VOLUMETRIC PHASED ARRAYS FOR SATELLITE COMMUNICATIONS

A Dissertation
Presented to
The Academic Faculty

By

William Chauncey Barott

In Partial Fulfillment
Of the Requirements for the Degree
Doctor of Philosophy in Electrical Engineering

Georgia Institute of Technology

August, 2006

VOLUMETRIC PHASED ARRAYS FOR SATELLITE COMMUNICATIONS

Approved By

Dr. Paul Steffes
School of Electrical and Computer Engineering
Georgia Institute of Technology

Dr. Douglas Williams
School of Electrical and Computer Engineering
Georgia Institute of Technology

Dr. Andrew Peterson
School of Electrical and Computer Engineering
Georgia Institute of Technology

Dr. Robert Roper
School of Earth and Atmospheric Science
Georgia Institute of Technology

Dr. Gregory Durgin
School of Electrical and Computer Engineering
Georgia Institute of Technology

Date Approved: June 26, 2006

For a mechanic, you do an awful lot of thinking.
-C-3PO

To those who have boldly gone where no man has gone before.

ACKNOWLEDGEMENTS

First and foremost, I thank my advisor, Dr. Paul Steffes, for almost six years of guidance and support. Quite simply, this research would not have happened without him.

I thank my committee members for the time that they invested in my work, and for their constructive comments throughout the process: Dr. Andrew Peterson, Dr. Douglas Williams, and Dr. Robert Roper. Special thanks to Dr. Gregory Durgin for his contributions as a member of my committee and for the generous use of lab equipment for the digitization and timing subsystem of this work.

Thanks also to Dr. Mary Ann Ingram for support through the Hybrid Ground Phase Array Project, which stimulated the development of this independent research. Thanks to Dan Mandl and Seth Shulman at the NASA Goddard Space Flight Center, who coordinated access to the NASA satellite EO-1 for demonstrating the ODIN array.

I was fortunate enough to act as a mentor for the NASA / SHARP program during the summer of 2005, which gave me the use of two excellent high school seniors. Thanks to Steven Singleton and Donna Huang for their precise and tireless work to construct and characterize eight antennas for the ODIN array. Similarly, I thank my long-time friend Brendon Church for his contributions to the array support structure and the enclosures for the RF hardware.

I also acknowledge my fifth-floor colleagues, whose collaboration and diversions helped in the development of this work and the maintenance of daily sanity. Thanks to Priscilla Mohammed, Allen Petrin, Thomas Hanley, and Elizabeth Moyer. Thanks also to Dr. Durgin's excellent team, Joshua Griffin, Chris Durkin, Ryan Pirkl, and Albert Lu, just to name a few. Thanks also to Sharon Fennell, who makes this place work.

Outside of Georgia Tech, I thank all of my friends, who have endured several years of antisocial graduate student behavior.

Special thanks to KF4GID (Jeanette Barott née Gartman) for marrying me, even after seeing what three years of graduate school did to me. It takes a brave woman to voluntarily choose a man who is open about his love for electromagnetics. I think I can finally solder better than you can now.

And to my parents, William Edwin and Pamela Norris Barott, you have been the best kind that anyone could ask for. Thank you for my love of tinkering and electronics, and for the chance to chase my dreams.

This work was supported by the Georgia Tech Foundation under award number 210000333 from the IDT Corporation. Additional support was provided by the NASA Advanced Information Systems Technology (AIST) Program under Grant NAG5-13362 from the NASA Goddard Space Flight Center.

TABLE OF CONTENTS

LIST OF TABLES

LIST OF FIGURES

LIST OF DEFINITIONS AND SYMBOLS

- A -

a. Vector containing a single steering vector

A. Matrix containing multiple steering vectors

Alpha (α). Half-arc for alias differentiation

AR. Axial Ratio

- B -

b. Vector of a single beam-space steering vector

BB. Base band

BER. Bit Error Rate

BIP. Beamforming with Interference Projection

bps. Bits per second, also K (kilo), M (mega), G (giga) and T (tera)

BPSK. Binary Phase Shift Keyed

BR. Bit Rate

BW. Multiple uses; (*as in frequency)*. Bandwidth; *(as in radiation pattern)*. Beamwidth, esp. in BW_{FN} (first-null beamwidth) and $BW_{3\text{dB}}$ (half-power beamwidth)

- C -

c. Index length, as in c_m (of the main beam) and c_n (of interferers)

CBF. Conventional Beamformer

CP. Circularly Polarized

CZT. Chirp-Z Transform

- D -

d. Distance between a ground station and satellite

dB. Decibel

dBc. Decibel with respect to the carrier

dBi. Decibel with respect to an isotropic radiator

dBic. Decibel with respect to an isotropic circularly polarized radiator

dBm. Decibel with respect to 1 mW

DBR. Daily Bit Rate

dBW. Decibel with respect to 1 W

Delta-P (ΔP). Figure of merit describing the quality of a synthesized radiation pattern

DFT. Discrete Fourier Transform

DG. Dense Grid

- E -

E-B-over-N-0 (E_B/N_0). Power per bit normalized by noise spectral density

EDT. Eastern Daylight Time

EES. Earth Environmental Satellite

EIRP. Effective Isotropic Radiated Power

El. Elevation angle

El-Min $(El_{\min})$. Minimum elevation angle at which a link is established

EMI. Electromagnetic Interference

EO-1. The NASA Earth Orbiter 1 spacecraft used in this research

- F -

f. Frequency

F. Multiple uses; *(beamforming)*. Matrix form of the FFT; *(data collection)*. Frame index number

FDTD. Finite Difference Time Domain

FFT. Fast Fourier Transform

FOM. Figure of Merit

- G -

G. Beam-space filtering operator

GA. Genetic Algorithm

gamma (γ). Internal angle between a ground station and satellite

Gamma (Γ). Reflection coefficient of an impedance mismatch

GB. Gigabyte (10^9)

GN. Ground Network

GPIB. General Purpose Interface Bus

GWN. Gaussian White Noise

- H -

H. Hermitian (complex transpose) operator

- I -

i. Orbital inclination

IF. Intermediate Frequency

IFFT. Inverse Fast Fourier Transform

IM. Intermodulation

IP3. Third order intercept point

- J -

JENNIE. Just Enough Nearly Impeccable Electronics

- K -

Kbps. Kilo bits per second (10^3)

KCS. Kilo complex samples (10^3)

- L -

l. Longitude, as in l_S

L. Latitude, as in L_S

lambda (λ). Wavelength

LAN. Local Area Network

LEO. Low Earth Orbit

LHCP. Left Hand Circular Polarization

LNA. Low Noise Amplifier

- M -

m. Masking operator for beam-space beamforming

Mbps. Mega bits per second $\left(10^6\right)$

MCS. Mega Complex Samples

MCS/s. Mega Complex Samples per second $\left(10^6\right)$

MOM. Method of Moments

MS. Mega Samples (Real)

MS/s. Mega Samples per second $\left(10^6\right)$

- N -

N. Number of antennas

NASA. National Aeronautics and Space Administration

NEC. Numerical Electromagnetic Code

NF. Noise Figure

- O -

ODIN. Omni Directional Interference Nulling

omega $\left(\omega\right)$. Argument of perigee

Omega $\left(\Omega\right)$. Longitude of the ascending node

- P -

PCI. Peripheral Component Interface

PDF. Probability Density Function

phi $\left(\phi\right)$. Multiple uses; *(beamforming)*. Phase error; *(geometry)*. Angular coordinate between a vector and the *x*-axis, as projected in the *xy*-plane

phi-0 (ϕ_0). Angle between perigee and the satellite

PLMA. Propagation Loss Matched Antenna

- Q -

QG. Quantization Grid

- R -

R-e (R_e). Radius of the earth

RF. Radio Frequency

RFL. Power loss due to reflection

RFP. Reduced Fourier-space Projection

RHCP. Right Hand Circular Polarization

R-s (R_S). Satellite orbital radius

RSLL. Relative Sidelobe Level

- S -

S-bar $(\overline{S})$. Average spacing between antennas, in units of wavelengths

SFL. Space-fed Lens

S-g (S_g). Spacing between periodic grid points

SLL. Sidelobe Level

SNR. Signal to Noise Ratio

SPDT. Single Pole Dual Throw

- T -

TDRS. Tracking and Data Relay Satellite

TDRSS. Tracking and Data Relay Satellite System

- V -

V. Matrix of steering vectors used for null-forming

VSWR. Voltage Standing Wave Ratio

- W -

WLAN. Wireless Local Area Network

- X -

x. Vector of phasor antenna outputs

- Y -

y. Output of a single beamformer

Y. Output of multiple beamformers

SUMMARY

The high amount of scientific and communications data produced by low earth orbiting satellites necessitates economical methods of communication with these satellites. A volumetric phased array for demonstrating horizon-to-horizon electronic tracking of the NASA satellite EO-1 was developed and demonstrated.

As a part of this research, methods of optimizing the elemental antenna as well as the antenna on-board the satellite were investigated. Using these optimized antennas removes the variations in received signal strength that are due to the angularly dependent propagation loss exhibited by the communications link. An exhaustive study characterized two antenna architectures, and included optimizations for radiation pattern, bandwidth, impedance, and polarization.

Additional studies were conducted regarding the optimization of aperiodic arrays. Volumetric arrays were investigated in detail, and pattern-space representations of volumetric arrays were created. A tracking algorithm for use with volumetric arrays was developed. This algorithm allows high-resolution direction finding using a small number of antennas while mitigating aliasing ambiguities. Finally, a method of efficiently applying multiple beam synthesis using the Fast Fourier Transform to aperiodic arrays was developed. This algorithm enables the operation of phased arrays combining the benefits of aperiodic element position with the efficiency of FFT multiple beam synthesis.

CHAPTER 1.
INTRODUCTION

Earth Environmental Satellites (EES) and other remote sensing satellites deliver significant amounts of valuable data from their positions in low earth orbit (LEO). The increased resolution and shortened orbital periods provided by low orbital altitudes are necessary for many applications, but fast orbits and ever-increasing data rates put a strain on present downlink systems.

Two methods of retrieving data from LEO satellites presently exist. The first of these is for the satellite to upload data to the Tracking and Data Relay Satellite System (TDRSS), where it is relayed and downloaded to the ground network (GN). The original TDRSS constellation consists of five satellites in geostationary orbit. Each of these satellites is capable of receiving high-speed Ku band data of up to 300 megabits per second (Mbps) from a single user.

Three "second generation" satellites were launched between 2000 and 2002. These satellites receive Ka band data of up to 1200 megabits per second from a single user as an alternative to the Ku band link. While impressive, the cost of TDRSS is enormous: the TDRS replenishment program responsible for the three second-generation satellites cost $840 million and the annual operating costs of TDRSS total $90 million. Additionally, each TDRS can support only two high-data-rate users at a time, and many LEO satellites with data rates in excess of 100 Mbps are currently in operation [1, 2].

An alternative to uploading data to TDRSS is for a satellite to download data directly to the GN. Currently, downlink stations consist of many large dish antennas that

Figure 1.1: Photograph of the Svalbard downlink station. From [3].

require at least one antenna for each satellite being tracked simultaneously. These stations are often located in remote polar areas to maximize the amount of data the station can download per day. One such station, located in the Svalbard archipelago in northern Europe, is shown in Figure 1.1. Not only is the process of steering these antennas with the requisite precision and speed costly and inefficient, but the remoteness of these stations increases the cost of maintenance and repair. The volume and importance of the data collected by LEO satellites necessitates finding more economical methods of creating efficient LEO downlink systems.

One alternative to such costly systems is a phased array of many inexpensive wide-beam antennas utilizing software-defined radio beamforming. Such a system would

Figure 1.2: Photograph of the X-band urban inflatable downlink array.

reduce or eliminate the need for mechanical steering and allow for simultaneous multibeam tracking of spatially separated spacecraft. Present methods of data recording and beamforming are very resource intensive [4]. For example, a 1 Mbps data stream that is binary-phase-shift-keyed (BPSK) and half-rate encoded has a 4 MHz first-null bandwidth. Digitizing this stream requires a digitized data rate of 96 Mbps for a single channel if 12-bit digitizers are used. This is almost two orders of magnitude greater than the original data rate. Despite this, several such arrays are presently under development [5, 6].

A photograph of one array that was used to demonstrate data download from the Argentinean satellite SAC-C is shown in Figure 1.2. The photographs in Figs. 1.1 and 1.2 represent the motivation for the present work on LEO satellite downlink systems: to

Table 1.1:
Characteristics of the Satellite EO-1

Characteristic	Value
Orbital Altitude	707 km
Eccentricity	1
Inclination	98°
EIRP	-2.2 dBm
Carrier Frequency	2270.4 MHz
Data Rate	2 Kbps
Encoding	½ Rate Convolutional
Modulation	BPSK
First Null Bandwidth	8 KHz

replace expensive and remote ground stations with a network of many inexpensive and urban ground stations.

This research has focused on the development of techniques for antenna and array design and has culminated in an array for tracking the NASA environmental satellite EO-1. The characteristics of this satellite are summarized in Table 1.1 [7]. Work was conducted in several areas of design and optimization, including elemental antennas, phased arrays, data processing, and target tracking.

This dissertation is divided into five parts, each of which describes a different aspect of this work. The first part is an introduction to LEO satellites and genetic algorithms. The second part focuses on the design of a propagation loss matched antenna (PLMA), which was used as a basis for the construction of the final array. The third part of this dissertation contains the results of aperiodic phased array analysis, including new methods of beamforming and target tracking as well as analyses of volumetric phased arrays. The final array is volumetric and implements these tracking algorithms. The fourth part contains information on the hardware of the demonstration array, dubbed the

Omni Directional Interference Nulling array (ODIN). The fifth and final part of this dissertation contains results and conclusions regarding the applications of the new elemental antenna and array design approach to phased arrays.

Part 1:

LEO Satellite Communications and Genetic Algorithms

CHAPTER 2.
LEO SATELLITES

2.1 Introduction

This research has focused on systems for data downlinks that are applicable to any LEO satellite. Before proceeding, it is necessary to discuss the characteristics of a satellite orbit, as well as to show the derivation of the metric used to compare ground station designs. This metric is defined as the daily bit rate (DBR) of the ground station and represents the average number of bits a ground station can receive from a single satellite within a 24-hour period. A probabilistic approach is used to derive a function describing this metric.

2.2 Orbit Descriptions

The orbits of LEO satellites can be approximated by ideal Keplerian orbits. Two angles define the plane of the orbit: the inclination of the orbit (i) and the longitude of the ascending node (Ω). The shape of the orbit is further described by the eccentricity (which is one for a circular orbit), the radius of the orbit (R_S), and the argument of perigee (ω). The position of the satellite is described by the angle between perigee and the position of the satellite (ϕ_0) [8]. A diagram of the orbit is shown in Figure 2.1.

The distance between a ground station and the satellite can be found by simple trigonometry, as shown in Figure 2.2. If R_e represents the radius of the earth and γ is the internal angle between the ground station and the satellite, this distance is determined by

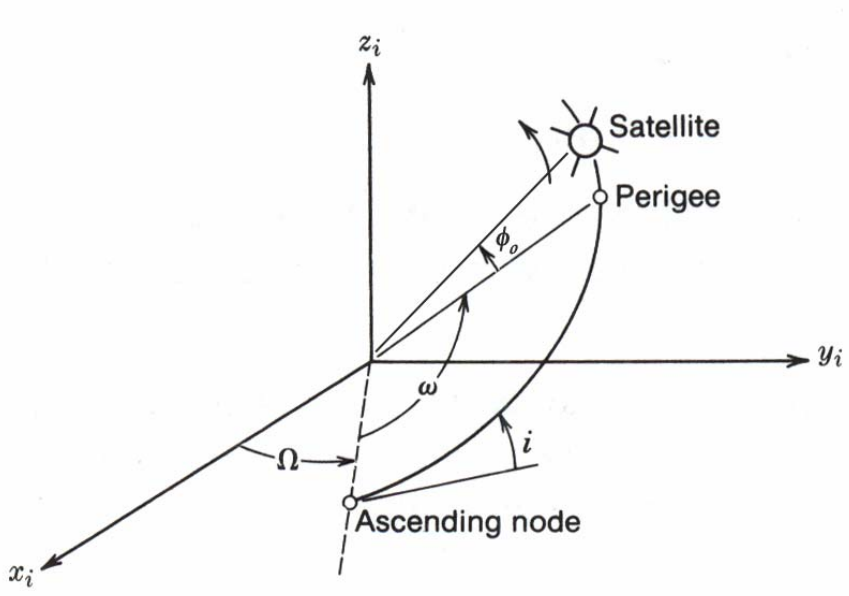

Figure 2.1: Graphical representation of the orbital model. From [8].

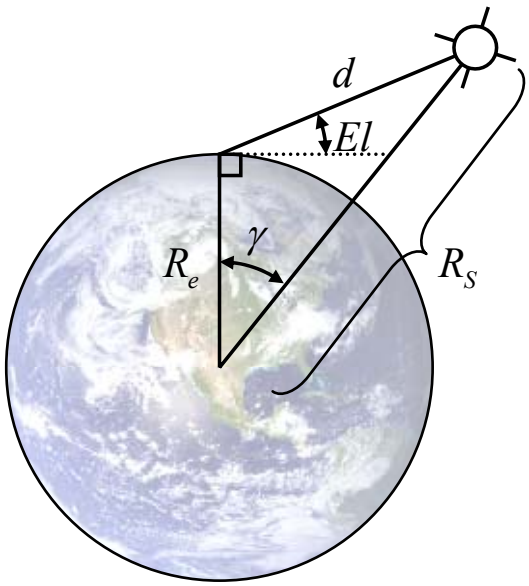

Figure 2.2: Graphical representation of the relationship between the internal angle, γ, and the distance between the ground station and the satellite.

$$d = R_S\left[1+\left(R_e/R_S\right)^2 - 2\left(R_e/R_S\right)\cos\left(\gamma\right)\right]^{0.5}. \qquad (2.1)$$

For LEO satellites, R_e and R_S have values within thirty percent of each other. Therefore, the distance varies significantly with changes in γ. As a result, the signal incident on a ground station has a much higher power when the satellite is overhead than when it is near the horizon. This principle is the basis for the antenna optimization work presented in Part 2.

For the probabilistic analysis of LEO satellites, it is assumed that their orbits are circular ($i = 1$), and the argument of perigee is arbitrarily assigned a value of $\omega = 90°$. Because ϕ_0 changes at a constant rate over time for a circular orbit $\left(d\phi_0/dt = C\right)$, it is convenient to use $d\phi_0$ instead of dt for calculations. Also, the value of $\phi_0\left(t\right)$ is assumed to be a uniformly distributed random variable between $0°$ and $360°$.

The motion $d\Omega/dt$ is also constant and is due to both short-term and long-term effects. The precession of sun-synchronous orbits causes a change of $0.986°$ per day; the nodal regression caused by the rotation of the earth causes a change of $360°$ per day. As a result, the angle $\Omega\left(t\right)$ can be considered as a uniformly distributed random variable between $0°$ and $360°$. The angles Ω and ϕ_0 are uncorrelated.

2.3 The Probability Density Function of the Subsatellite Point

At any moment in time, the subsatellite point is uniquely defined by its latitude and longitude coordinates, L_S and l_S. Because Ω can be considered as a uniformly distributed random variable, l_S can also be considered a uniformly distributed random variable between $0°$ and $360°$. For any latitude coordinate, a circle is defined that

intersects all possible subsatellite points and has a circumference given by $2\pi R_e \cos(L_S)$, where R_e is the radius of the Earth.

If L_S changes by an incremental amount dL_S during an interval of time defined by $d\phi_0$, then the incremental area containing all possible subsatellite points during the interval is given by

$$\begin{aligned} dA/d\phi_0 &= \left| dL_S/d\phi_0 \cdot \cos(L_S) \cdot 2\pi \cdot R_e^2 \right| \\ &= \left| \sin(\phi_0) \cdot \sin(i) \cdot 2\pi \cdot R_e^2 \right|, \end{aligned} \tag{2.2}$$

where ϕ_0 is related to L_S by

$$\phi_0 = \arccos\left[\frac{-\sin(L_S)}{\sin(i)} \right]. \tag{2.3}$$

The probability density function (PDF) of the satellite's location can be shown to be

$$p(L_S, l_S) = \frac{\cos(L_S)}{2\pi^2 \cdot \left| \sin(\phi_0) \cdot \sin(i) \right|}. \tag{2.4}$$

2.4 Ground Station Footprint

The "footprint of a ground station" is defined as the set of subsatellite points for which a link to the satellite can be accomplished. If the propagation loss due to distance is the only variable that determines the received power per bit of data normalized by the noise power spectral density (E_B/N_0), then the threshold transmitted power that is required for data downlink is related to an elevation angle in the local coordinates of the ground station. For a given spacecraft transmitted power, this angle will be referred to as

the minimum elevation angle for downlink $\left(El_{\min}\right)$. Transmission is possible only if the satellite is above $El_{\min}$.

The law of sines relates $El_{\min}$ to the set of subsatellite points from which a signal can be received. For any latitudes L_G and L_S of the ground station and subsatellite point, a value Δl_S is defined that describes the difference in longitudes for which the satellite is at $El_{\min}$ [8].

The probability that a transmission can occur at any instant in time is given by the integration of (2.4) over the footprint of the ground station,

$$P_T = \int_{-L_{Max}}^{L_{Max}} \int_{-\Delta l_S}^{\Delta l_S} p\left(L_S, l_S\right) \cdot dL_S dl_S \ , \qquad (2.5)$$

where $L_{Max} = \min\left(i,\ 180° - i\right)$. The DBR for the ground station is found by $86400 \cdot P_T \cdot BR$, where 86400 is the number of seconds in a 24-hour period and *BR* is the rate of the link (bps).

Generally, if the communications link has several different bit rates, and the bit rate at a given time is the maximum bit rate than can be established while maintaining the required quality of service, the aggregate DBR is given by

$$DBR = 86400 \cdot \sum P_{T\,i} \cdot \left(BR_i - BR_{i-1}\right), \qquad (2.6)$$

where increasing indices correspond to increasing bit rates. The value of BR_0 is zero by definition. An illustration of this concept is shown in Figure 2.3. When the subsatellite point is within the outer circle (including the inner circle), a 50 Mbps link can be

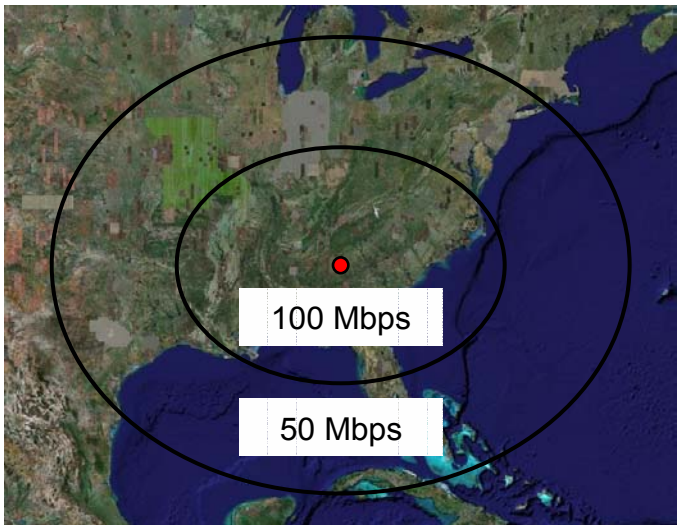

Figure 2.3: Possible link data rate as a function of the subsatellite point.

established. The data rate can be increased to 100 Mbps when the subsatellite point is located inside the inner circle.

If *BR* is a function of the signal power incident on the ground station, then it can be defined as a function of the latitude and longitude of the subsatellite point. The expression for the DBR will take the form of

$$DBR = 86400 \cdot \int_{-i}^{i} \int_{-\Delta l_s}^{\Delta l_s} p\left(L_S, l_S\right) \cdot BR\left(L_S, l_S\right) \cdot dL_S dl_S \,. \qquad (2.7)$$

The highest DBR will be achieved when *BR* is a continuous function so that the received E_B / N_0 is always equal to the threshold value.

It is possible to find a value L_G that maximizes (2.7) for particular values of *i* and $El_{\min}$. If fixed antennas are used, then the footprint of the ground station can be shaped to further maximize the DBR of the network. Using EO-1 as an example, a single ground station located at 64°N receives 1.7 times as much data from subsatellite points that are

north of 64°N that from points south of the ground station. This effect will be seen in the optimization of fixed Space-fed Lens antennas in Appendix D.

2.5 Network Analysis

For satellites with high orbital inclinations, ground stations at polar latitudes have a higher DBR than ground stations at temperate or equatorial latitudes. However, if the ground station cost is low, then it is economically viable to use multiple ground stations in equatorial regions and achieve the equivalent DBR of a single polar ground station.

Several network configurations were examined to demonstrate the requirements of a network of ground stations located in temperate or equatorial regions. The design goal for these networks was to meet or exceed the DBR of a single 11m dish antenna downlink station located at the Poker Flats facility in Alaska. The value $El_{\min}$ is restricted to 5° above the horizon. The 105 Mbps X-band downlink of EO-1 is used as a test case. The threshold E_B/N_0 for demodulation for this link is 6.5 dB.

Table 2.1 contains DBR results for a number of different network configurations. The variables in the network include the number of ground stations, the position of the ground stations, the number of antennas per ground station, and the data rate. Both fixed and variable data rate models are considered. The elemental antennas of the ground stations are 0.75m dish antennas. It is observed that several networks produce DBRs comparable to the Poker Flats facility.

Table 2.1:
Network Configurations and Performance

TX Rate (Mbps)*	Network**	Total Antennas	DBR (GB)
105	11m (PF) -- Reference	1	585
50	3 x2 (S, B)	6	270
50, 100	3 x2 (S, B)	6	395
50, 100, 200	3 x2 (S, B)	6	497
50, 100	3 x3 (S, B, T)	9	501
50, 100, 200	3 x3 (S, B, T)	9	642
105	3 x2 (S, B)	6	246
105	7 x2 (S, B)	14	587
105	5 x3 (C, H, DC)	15	545
105	5 x2 (H, DC) 6 x1 (C)	16	578
50	3 x4 (H, S, B, T)	12	427
105	8 SFL x2 (S, B)	16	587

*Where multiple transmit rates are listed, the system uses the highest of the listed rates that can be supported based on the signal power incident on the ground station. As a result, the data rate will not be constant during a downlink period, and will change as described in Figure 2.3.
**Network layout format is: Number of antennas per station x Number of stations (Station codes). Station codes include: Bangor, Maine (B), Stockton, California (C), Washington, D.C. (DC), Honolulu, Hawaii (H), Poker Flats, Alaska (PF), Seattle, Washington (S), and Corpus Christi, Texas (T).

2.6 Predicting Satellite Location

Ideal Keplerian orbits are sufficient for probabilistic analyses, but are not useful for accurately predicting the location of a satellite as a function of time. Several models exist for predicting the location of an orbiting body; these go by the "SGP" and "SDP" family names. The SGP model was developed in 1966 and is the simplest to implement, but it offers the least accuracy. This model is used for near earth satellites whose orbits are not affected by the gravitational pull of bodies other than the earth. SGP4 (1970) and SGP8 (1980) are more complex to implement but offer greater accuracy than the SGP

model. The SDP models, SDP4 and SDP8, are similar to their SGP counterparts but are intended for calculating deep space trajectories [9].

Comparisons between the outputs of the SGP and SGP4 models indicate a difference in look-angles of less than $0.5°$ for low earth orbiting satellites. This accuracy is sufficient for the ODIN demonstration array, which has a beamwidth of about $4°$. While a free Matlab^{TM}-based SGP package was integrated into the array processing routines [10], no Matlab-based SGP4 implementation was available. Readers should refer to more in-depth documentation of the SGP models, such as [9], for more information and the relevant mathematics.

CHAPTER 3.
GENETIC ALGORITHMS

Solutions to many problems in electromagnetics rely on various numerical methods. The method of moments (MOM) based numerical electromagnetic code (NEC) and finite difference time domain (FDTD) method are two such numerical methods for solving antenna pattern, scattering, and propagation problems [11]. These methods solve Maxwell's equations subject to certain conditions and based on certain approximations. These methods are usually implemented numerically because it is not possible to solve many of the resulting differential equations analytically. These methods generally solve systems of the form

$$\nabla E(x,y,z,t) = \int A(x,y,z,t) + \nabla B(x,y,z,t). \qquad (3.1)$$

The integration and differentiation operators in Equation (3.1) represent generalized operators for such a system. The variables x, y, z, and t are known, and the functions A and B are deterministic, but tedious.

Other types of problems exist where the outcome is known but the constituent variables are not. These include problems of antenna or array analysis in which it is desired to control the shape of the radiation pattern. If the element positions of an array are constrained to a grid, and electromagnetic effects are ignored, and only the phase and magnitude of each element's stimulation are altered, analytical methods exist for optimizing the sidelobe levels and radiation patterns of the array [12]. Although the results can be improved significantly if the element positions deviate from the grid, the

analytical methods cease to apply. If electromagnetic effects such as coupling and scattering are included in the analysis, no solution exists outside of an iterative numerical model. Such problems have the form

$$P = C(x, y, z, t). \tag{3.2}$$

The values of the variables are unknown and could be determined by equations of the type (3.1). Some conditions are known regarding both P and the bounds of the variables, but C is noninvertible, and no direct answer can be obtained without searching the solution space.

Problems such as those described by (3.2) are well suited for iterative methods. After a solution condition is defined, the algorithm alters the system variables in an attempt to find a combination that gives a solution most closely related to the solution condition. The Newton-Raphson method for finding the roots of a function is one such iterative method that uses the derivatives of the function at the point i to generate the $i+1$ guess [13].

The title of genetic algorithm (GA) applies to any iterative optimization algorithm that resembles the process of evolutionary biology [14]. Although initially time consuming to create, a properly designed GA will essentially solve the problem autonomously, and significant modifications to the problem are easy to implement once the structure of the algorithm is in place. Many resources exist on the application of genetic algorithms to problems in electromagnetics [14-17].

The GA structure used in this research is shown in Figure 3.1 and has four essential steps per iteration. First, the algorithm expands the population of potential

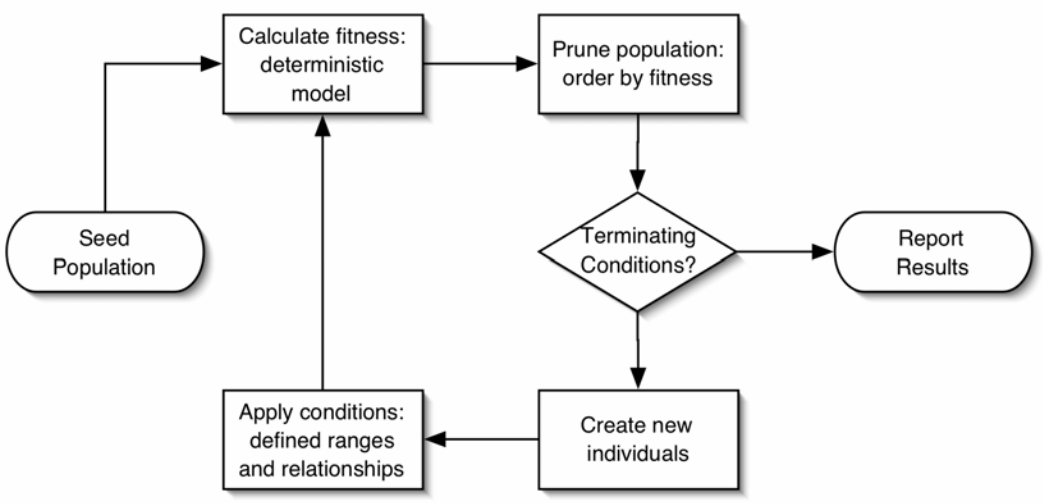

Figure 3.1: Outline of the GA process.

variable value sets by adding new individuals. Second, conditions are applied so that the genes of the new individuals correspond to realistic values for the variables in the problem. Next, the algorithm calculates the fitness of each individual. Last, the population is pruned back to its original size by the elimination of the worst performing members. Over many iterations, the average fitness of the population will improve toward the optimal value. The algorithm can either proceed for a set number of generations or halt after meeting a predetermined condition. The GA represents the values of the genes with continuous variables describing the exact size of an object, as in [16], or Boolean values describing the presence or absence of an object, as in [17]. The algorithms used in this study implemented genes of continuous variables, which are preferred for many antenna and array design applications [18].

The algorithm creates new individuals by four methods. First, a completely new individual is added to the population; this individual has a pseudo-random genome and is

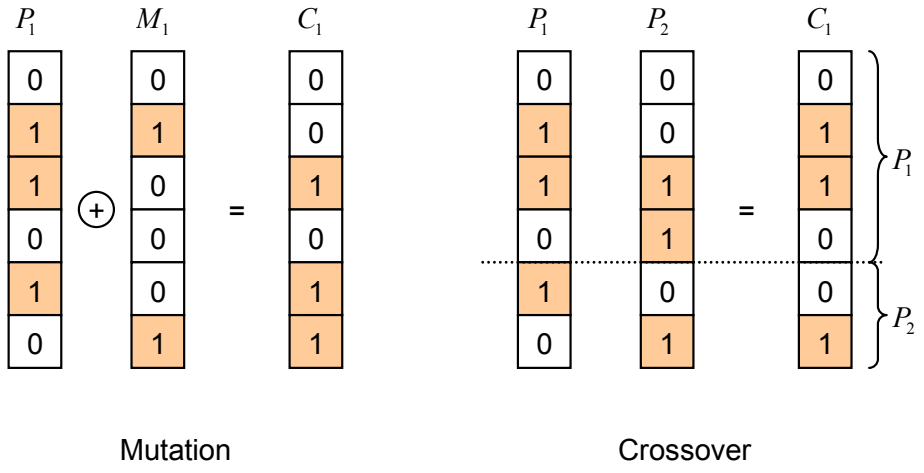

Figure 3.2: The GA spawning processes.

not related to other individuals. Second, an individual from the population is chosen and duplicated; the new individual undergoes a small mutation to some or all of its genes. Third, two distinct parents are chosen at random from the population; a crossover point is chosen, and the genes of the parents are spliced to create a new individual. Finally, crossover is performed as in the previous method, but the child undergoes a set of random mutations as in the second method. Graphical illustrations of these processes are shown in Figure 3.2.

Mutations of Boolean genes are implemented with an XOR function, as shown in Figure 3.2. The mutation vector M_1 is allowed up to N_M nonzero entries, which each cause a single bit alteration from the parent, P_1, to the child, C_1. Mutations of continuous genes are implemented with vector addition. For the i_{th} continuous variable of the parent, $P_1(i)$, a uniformly distributed random number $M_1(i)$ is added such that

$$C_1(i) = P_1(i) + M_1(i). \tag{3.3}$$

The maximum magnitude of M is the mutation rate and determines the maximum difference between a child and its parent. A larger mutation rate is equivalent to a larger value of N_M for a Boolean gene.

The conditions applied to genes depend on the particular application. Some conditions in a linear array include restrictions on the spacing between elements, element size, and element stimulation. Similarly, the fitness of each individual depends on the particular problem, and the user specifies the method for calculation. The algorithms used in this research for calculating fitness account for the simulated radiation pattern, impedance, and sidelobe level of an individual.

It is possible to implement additional subroutines in a genetic algorithm. For example, Boeringer and Werner reported the advantage of using a GA with self-adaptive mutation rate controls [19]. Other possibilities include adaptive complexity algorithms wherein the resolution, or number of bits allocated to an individual, is adaptively controlled. While not a subject of this research, the development of adaptive resolution algorithms is a subject of continuing research. The algorithm that was used in this research was a non-adaptive GA that optimized a genome defined by a structured variable in Matlab.

Part 2:

Antenna Optimization

CHAPTER 4.
GENETIC ANTENNAS

The efficiency with which genetic algorithms solve complex numerical problems is well-suited to antenna design, where many variables must be optimized for a problem with complex and competing design goals. The application of GAs to antenna design was pioneered by Linden and Altshuler [18, 20-23]. The most widely recognizable genetic antenna is Linden's meander antenna, shown in Figure 4.1.

Many other models for genetic antennas exist. Taxonomically, these models and antennas can be classified into categories based on familiar antennas (such as Yagi-Uda array, helix, or spiral antennas) and unfamiliar antennas (such as node, binary patch, or meander antennas) [24, 25]. Examples of the unfamiliar antennas are shown in Figure 4.1. Each model has advantages and disadvantages in computational cost, ease of construction, and performance. Generally, a less restrictive model creates an unfamiliar antenna and can produce surprising results, but it has a much higher computational cost.

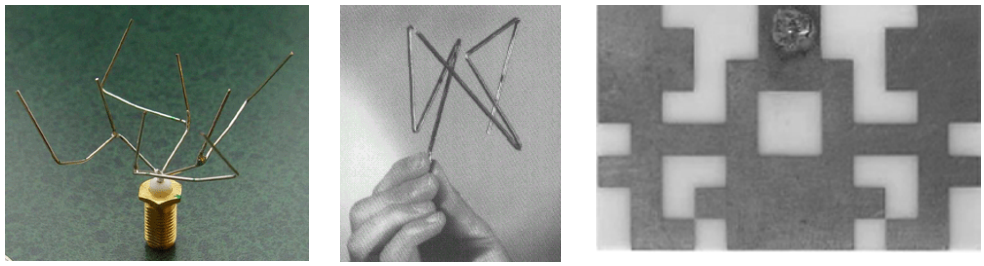

Figure 4.1: Unfamiliar genetic antennas based on loosely restricted models.

For example, a Yagi parasitic antenna requires only two variables for each element: the length and distance from the feed. A similar less restricted design requires six variables for each element, representing the *x*, *y*, and *z* coordinates of both ends of every wire.

Computational cost isn't the only consideration when choosing the proper model; the suitability of the model to the current problem is also important. For example, while a Yagi model is well suited to creating a beam pattern similar to that radiated by a linear phased array, the Yagi architecture is linearly polarized and narrow band because of the dipole elements. Alternatively, many node antennas are circularly polarized and broadband, but inappropriate for tasks requiring a narrow beam width.

The following chapters focus on the design of the antenna selected for the Omni Directional Interference Nulling (ODIN) array. Improvements and alternative applications are also discussed.

CHAPTER 5.
THE PROPAGATION LOSS MATCHED ANTENNA

5.1 Introduction

It was noted in Chapter 2 that the distance between a LEO satellite and a ground station varies significantly while the satellite is in view of the ground station. As a result, the propagation loss of a communications link will also vary significantly. The amount of variation can be found using orbital equations. A ground station antenna was developed for the purpose of compensating for variation in incident power; this antenna is similar in concept to slant range or cosecant type antennas. Ideally, this antenna provides constant signal strength, and E_b/N_0, at the output of the antenna, maximizing the amount of data that can be downloaded from the satellite without increasing the cost of the array.

This antenna was developed using a combination of genetic algorithms and the method of moments (MOM) based numerical electromagnetic code (NEC) [11]. This elemental antenna was developed specifically for the NASA satellite EO-1, which has an orbital altitude of 707 km. Because only the angularly dependent propagation loss was included in the model, this antenna is called a *propagation loss matched antenna* (PLMA). Extensive analysis was conducted to identify the requirements for such an antenna, and several designs were selected for construction and testing before one design was selected as the elemental antenna for the ODIN array.

Several terms will be used in a standard fashion for this chapter to avoid ambiguity. For example, although *antenna* could apply to a component dipole, to the

parasitic array of dipoles comprising the elemental antenna being discussed here, or to the phased array of antennas, in this chapter it will only be used to refer to the elemental antenna, or PLMA. Similarly, the *element* is the component building block of the *antenna* (PLMA) and the *phased array* or *ground station* is a collection of many PLMAs.

5.2 Design and Model

5.2.1 Overview of the PLMA

Using orbital equations [8] and the descriptions contained in Chapter 2, the distance between a ground station and a satellite is given by

$$d = R_s\left[1+\left(R_e/R_S\right)^2 - 2\left(R_e/R_S\right)\cos\left(\gamma\right)\right]^{0.5}, \qquad (5.1)$$

where R_e and R_S are the radii of the earth and the orbit, and γ is the angle between the radii. The angle γ is related to the satellite's elevation coordinate as measured at the ground station by

$$\cos\left(El\right) = \sin\left(\gamma\right)\cdot\left(R_e/d\right). \qquad (5.2)$$

For satellites in low earth orbit, this distance is almost four times greater when the satellite is near the horizon than when it is at zenith. The signal power incident on a ground station is related to this distance by the Friis transmission equation,

$$\frac{P_r}{G_r} = P_t G_t\left(\frac{\lambda}{4\pi d}\right)^2, \qquad (5.3)$$

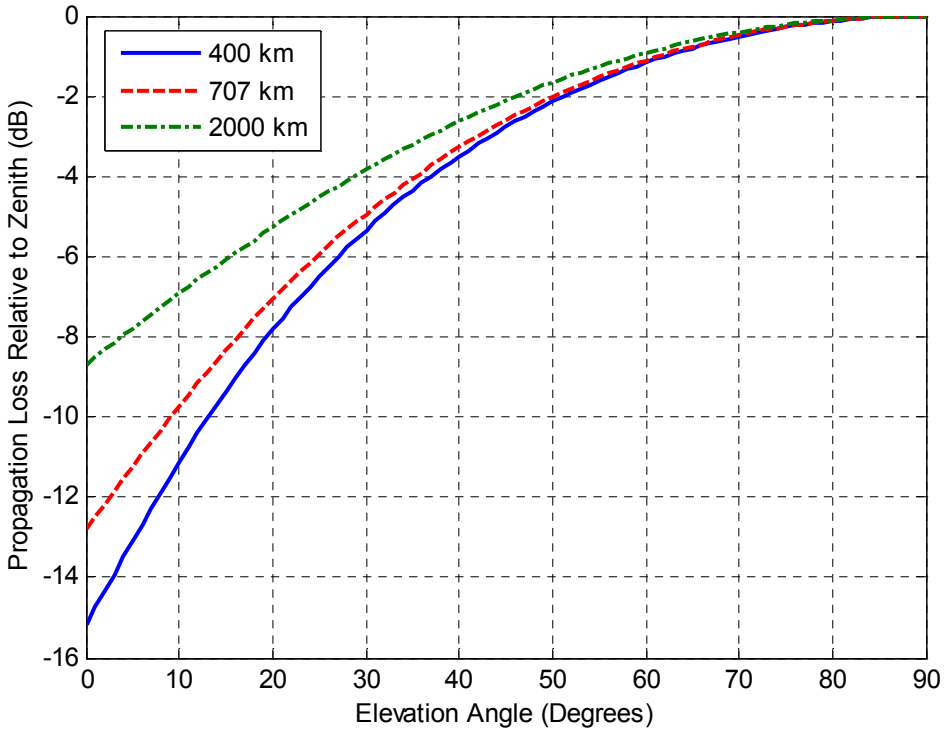

Figure 5.1: Propagation loss relative to zenith for satellites at various altitudes.

where P and G represent the transmitted and received powers and gains and λ is the wavelength of the communications signal. For this analysis, it is assumed that the satellite antenna is isotropic. The propagation loss of the communications link is given by the term

$$L_P = \left(\frac{\lambda}{4\pi d} \right)^2 . \qquad (5.4)$$

This is a mathematical expression for the commonly-known inverse-square-law. If the distance varies by a factor of four, the propagation loss, and therefore the received power, will vary by a factor of 16, or 12 dB. By Equations (5.1) and (5.2), the incident power is related to the elevation coordinate of the satellite. A plot of this relationship is shown in

Figure 5.1 for LEO satellites at several orbital altitudes. If the ground station antennas have a gain that is independent of the direction to the satellite, a system designed for horizon-to-horizon communications with a LEO satellite will exhibit an excess link margin greater than 10 dB when the satellite is at high elevation angles.

An excess link margin adversely affects the efficacy of the receiving ground station, which is defined as DBR/N, the number of bits downloaded per-day per-antenna. This efficacy can be maximized by satisfying three conditions. First, the received energy per bit, normalized by the noise power spectral density $\left(E_b/N_0\right)$, should be constant for the duration that the link is established; an excess link margin at any time leads to wasted downlink capacity and increased system cost. Second, the received E_b/N_0 should be equal to the threshold E_b/N_0 required for the desired bit error rate (BER). Third, the elevation angle at which a link is established $\left(El_{\min}\right)$ should be as close to the horizon as possible.

The received E_b/N_0 can be made constant either by varying the channel bit rate or by synthesizing a ground station radiation pattern to remove the angularly dependent variations in the incident signal strength. These methods are illustrated in Figure 5.2. It can be shown for a ground station consisting of N fixed antennas that the maximum efficacy is achieved using a synthesized radiation pattern and a constant bit rate.

The benefits of maximizing the ground station efficacy are seen by examining the total number of antennas required for a global network of downlink stations. In this analysis, the total ground area of subsatellite points serviced by the ground station network is a constant. The network can receive data from the satellite when its subsatellite point is inside the service area. If the data rate of the link is constant, a fixed

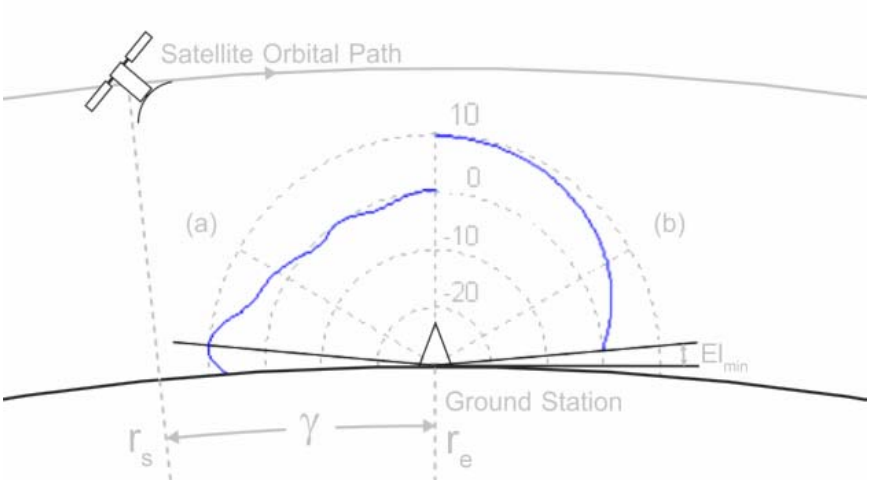

Figure 5.2: Methods of compensating for the variations in incident signal power: (a) Absolute gain (dBi) of a single antenna in the phased array of fixed antennas, using pattern synthesis and assuming a constant data rate link. (b) Relative channel bit rate (dB), without pattern synthesis.

service area equates to a fixed amount of data downloaded per day. The network can consist of either a few ground stations with small $El_{\min}$ values or many ground stations with $El_{\min}$ values closer to zenith. The number of antennas is found by $N_{tot} = A_{tot} N_g / A_g$, where A_{tot} is the fixed area containing the subsatellite points serviced by the global network, A_g is the footprint area serviced by a single ground station, and N_g is the number of antennas required for a single ground station.

Figure 5.3 shows plots of the relative number of elemental antennas required for the global network as a function of the $El_{\min}$ of the individual ground stations. Values are plotted for two arrays using two different types of fixed antennas. The first has a uniform gain at all angles above $El_{\min}$ and a gain of zero elsewhere; the second is the PLMA, which has a radiation pattern that is matched to the inverse of the predicted propagation loss at angles above $El_{\min}$ and zero gain elsewhere.

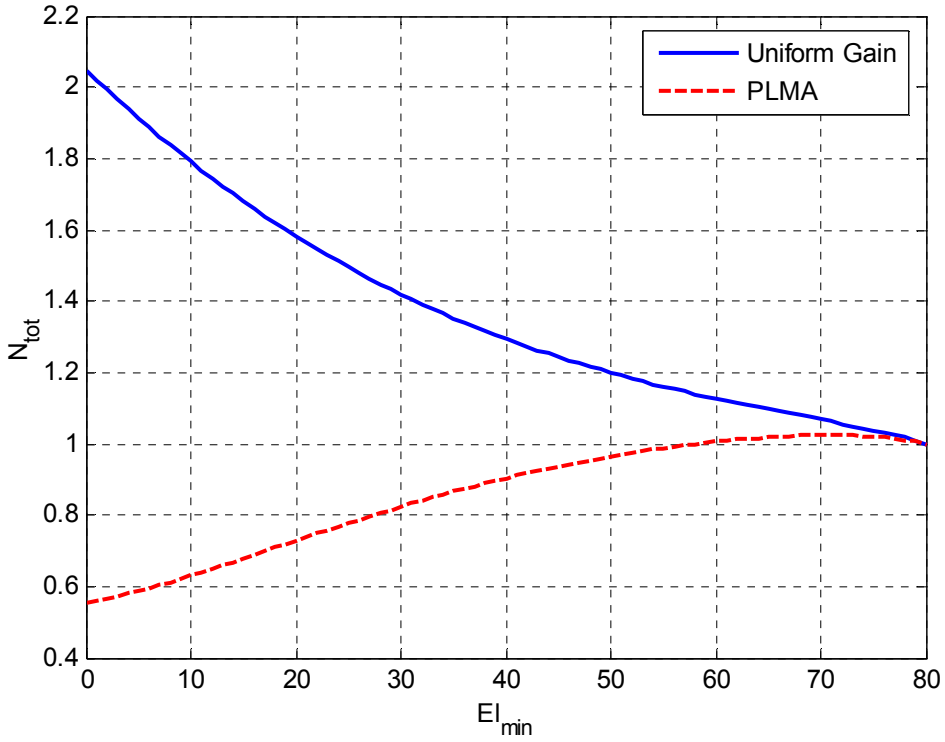

Figure 5.3: Number of antennas required for a network of ground stations providing data downlink from a satellite at 707 km altitude. Data is normalized to a value of 1 for $El_{\min} = 80°$.

A network of fixed PLMAs requires fewer antennas when the ground stations have $El_{\min}$ values close to the horizon than when the values of $El_{\min}$ are nearer to zenith; the opposite is true for a network of fixed antennas with uniform gain. Overall, the network of PLMAs requires fewer antennas than a network of antennas with uniform gain; the reduction is more than 70% in a network of ground stations with $El_{\min}$ values near the horizon. The cost reduction varies between 80% and 60% for satellites at altitudes between 400 km and 2000 km.

5.2.2 Design Model

One way to synthesize the desired radiation pattern is to model each elemental antenna as a fixed array of radiating elements. These elements are distributed along the *z*-axis for rotational symmetry and are phased, spaced, and weighted so the radiation pattern of the PLMA matches the desired radiation pattern. If the antenna is properly designed, it is possible to feed only one of the elements; the other elements are parasitic, with currents controlled by their size and position. Since the PLMA has only one signal port, the cost of the PLMA is similar to the cost of any other fixed elemental antenna commonly used in a phased array.

Although there are methods to synthesize the pattern of an elemental antenna consisting of an array of identical and equally spaced elements [12], there are no analytical methods for designs allowing for variable spacing or including the effects of electromagnetic coupling. A GA is used for the design of this elemental antenna. The characteristics of this GA are shown in Table 5.1. Each trial is repeated many times to ensure statistical reliability of the results. The mutation rates and spawning methods

Table 5.1:
Genetic Algorithm Characteristics for the Dipole PLMA

Characteristic	Value
Population Size	110 Individuals
Advancement	Best 50 of Total Population
Spawning Methods	30 by Mutation 20 by Crossover 10 by Mutation and Crossover
Maximum Mutation	0.2λ (Spacing) 0.05λ (Length)
Termination Condition	500 Generations

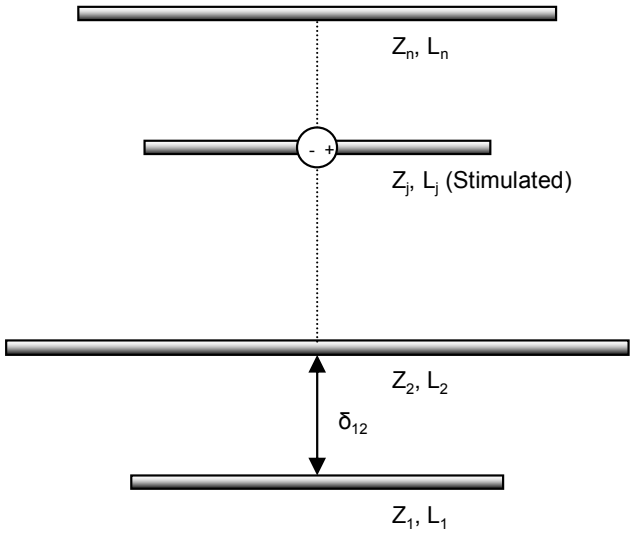

Figure 5.4: The dipole PLMA design model.

were determined empirically to obtain the fastest convergence for the algorithm. The GA stores continuous values describing the positions and lengths of the elements instead of Boolean or discrete values.

A genetic Yagi-Uda Array was selected as the PLMA design model, as shown in Figure 5.4. Horizontally oriented dipoles serve as the elements of the PLMA; one dipole is selected as the feed element and the others are parasitic. The position and length of each element are optimized with the minimum distance between adjacent elements as $\lambda/10$. This design model satisfied the requirements of the system to be demonstrated as part of this research. First, it is simple to analyze and construct, as compared to other genetic antenna models (for example, [22] and [26]). Second, although the source satellites radiate circularly polarized (CP) signals, the phased array should accommodate

both RHCP and LHCP signals so tracking and downlink can be demonstrated with many different satellites. No ground plane is included in this design because these antennas are distributed in a volumetric array.

Although the design model in Figure 5.4 is inspired by, and is similar in appearance to, a Yagi parasitic antenna, there are two important distinctions. First, while a Yagi is designed for boresight radiation, the PLMA is designed for near-broadside radiation. Second, approximate design rules regarding directors and reflectors exist for a Yagi, but the exact lengths and positions of the elements in the PLMA define exact currents and phases on each of the wires, and no director or reflector symmetry exists in the dipole PLMA design.

5.3 Design Optimization Results

5.3.1 Overview

More than 3600 genetic algorithm optimization trials were performed based on the MOM dipole PLMA model, testing a total of over 100 million design variations. These trials were executed on a cluster of six AMD Athlon 2400 computers that ran in parallel for about twelve weeks. Variables within individual trials included only the dipole lengths and positions; multiple trials were conducted wherein the number of dipoles, the selection of the stimulated element, the antenna bandwidth, and the allowed impedance mismatch were varied.

The GA attempts to create a synthesized radiation pattern that is as close to the ideal pattern as possible. The algorithm minimizes the maximum pattern error of the antenna when used with an impedance-matched feed, as defined by

$$\Delta P_{\max} = \max\left[G(\theta)_{dB}^{ideal} - G(\theta)_{dB}^{actual} \right]. \qquad (5.5)$$

The maximum pattern error reflects the number of elemental antennas required for communication to a satellite over the specified range of angles. An array consisting of antennas with a $\Delta P_{\max}$ value of 3 dB requires twice as many antennas as an array of ideal antennas.

It is customary to define the figure of merit (FOM) for an individual candidate solution (in this case, a PLMA design) in a GA optimization so that a higher FOM represents a better solution; the FOM in dB is given by the inverse of the maximum pattern error ($\Delta P_{\max}$, in dB) as

$$FOM = -\Delta P_{\max}. \qquad (5.6)$$

The pattern used to determine the FOM is taken on the plane broadside to the dipoles and the pattern is normalized to correct for the enhanced gain of the individual dipoles. In practice, the dipoles exhibit gain variations and nulls in planes other than broadside. Such pattern variations must be considered in the design of a phased array.

The $\Delta P_{\max}$ of the optimized antenna may depend on the initial conditions of the GA, including the number of elements, selection of the stimulated element, and initial spacing between the elements. Figure 5.5 contains a plot of the optimized $\Delta P_{\max}$ of the antenna as a function of the number of elements. The solid line represents the behavior for an initial spacing of $\lambda/2$. Results for antennas with 11 and 14 elements were re-analyzed for initial spacings of λ and $3\lambda/2$; the best $\Delta P_{\max}$ values are included in Figure 5.5.

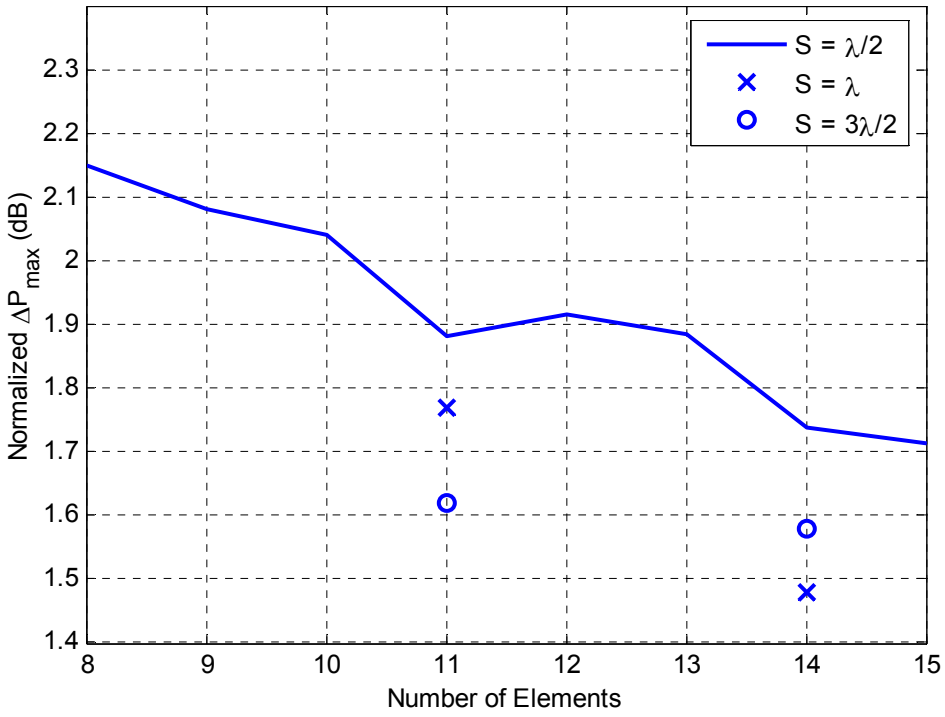

Figure 5.5: Normalized maximum pattern error as a function of the number of elements and initial spacing.

The configurations with 11 and 14 elements and an initial element spacing of 1 wavelength were chosen for further analysis of bandwidth and impedance optimization since they lie near local minima of the pattern error.

5.3.2 Bandwidth Considerations

In typical usage with earth environmental satellites, the PLMA will not require a large bandwidth; nonetheless, it should be optimized for operation within the desired downlink band. Several possible bands of operation include the S-band allocation for EES downlink (2200-2290 MHz), which has a relative bandwidth of 4%, the X-band EES downlink allocation (8025-8400 MHz, BW<5%), and the entire X-band satellite downlink allocation (7250-8400 MHz, BW<15%) [27].

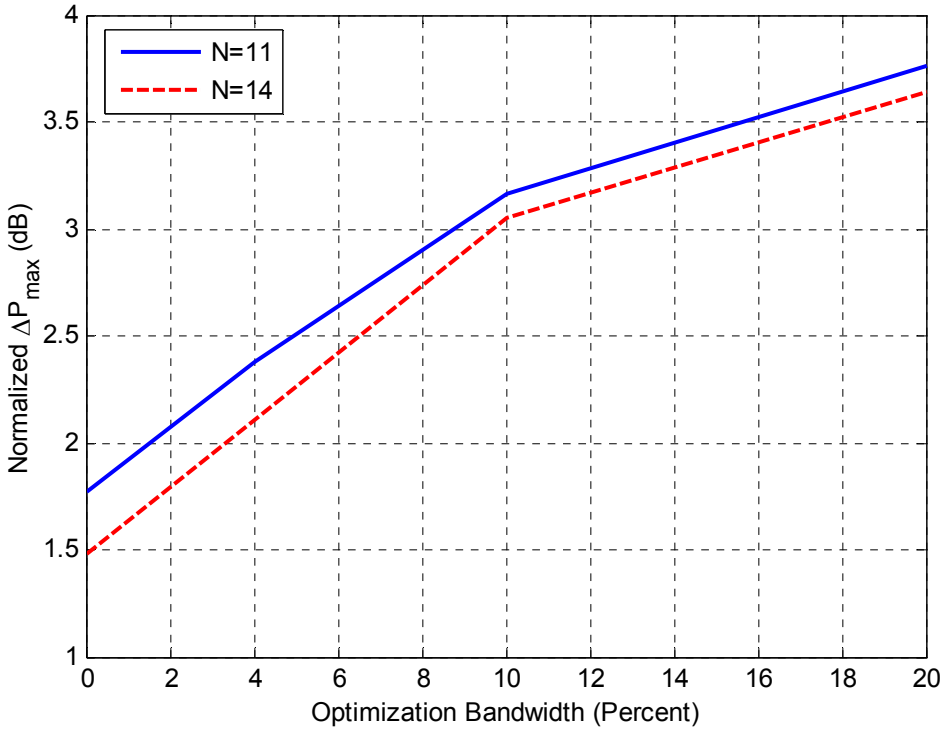

Figure 5.6: Normalized maximum pattern error versus optimization bandwidth.

Optimization trials were performed using antennas with 11 and 14 elements. The bandwidth of the antenna is optimized to match the desired bandwidth by analyzing each antenna at several frequencies within the desired bandwidth and by using the worst performing $\Delta P_{\max}$ as the representative value for pattern error. Mathematically, this is written as

$$\Delta P_{\max} = \max\left[\Delta P_{\max}(f)\right]. \qquad (5.7)$$

The resulting change in the $\Delta P_{\max}$ due to bandwidth optimization is shown in Figure 5.6. It is possible to achieve pattern match over a small bandwidth with a small impact on the antenna's $\Delta P_{\max}$; wider bandwidths noticeably degrade the pattern match of this model. Figure 5.7 contains plots illustrating the frequency-dependent performance of

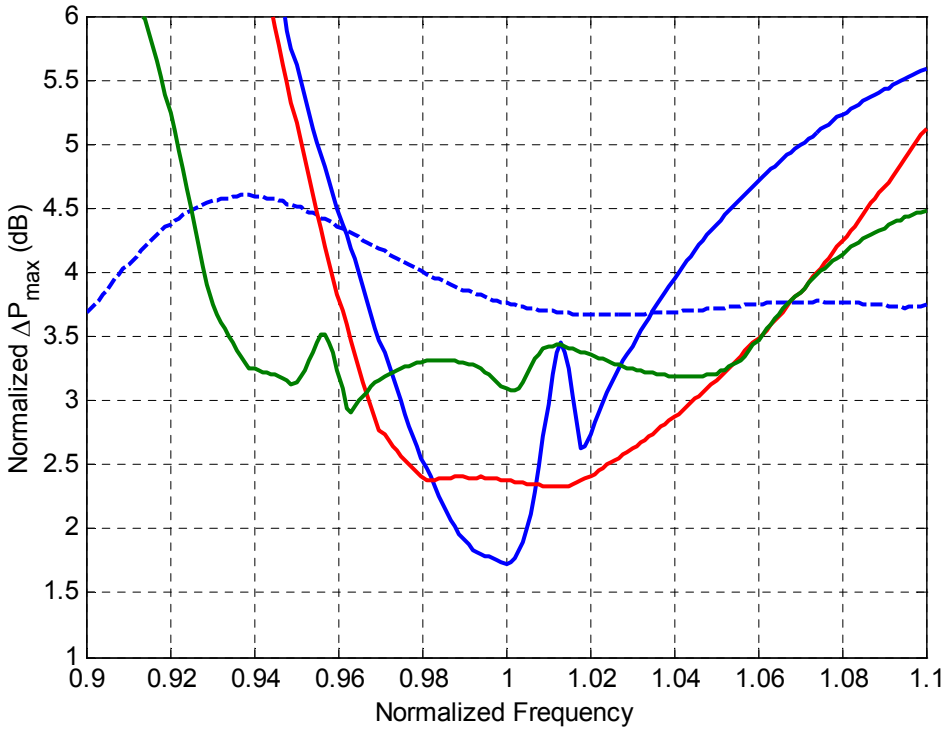

Figure 5.7: Normalized maximum pattern error as a function of frequency for PLMA designs using 11 elements and optimized for a single frequency (blue), 4% bandwidth (red), 10% bandwidth (green), and 20% bandwidth (blue-dash).

several antennas optimized for different bandwidths. While this optimization employed only three frequency points (lower edge, midband, top edge), the ripples in the performance can be reduced by increasing the number of frequency points included in the optimization process.

5.3.3 Impedance Matching Considerations

In addition to optimizing the bandwidth, it is important that the antennas be well matched. The GA constrains the impedance by altering the FOM of antennas with unsuitably high losses due to reflection, where reflection loss is defined by

$$RFL_{dB} = -10\log\left(1-\left|\Gamma\right|^2\right), \qquad (5.8)$$

where Γ is the measured reflection coefficient at the antenna terminal. The reflection loss is a more convenient quantity for analysis than VSWR because it relates directly to a degraded figure of merit for the antenna.

The 4% bandwidth antennas have a predicted reflection loss of less than 0.5 dB over their operating band, but the worst-case reflection loss increases to 2 dB as the bandwidth of the antenna increases to 20%. This is because the impedance of the antenna is dominated by the impedance of the feed element. Because the algorithm cannot effectively match the impedance of wider bandwidth antennas, such antennas require external impedance matching networks.

Basic designs of multi-stub tuners and stepped-impedance line transformers [28] were applied to the 20% bandwidth design. A GA optimized the geometry of the matching network; the effectiveness of using genetic algorithms for impedance matching has previously been demonstrated [29, 30]. The line impedances were restricted to the range of 50Ω to 100Ω, and the algorithm used simulated impedance values at each frequency. It is possible to achieve a reflection loss of less than 0.15 dB (VSWR < 1.5) using a double stub tuner or a three section stepped impedance line transformer. The reflection loss characteristics for the antennas shown in Figure 5.7 are presented in Figure 5.8, along with the reflection loss of a 20% bandwidth antenna using an optimized matching network.

5.4 Construction and Measurements

Three PLMA designs were selected for construction. These antennas each have 11 elements and were chosen from the narrow-band, 4%, and 10% bandwidth groups.

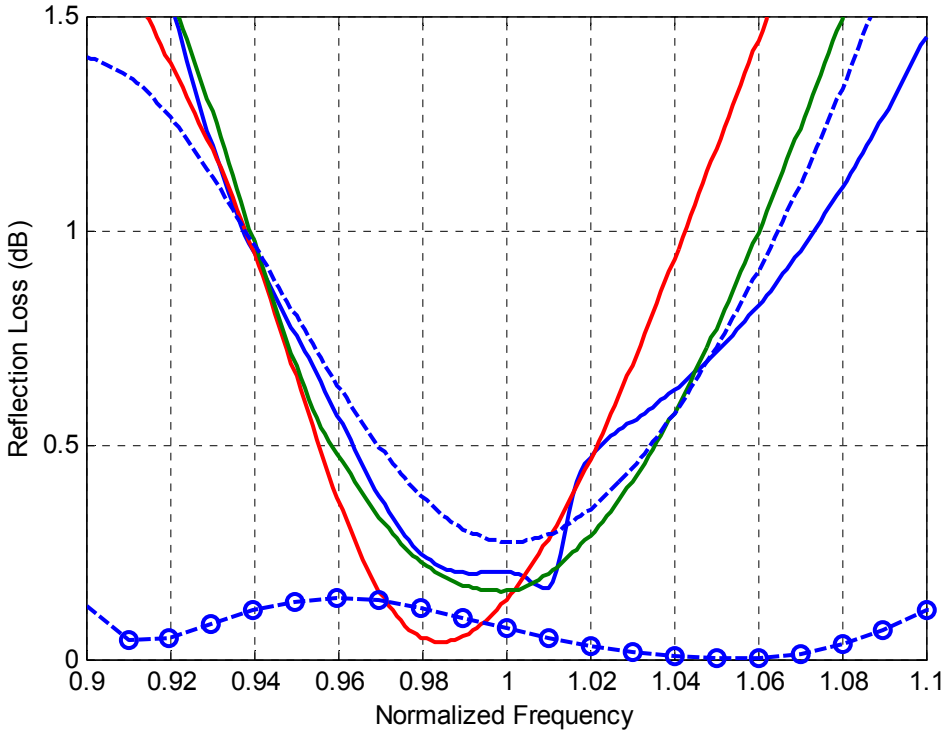

Figure 5.8: Reflection loss as a function of frequency for the same designs as Figure 5.7. Also includes the reflection loss for the 20% bandwidth antenna with an optimized matching network (circle-dash).

The selected antennas have the best FOM and lowest possible reflection loss in their groups; no matching networks were used. The narrow-band antenna was designed for a center frequency of 915 MHz and had design tolerances of 2.4 mm for the length of the elements and 10 mm for the spacing. The other two antennas were designed for a center frequency of 2245 MHz and had design tolerances of 1 mm for the length of the elements and 4 mm for the spacing. These tolerances correspond to randomly distributed errors in each dimension that yield a maximum combined FOM degradation of 1.0 dB.

These antennas were hand built using 1.6 mm-diameter brass radiating elements and a non-conductive nylon and fiberglass structure. The radiating elements are thicker

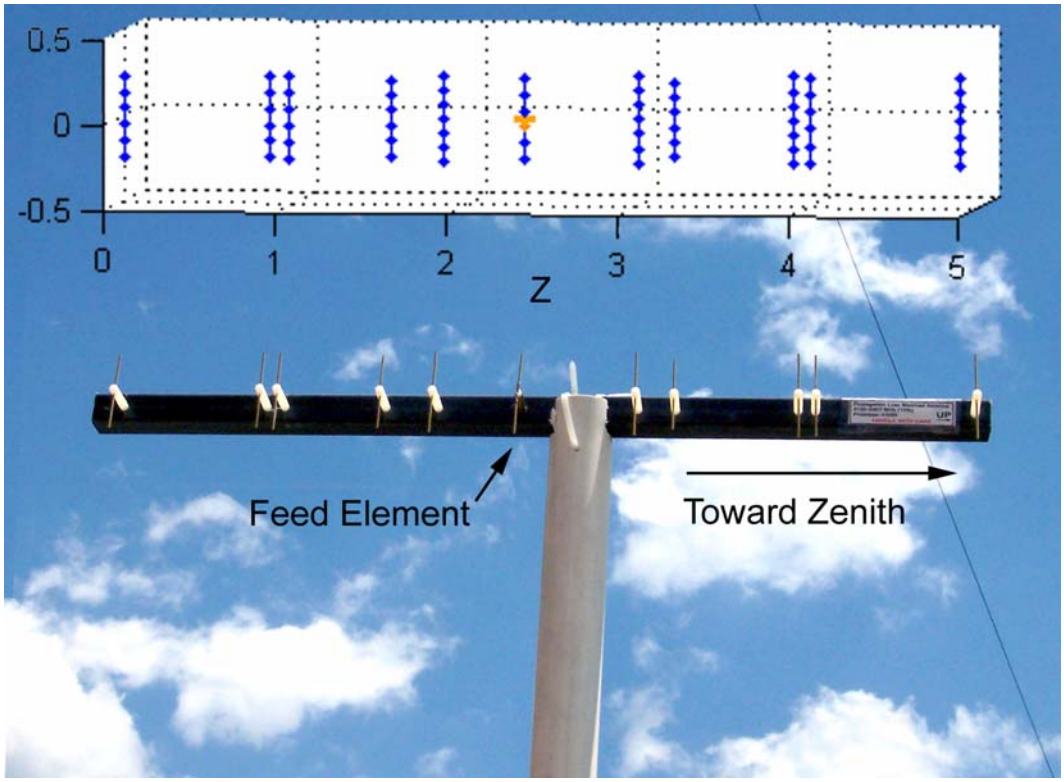

Figure 5.9: The 10% Bandwidth antenna at the Georgia Institute of Technology test range. The NEC diagram for the antenna is overlaid, with units in wavelengths.

than those used in the initial design of the antenna, and the wider radius impacts the results. The feed elements incorporated a quarter-wave bazooka balun [31]. These antennas were tested at the Georgia Institute of Technology outdoor test facility. This facility has an azimuth rotator located 8.1m away from a reference antenna mast. An image of the 10% bandwidth antenna at the facility is shown in Figure 5.9, with the NEC diagram overlaid. Although the 10% bandwidth antenna appears to have some symmetry about the feed element, this is incidental; the antenna is not symmetric.

Figure 5.10 contains plots comparing the reflection loss for the simulated and the measured 10% bandwidth antennas; the plots for the 4% bandwidth antennas are similar. The effect of the increased radius of the radiating element is evident, manifested as a

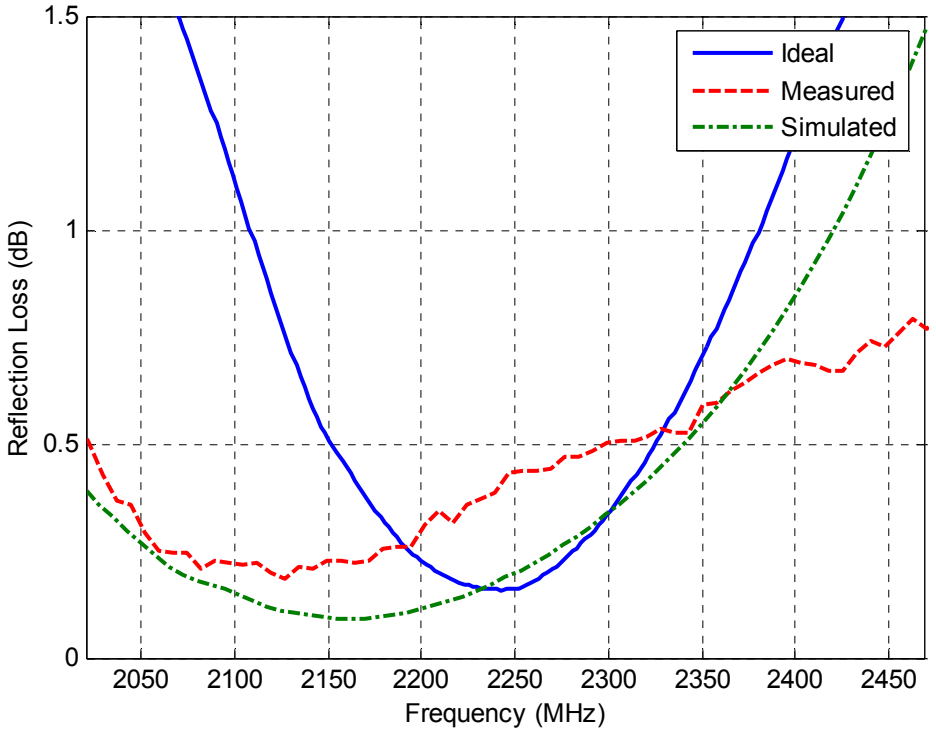

Figure 5.10: Measured reflection loss as a function of frequency of the 10% bandwidth antenna compared to that modeled for a very thin radiating element and that modeled for the radius used in the antenna tested.

wider resonance at a lower frequency. The reflection loss of the physical antenna is similar to its simulated counterpart.

A typical plot of the measured antenna pattern is shown in Figure 5.11. This plot is for the 10% bandwidth antenna, measured at the center frequency of 2245 MHz. The predicted pattern is included for reference. The main lobe of the physical antenna matches the predicted pattern, but the effects of the construction errors are evident; the two solid lines represent the front (azimuth=0°) and back (azimuth=180°) measured patterns. The most important error is the deep ripple near 65° elevation, which significantly affects the ΔP_{max} of the antenna. Further analysis with Ansoft HFSS™

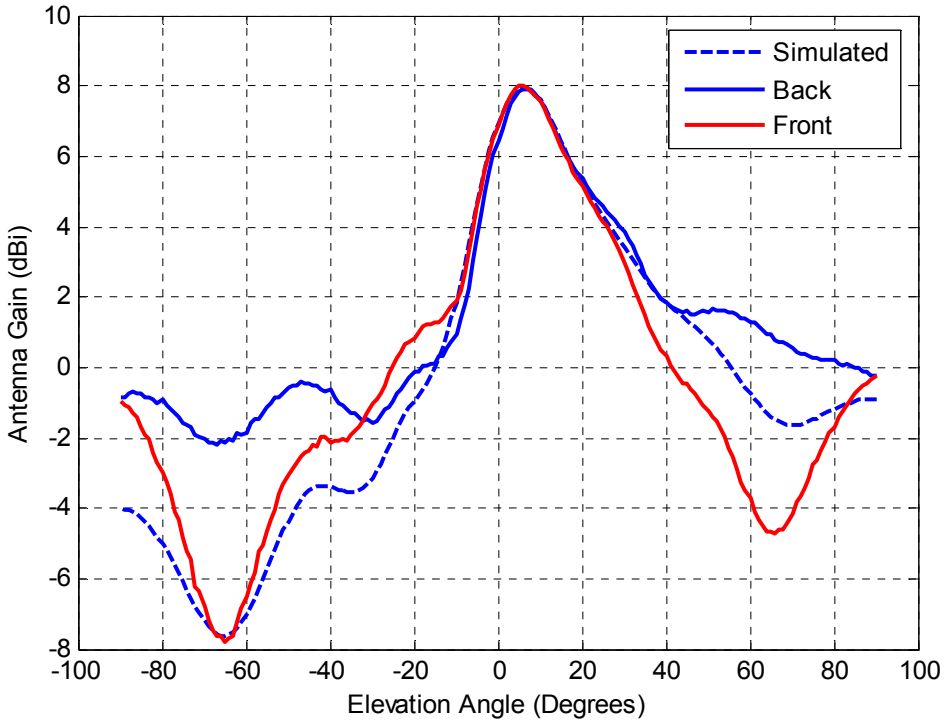

Figure 5.11: Measured pattern of the 10% bandwidth antenna compared to the simulated pattern.

confirmed that this asymmetry is because of the presence of the fiberglass structure in the high frequency antennas. A similar asymmetry was observed with the 4% bandwidth antenna but was not present in the pattern of the 915 MHz antenna.

The ΔP_{max} for this antenna is shown as a function of frequency in Figure 5.12. This data is similar to that in Figure 5.7, but it is based on the absolute gain of the PLMA and is not normalized. The predicted ΔP_{max} for the model using the actual wire radius is compared to the measured ΔP_{max} for both halves of the pattern; the measured frequencies are indicated. The effect of the pattern asymmetry is clearly seen; although one-half of the pattern matches the predicted ΔP_{max} to the limit specified by the design tolerances, the other half of the pattern does not.

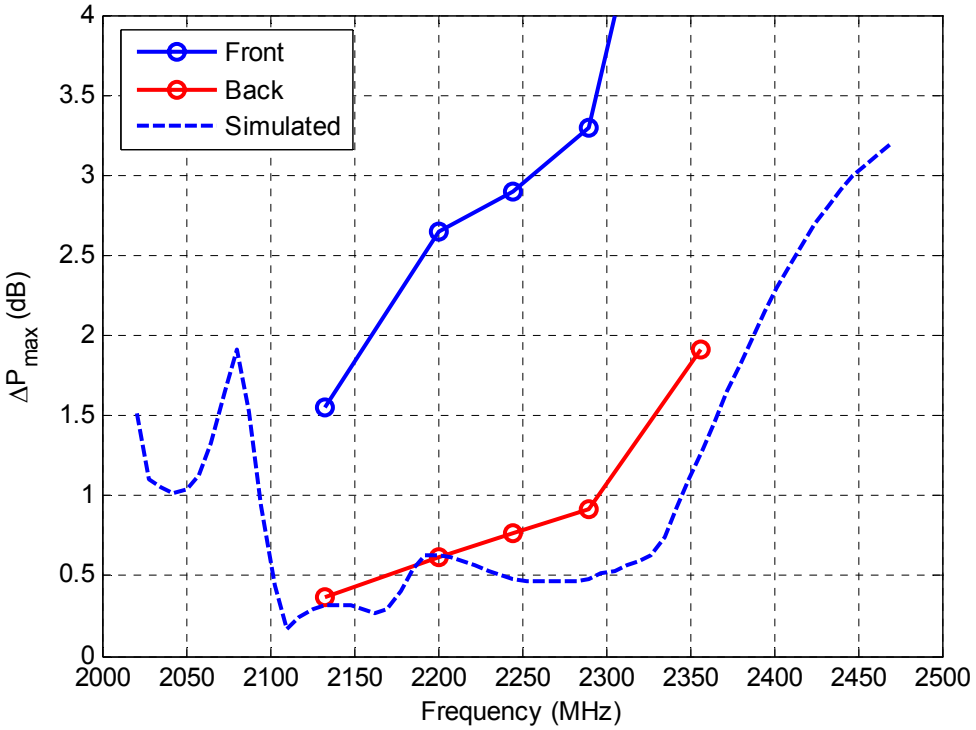

Figure 5.12: Measured pattern error of the 10% bandwidth antenna as a function of frequency as compared to the simulated value.

5.5 Antennas for the ODIN Array

The 10% bandwidth antenna was chosen as the elemental antenna for the Omni Directional Interference Nulling array (ODIN), which is to be demonstrated as a part of this research. Eight additional antennas were constructed; six of these were used in the array, and two were available as spares. These antennas utilized a printed dipole feed element with an integrated bazooka balun, as shown in Figure 5.13. The radiation pattern and impedance of these antennas were measured to ensure conformity with the design specifications. Patterns were sampled with a network analyzer at 201 frequency points

Figure 5.13: The printed dipole feed element.

between 2.0 GHz and 2.5 GHz. A summary of these measurements is contained in Appendix A.

It is noteworthy that these antennas exhibit less pattern asymmetry than the prototype antennas. The only differences between the prototype and ODIN antennas are the change in the type of feed element and the distance between the wires and the fiberglass ($\lambda/6$ for the ODIN antennas versus $\lambda/4$ for the prototypes). HFSS analysis was unable to confirm a change in the radiation pattern due to either of these factors. It is possible that fiberglass from the ODIN antennas came from a different stock than for the prototype antennas. The ODIN antennas were confirmed to operate within the design limits to the level of accuracy provided by the measurements.

CHAPTER 6.
A PROPAGATION LOSS MATCHED SPACECRAFT ANTENNA

Two drawbacks of the dipole PLMA when used in an array for satellite communications are that it is linearly polarized and that it exhibits the endfire nulls caused by the pattern of the dipoles. Using a different architecture can alleviate these problems. For example, an array of loop elements can exhibit azimuthally symmetric circularly polarized radiation patterns.

The Balanis model for a helical antenna, shown in Figure 6.1, approximates such an array of loop antennas. In the genetic helical model, each turn of the antenna has an optimized radius and height. A study similar to that performed in the previous chapter for the dipole PLMA was performed using a helical optimization model. The algorithm optimized the diameter and height of each turn in the helix. The figure of merit of the pattern match is modified by the polarization mismatch as a function of angle. The loss

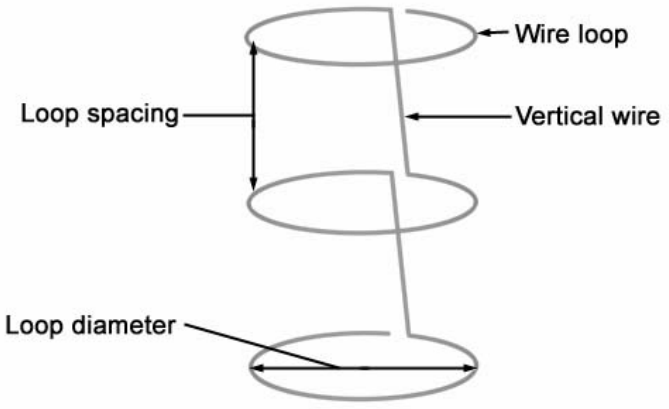

Figure 6.1: Balanis model of a helical antenna used as basis for PLMA design.

due to polarization mismatch is found by

$$L_{pol} = \frac{\left(1 \pm AR\right)^2}{2\left(1 + AR^2\right)}, \tag{6.1}$$

where the sign in the numerator is positive for matching to RHCP and negative for matching to LHCP. The axial ratio, AR, varies between ± 1 and is found during NEC analysis.

Rather than analyzing a ground station antenna in this study, the properties of the PLMA were applied to an antenna for use onboard a LEO satellite. This is advantageous because although a ground station requires many elemental antennas to achieve the data rates required by LEO downlinks, the satellites themselves sometimes use a single, downward (nadir) oriented antenna than has a very wide beam, in order to provide data to many possible ground stations simultaneously. The main difference between a PLMA for ground station use and a PLMA for spacecraft use is the required viewing range of the antenna. For a LEO satellite in an orbit 707 km above the surface of the earth, a ground station located in the direction of $62°$ from nadir (as observed from the satellite) will observe the satellite at a local elevation angle of $5°$. The propagation loss exhibited by the communications link can be expressed a function of the angle from nadir using the relationship

$$\theta = 180° - \gamma - El, \tag{6.2}$$

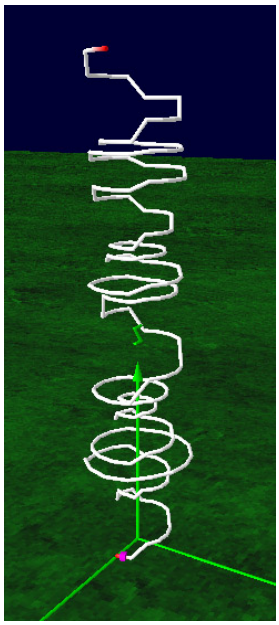

Figure 6.2: Computer drawing of a genetic helix for spacecraft use.

as was illustrated in Figure 2.2. The propagation loss as a function of the angle from nadir follows a similar curve as that presented in Figure 5.1 for the propagation loss as a function of elevation, but is compressed to a $62°$ range of angles as opposed to the $85°$ range for a ground station.

The antenna architecture in this study incorporates a ground plane and the feed is located at the ground plane. An image of the resulting antenna is shown in Figure 6.2. The simulated characteristics of this antenna indicate that it radiates circular polarization over the entire beam and has a polarization mismatch of less than 0.1 dB at most angles. A plot of the polarization mismatch is shown in Figure 6.3. The radiation pattern is nearly azimuthally symmetric, and the overall pattern match, $\Delta P_{\max}$, is about 2.0 dB. The construction of such an antenna is a subject for further research.

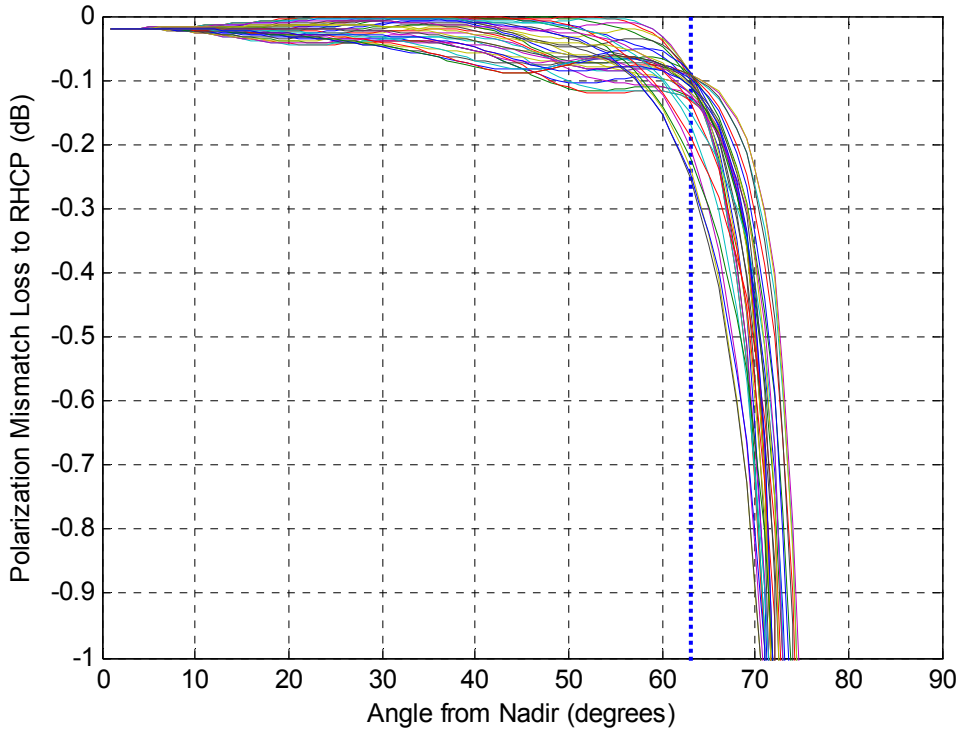

Figure 6.3: Calculated polarization mismatch versus angle. The vertical line at $62°$ indicates the maximum use angle from nadir, corresponding to $El_{\min} = 5°$. Plotted for azimuth slices between $0°$ and $350°$ in $10°$ increments.

CHAPTER 7.
MULTIFEED PLMA WITH SIDELOBE SUPPRESSION

7.1 Introduction

Because the previously described dipole PLMA is parasitic and operates over a wide range of angles, the proximity of other identical antennas affects its impedance and radiation pattern. This chapter focuses on a modification of the genetic Yagi design in which multiple driven elements are included in an antenna array. The array is designed so that it consists of many concatenated identical subarrays, as shown in Figure 7.1. These subarrays, termed "array tiles," each consist of a number of parasitic elements and driven elements (feeds). These driven elements will be placed at intervals greater than $\lambda/2$, so this model also incorporates a method of reducing the grating lobes (aliasing during beamforming) of the array. More information on methods to reduce grating lobes is included in Part 3 of this dissertation.

The array tile is optimized so the radiation pattern of each feed is similar to the desired radiation pattern. The tile is simultaneously optimized so the array exhibits low

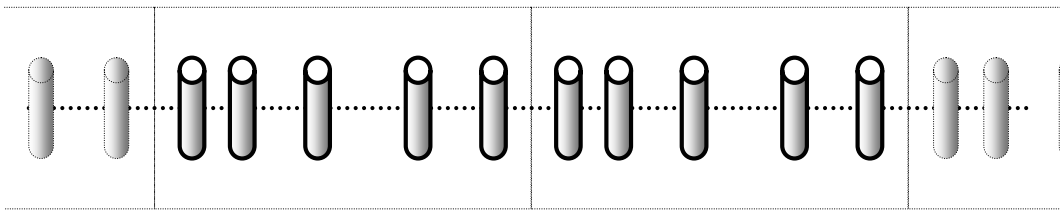

Figure 7.1: Concept of a concatenated array. The dotted boxes indicate the individual tiles, and radiating elements are shown as cylinders.

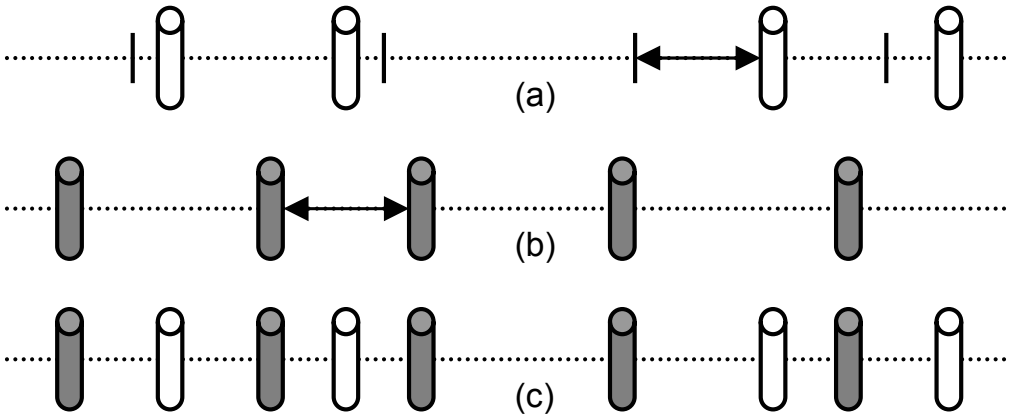

Figure 7.2: Representation of element positions in the array tile, showing the feed positions (a), parasitic element positions (b), and the combined array tile (c).

sidelobe levels. Optimizing an array tile has several advantages compared to optimizing a single parasitic antenna for an array. First, each parasitic element contributes to the radiation pattern of many feeds, so the number of parasitic elements is reduced. Second, the presence of other feeds is implicit in the design, so the interactions between feeds are known and optimized.

The GA used in this analysis contains three genes, as opposed to the two used in the development of the PLMA. The first determines the positions of the feeds within the array as compared to their proximal grid point, as shown in Figure 7.2a. The second describes the positions of the parasitic elements as compared to their nearest neighbor, as shown in Figure 7.2b. The third gene determines the length of each element. The size of each tile, the number of feeds, and the maximum number of parasitic elements per tile are determined prior to the execution of the algorithm.

The fitness of individuals within the algorithm is given by

$$FOM = -\left(W_P \cdot \Delta P_{\max} + W_{RSLL} \cdot \Delta RSLL_{\max}\right). \qquad (7.1)$$

The algorithm maximizes the fitness of the population. The value $\Delta P_{\max}$ represents the quality of the radiation pattern synthesis, and is defined in Equation 5.5. The value $\Delta RSLL_{\max}$ represents the degree to which the predicted relative sidelobe levels (RSLL) exceed the desired sidelobe level. The calculation of sidelobe levels is described in more detail in Chapter 9. The values W_P and W_{RSLL} control the relative weighting of the sidelobe level and the radiation pattern. Values of $W_P = 1$ and $W_{RSLL} = 0.5$ were used so that the algorithm emphasizes the pattern match over the sidelobe level.

7.2 Theory

7.2.1 Radiation Pattern Synthesis

Many choices are possible for the desired radiation pattern of the feeds. For ease of presenting this model, two cases were analyzed in which the desired radiation pattern is constant over a range of angles and zero elsewhere. The scan range of the array is limited to the high gain region. In the first case, the tile operates between $-30°$ and $+30°$ from broadside; in the second case, the range is limited to $\pm 15°$ from broadside.

The algorithm represents the position of each parasitic element using the offset from the position of the previous element, as shown in Figure 7.2b. The minimum distance between any two elements, fed or parasitic, is $\lambda/10$. The maximum number of parasitic elements is defined prior to the execution of the algorithm, which uses fewer parasitic elements by positioning unwanted parasitic elements outside the array tile, where they are removed from the analysis.

The array tile is analyzed using NEC [11]. In its current implementation, the algorithm analyzes an array consisting of three tiles. This number can be increased, but elements more than a few wavelengths from a feed do not contribute significantly to the radiation pattern. A value $\Delta P_{\max}(n)$ is assigned to each feed as in the single feed analysis of the PLMA. The worst performing of these is selected as the representative value for a tile, using

$$\Delta P_{\max} = \max\left[\Delta P_{\max}(n)\right]. \tag{7.2}$$

This value is used in Equation. (7.1) to determine the FOM of each array tile.

7.2.2 Sidelobe Level Optimization

The feeds in this antenna array are spaced at intervals greater than a half-wavelength. This allows the algorithm freedom to place the parasitic elements and increases the resolution of the array. A genetic algorithm optimizes the positions of these feeds to prevent grating lobes in the radiation pattern of the array. Methods for reducing the sidelobe levels of aperiodic phased arrays are discussed in more detail in Part 3.

Although the sidelobe levels are optimized in parallel with the radiation pattern, the process can be described separately. The positions of the feeds are described by a gene that is independent from the positions of the parasitic elements. This gene contains values describing the distance of each feed from its proximal grid point, as shown in Figure 7.2a. The number of feeds per tile and distance between proximal grid points are both defined before the execution of the algorithm.

The sidelobe level is determined from a radiation pattern in which the effect of the gain of each feed is removed. This pattern is given by

$$G(\theta_t, \theta_s) = \left[\mathbf{a}(\theta_t) \cdot \mathbf{x}(\theta_s) \Big/ \sum_{i=1}^{n} \left| \mathbf{x}_i(\theta_s) \right| \right]^2, \qquad (7.3)$$

where $\mathbf{x}(\theta_s)$ is a vector containing the complex response of each feed as a function of the stimulus incidence angle θ_s, and the vector $\mathbf{a}(\theta_t)$ contains phase-only steering vectors corresponding to a target angle θ_t. The maximum value of G over θ_s, exclusive of the main lobe, defines the relative sidelobe level for a target angle θ_t. This normalization is required to infer the sidelobe level of the beamformer; if a sidelobe is 20 dB down from the main lobe, but 18 dB is due to the pattern of the antennas and only 2 dB is due to the resolution of the beamformer, the beamformer cannot effectively null signals within the sidelobe. Furthermore, it is necessary to analyze the pattern from various stimuli and target angles, θ_s and θ_t, because the pattern of the array changes significantly with beam steering. Pattern space techniques applied to arrays of identical feeds, such as those discussed in Chapter 9, are not applicable to this array tile.

The algorithm uses the equation

$$\Delta RSLL_{\max} = \max\left[RSLL_{dB}^{ideal}, RSLL(\theta_t)_{dB}^{actual} \right] \qquad (7.4)$$

to describe the degree by which the worst case sidelobe level exceeds the ideal sidelobe level. This value of $\Delta RSLL_{\max}$ is used in Equation (7.1) to determine the FOM of the array tile.

The GA calculates sidelobe levels for arrays with six concatenated tiles. This yields better sidelobes than optimizing a single tile alone and concatenating the result to form the array, as illustrated in Figure 7.3. Predicted patterns are plotted for tiles using four feeds with 0.75λ average spacing between the feeds. A concatenated array

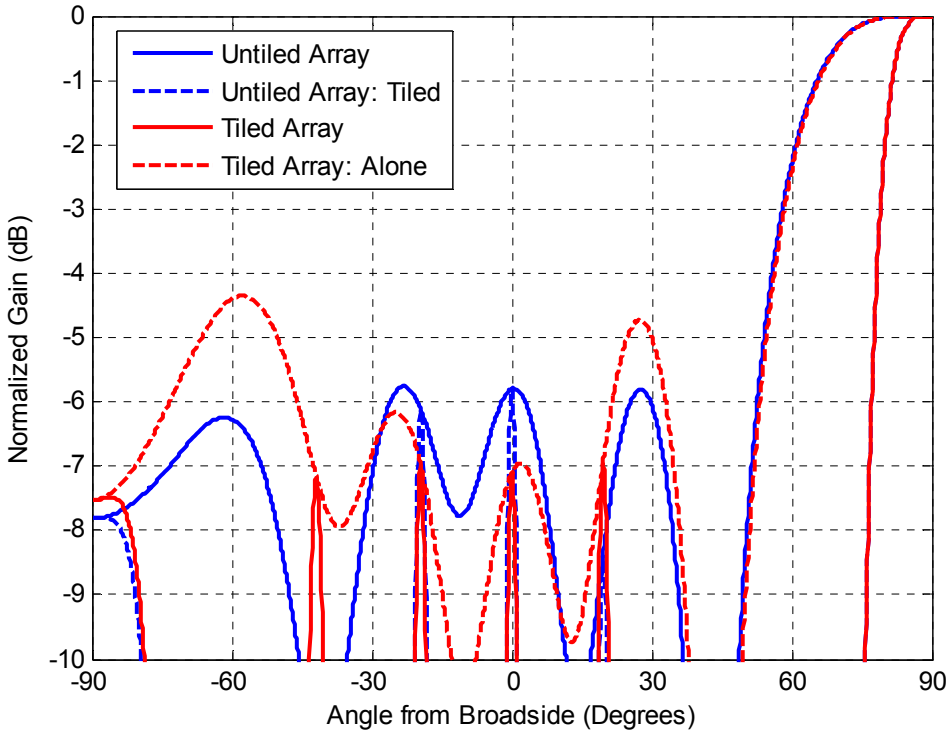

Figure 7.3: Array factor radiation patterns for optimized tiled and untiled arrays.

consisting of individual tiles that were not were not generated with a tiled algorithm does not have substantially lower sidelobes than a constituent tile, resulting in less than optimal performance. Additionally, a solution from a tiled algorithm exhibits significantly higher sidelobes when than its concatenated array when analyzed alone.

Figure 7.4 has plots comparing the effect of the number of feeds per tile and number of tiles on the optimized sidelobe level of the array. These were created by analyzing simple tiles of identical isotropic radiators using a grid spacing of 0.75λ and an end-fire optimization scan angle.

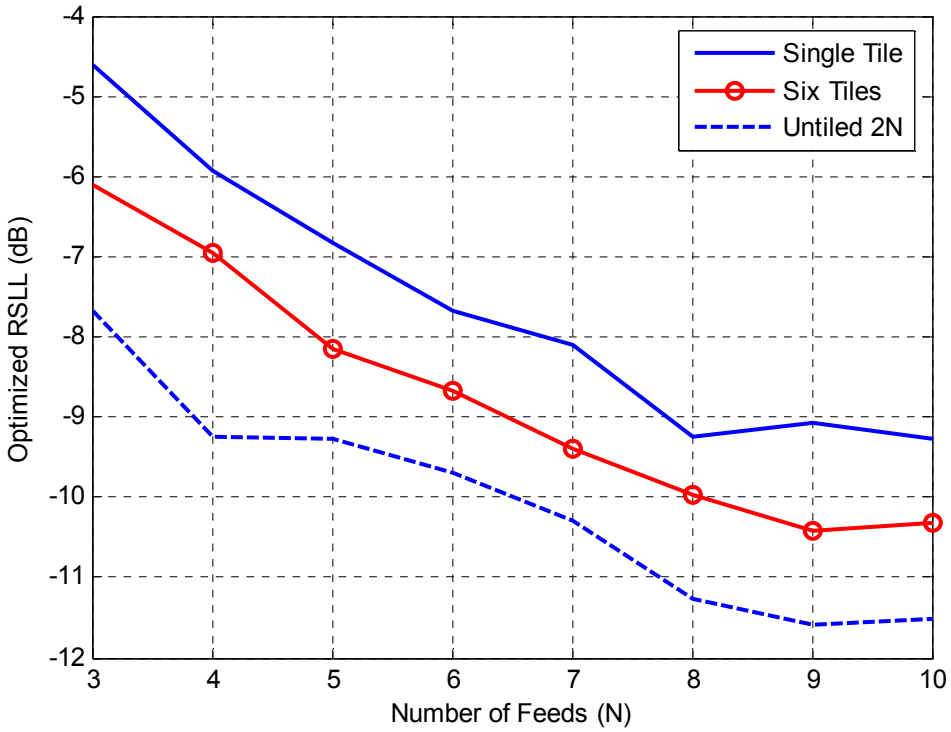

Figure 7.4: RSLL versus N for a single tile, six tiles, and a single tile with $2N$ feeds.

7.3 Design Optimization Results

The GA was applied to tiles using operating ranges of ±30° and ±15° from broadside. These tiles are 1.5λ long and have two feeds, resulting in an average feed spacing of 0.75λ. These tiles also used a maximum of nine parasitic elements. The following results were the best observed in several trials of the algorithm.

Figs. 7.5 through 7.7 contain results from the design algorithm. Diagrams of the tile configurations for both ±30° and ±15° tiles are shown in Figure 7.5. Plots of the predicted radiation patterns and sidelobe level for the ±15° tile are contained in Figure 7.6. Similar data for the ±30° tile is contained in Figure 7.7.

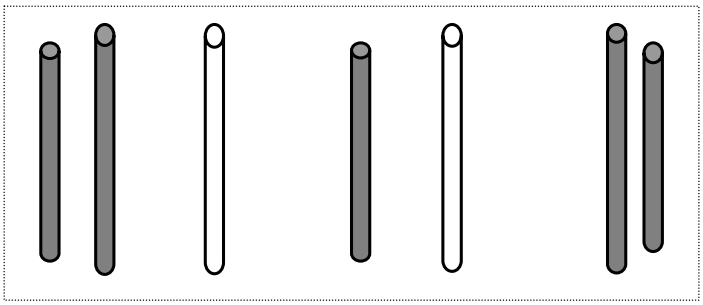

(a)

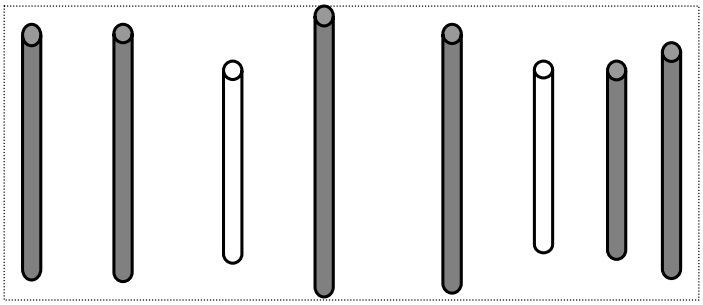

(b)

Figure 7.5: The optimized tile configurations for the ±30° (a) and ±15° (b) arrays. Feeds (white), parasitic elements (gray) and the tile boundary are indicated.

The predicted radiation patterns of the feeds in both tiles approximate the ideal pattern over the scan range. The algorithm also optimizes the sidelobe levels over the scan range. The worst-case predicted sidelobe levels are -5.0 dB and -7.8 dB for the ±30° and ±15° tiles, respectively. These results should improve as the number of feeds per tile increases.

This model can be modified to include the impedance and bandwidth optimizations of Chapter 5. Additionally, the concepts can be applied to other genetic antenna models to produce many designs, such as a binary patch antenna with multiple feeds. These modifications, and a physical demonstration of an array designed by this method, are potential subjects for further research.

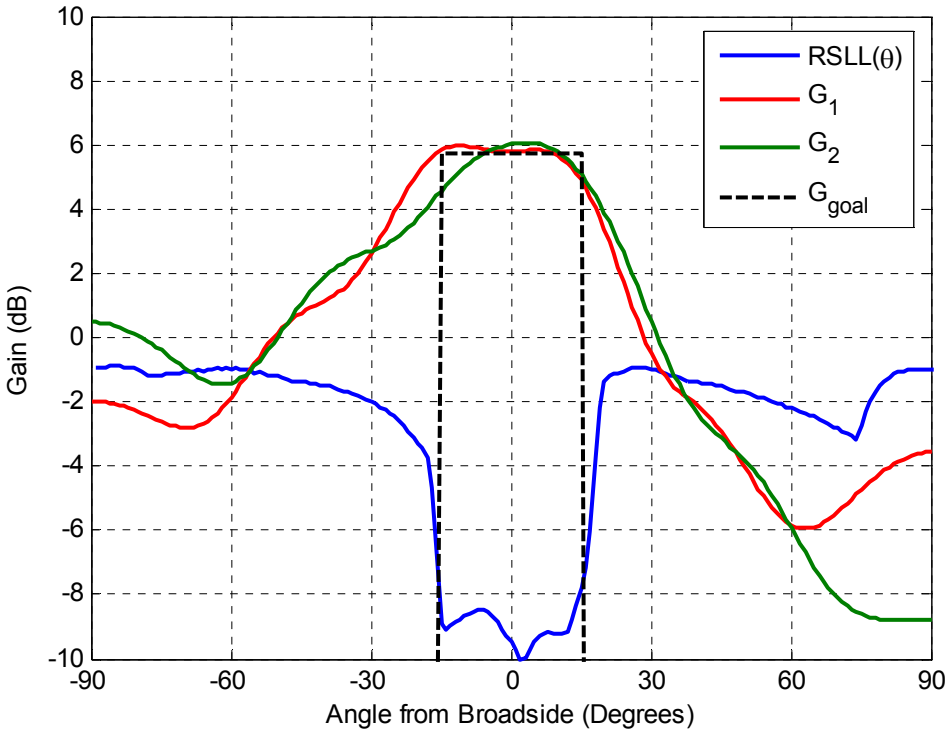

Figure 7.6: Feed radiation patterns and RSLL versus scan angle for the $\pm 15^{\circ}$ tile.

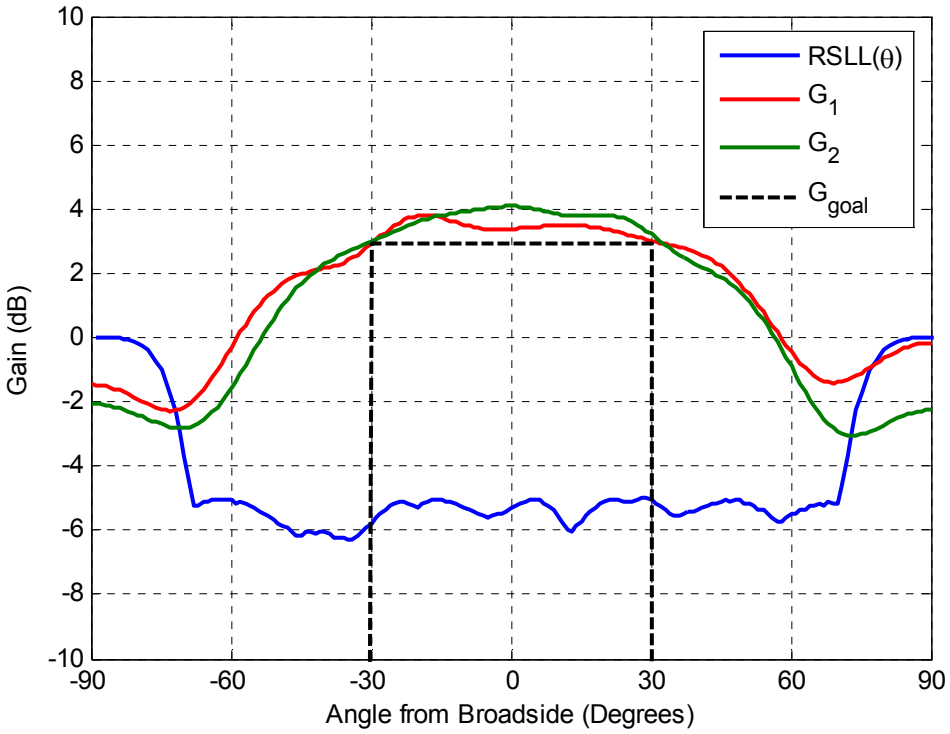

Figure 7.7: Feed radiation patterns and RSLL versus scan angle for the $\pm 30°$ tile.

Part 3:

Array Optimization

CHAPTER 8.
APERIODIC AND THINNED PHASED ARRAYS

8.1 Introduction

A phased array is a collection of elemental antennas whose outputs (or inputs) are weighted, phase shifted, and combined to create a radiation pattern for the array that is different from the radiation pattern of an elemental antenna. The phased array often has more gain and a narrower beamwidth than an elemental antenna, and techniques can be used to null interfering signals from the resulting output signal. Ordinarily, the maximum gain of the phased array is N times the gain of an elemental antenna comprising the array, where N is the number of antennas within the array. The maximum resolution of the array is determined by the size of the aperture in which the elemental antennas are distributed.

Sometimes, phased arrays require a large aperture but a small number of antennas. Placing these antennas at periodic intervals exceeding one half wavelength, or $\lambda/2$, creates grating lobes in the radiation pattern and limits the usefulness of the array. Aperiodic placement techniques can remove grating lobes and minimize the sidelobe levels of the array, as shown in Figure 8.1 [17]. This topic was discussed briefly in Chapter 7 in regard to the minimization of sidelobes of the Multifeed PLMA.

Theories of aperiodic arrays have been described in detail [32-33]. For example, Haupt showed the relationship between the unit circle representation and antenna positions for aperiodic arrays [34]. However, it is difficult to apply constraining requirements to arrays designed using this method or other deterministic methods [35,

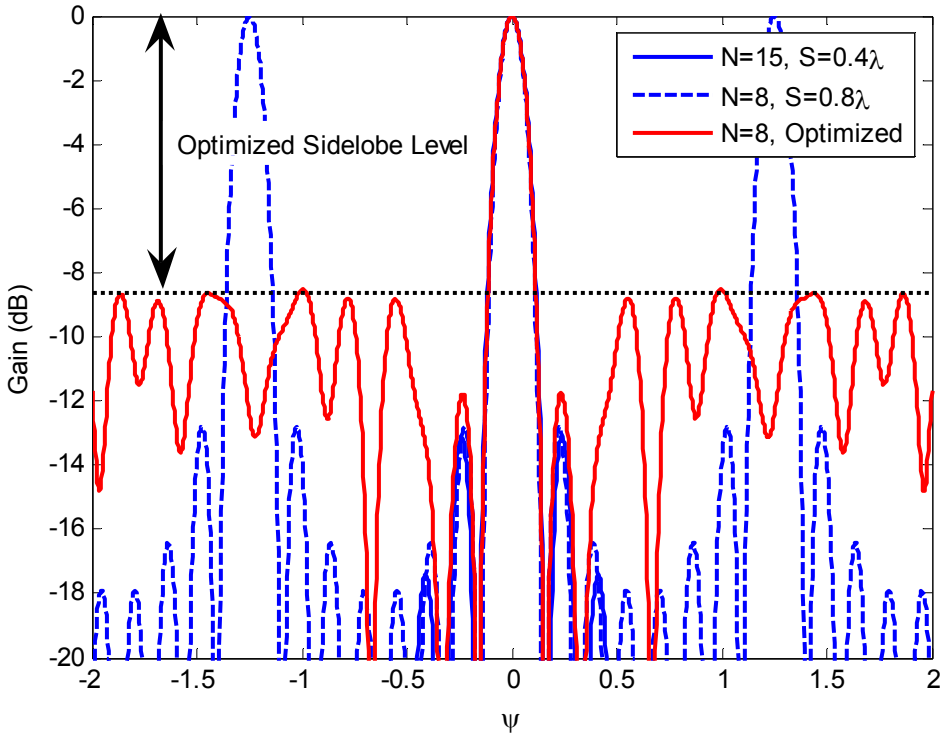

Figure 8.1: Radiation patterns illustrating grating lobe reduction. Plotted for arrays of N antennas with the indicated intervals between antennas. Each of these arrays occupies the same aperture size and has the same main lobe beamwidth.

36]. As a result, iterative search algorithms, such as genetic algorithms, are often used to determine antenna positions in an aperiodic array.

The usefulness of genetic algorithms as optimization tools in aperiodic linear array design has been demonstrated [16, 17]. However, little attention has been given to their application to the design of volumetric arrays or to arrays in which constraints are placed on the antenna positions. Volumetric or other three dimensional array configurations are advantageous for any phased array system used for horizon-to-horizon communications, because arrays limited to the *xy*-plane exhibit resolution loss at elevation angles below $45°$. This is undesirable because it limits the ability of the system

to provide accurate direction finding estimates and to null interferers adjacent to desired sources near the horizon.

Whereas the research described in the previous chapters focused on the development of elemental antennas for use in a phased array, the research described in the following chapters focused on the optimization of the array itself. Three specific areas investigated include pattern-space representations of array radiation patterns, alias differentiation during tracking with volumetric arrays, and efficient FFT beamforming and independent null steering using aperiodic arrays.

CHAPTER 9.
UVW SPACE AND THINNING VOLUMETRIC ARRAYS

9.1 Introduction

Although the optimization of aperiodic arrays has been well studied (e.g. [32 - 37]), several subjects in this field have been neglected. First, pattern-space representations of the radiation pattern of linear arrays are well known (for example, as in Stutzman [11] or Hansen [12]), but pattern-space representations are ignored in the optimization of aperiodic planar arrays. Furthermore, no pattern-space representation or aperiodic optimization data exists for volumetric arrays, using pattern-space representations or otherwise. A second area that has been neglected is the study of aperiodic array optimization when the minimum distance between adjacent elemental antennas is restricted. Such a restriction can arise from the physical size of the elemental antenna or the desire to reduce mutual coupling between elemental antennas.

Both of these areas have been studied extensively in this research. Results are presented from a mathematical analysis of the pattern-space representation and from results using GA optimization of the arrays. The GA employed uses a continuous gene to describe antenna positions, as in [16], instead of Boolean values describing the presence or absence of an antenna at a grid point, as in [17]. Characteristics of the GA are shown in Table 9.1. Each trial repeats many times to ensure statistical reliability of the results. The inverse of the maximum relative sidelobe level (RSLL) defines the fitness of individuals within the GA [17]. The algorithm maximizes the fitness of the population and as a result minimizes the sidelobes exhibited by an array.

Table 9.1:
Genetic Algorithm Characteristics for the Aperiodic Array Optimization

Characteristic	Value
Population Size	110 Individuals
Advancement	Best 50 of Total Population
Spawning Methods	30 by Mutation 20 by Crossover 10 by Mutation and Crossover
Continuous Genes	1: *X*-Coordinate (Linear Array) 2: *XY*-Coordinates (Planar Array) 3: *XYZ*-Coordinates (Volumetric Array)
Maximum Mutation	0.2λ (Position)
Termination Condition	20 Generations Without Improvement

9.2 Calculating the Maximum Sidelobe Levels

9.2.1 Determining Sidelobe Levels

The complexity in predicting the relative sidelobe level (RSLL) of an array (the metric of performance) requires an efficient method of analysis. This involves determining the radiation pattern and finding the maximum value exclusive of the main lobe. For a linear array, the pattern is optimized at a maximum selected scan angle, which results in optimization at smaller angles down to broadside [16, 37]. However, because the width of pattern lobes changes as a function of angle, a simple algorithm can erroneously report the main lobe as a sidelobe, as shown in Figure 9.1. This error probably led to the finding in [16] that linear arrays cannot be optimized for endfire pointing. Uniform sampling of the pattern as a function of angle [16] also causes oversampling of the endfire lobes and reduces the speed of the algorithm.

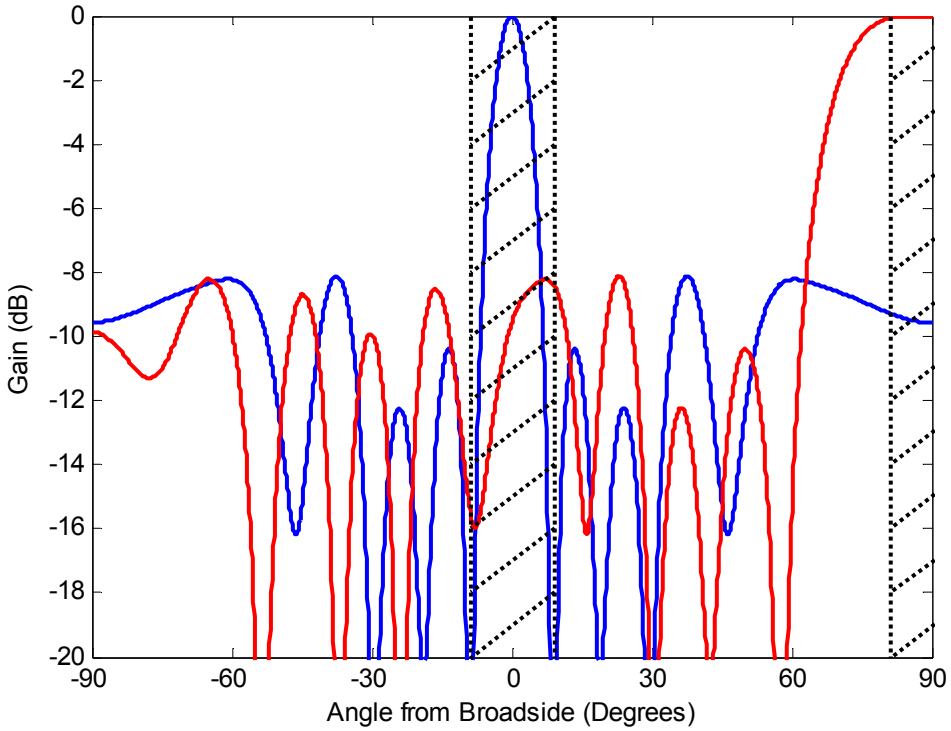

Figure 9.1: Radiation pattern as a function of angle for a linear array. The main lobe of the endfire-pointed array extends past the allotted window (shaded).

9.2.2 Using a Pattern-Space Representation

Instead of representing the radiation pattern as a function of the angle of arrival, it is better to represent the radiation pattern in pattern-space during the optimization, as in [17]. The pattern-space representation, such as that shown in Figure 9.2, is found by examining the mathematical form of the beamformer. The beamformer is given by $\mathbf{y} = \mathbf{a}^H \mathbf{x}$, where $\mathbf{y}$ is the output beam and $\mathbf{a}^H$ is the Hermitian (complex transpose) of the steering vector. The vector $\mathbf{x}$ consists of the antenna phasors written as

$$\mathbf{x}_i = \exp\left[jk \left(X_i \cos\phi \sin\theta + Y_i \sin\phi \sin\theta + Z_i \cos\theta \right) \right], \quad (9.1)$$

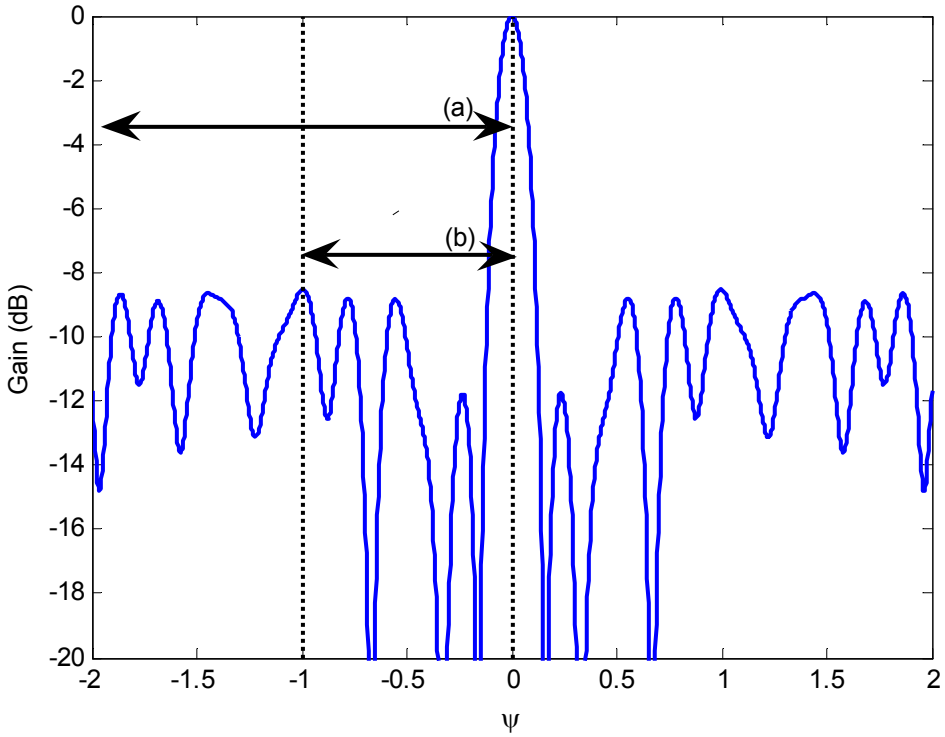

Figure 9.2: Pattern-space representation for a linear array. Scan range limits indicated for endfire optimization (a) and broadside optimization (b).

where $k = 2\pi/\lambda$, ϕ and θ represent the angles of arrival of a signal, and X_i, Y_i, and Z_i represent the position of the i_{th} elemental antenna out of N total antennas.

Using primed angles ϕ' and θ' to indicate the steering direction, the steering vector is written as

$$\mathbf{a}_i^H = \exp\left[-jk\left(X_i \cos\phi' \sin\theta' + Y_i \sin\phi' \sin\theta' + Z_i \cos\theta'\right)\right]. \quad (9.2)$$

Abbreviating the functions $c_\theta = \cos\theta$ and $s_\theta = \sin\theta$ and writing the beamformer yields

$$\mathbf{y} = \sum_{i=1}^{N} \exp\left\{jk\left[\begin{array}{r} X_i\left(c_\phi s_\theta - c'_\phi s'_\theta\right) + Y_i\left(s_\phi s_\theta - s'_\phi s'_\theta\right) \\ + Z_i\left(c_\theta - c'_\theta\right) \end{array}\right]\right\}. \quad (9.3)$$

In the case of a linear array positioned on the *y*-axis, the equation simplifies to

$$\mathbf{y} = \sum_{i=1}^{N} \exp\left\{ jk\left[Y_i \left(s_\phi - s'_\phi \right) \right] \right\}. \qquad (9.4)$$

It is helpful to use the substitution $\Psi = s_\phi - s'_\phi$ [12], which is unitless and has the range $\Psi = -\left(s'_\phi \pm 1 \right)$ for a total range of ± 2. The magnitude of (9.4) is symmetric about the main beam at $\Psi = 0$.

The optimization algorithm evaluates (9.4) between $\Psi = 0$ and $\Psi = 1 + \sin\phi'$, where ϕ' is the maximum scan angle, as shown in Figure 9.2. The substitution of Ψ improves the speed of the algorithm and eliminates varying lobe sizes. The pattern-space beamwidth of the main lobe is estimated from the aperture size, $BW \approx 1 \Big/ \left(N\overline{S} \right)$ [12], where $\overline{S}$ is the mean spacing between antennas in wavelengths. Like other pattern-space quantities, the beamwidth is unitless.

9.2.3 Planar Arrays

A similar UV substitution is used to represent the pattern-space of planar arrays. The planar case of (9.3) is

$$\mathbf{y} = \sum_{i=1}^{N} \exp\left\{ jk\left[X_i \left(c_\phi s_\theta - c'_\phi s'_\theta \right) + Y_i \left(s_\phi s_\theta - s'_\phi s'_\theta \right) \right] \right\}. \qquad (9.5)$$

By defining the pattern-space $\Delta u = u - u' = c_\phi s_\theta - c'_\phi s'_\theta$ and $\Delta v = v - v' = s_\phi s_\theta - s'_\phi s'_\theta$, the maximum extent of these variables is the circle $\Delta u^2 + \Delta v^2 = 4$. For any steering angle, the radiation pattern is defined by a circle of radius 1 within the pattern-space, as shown in Figure 9.3.

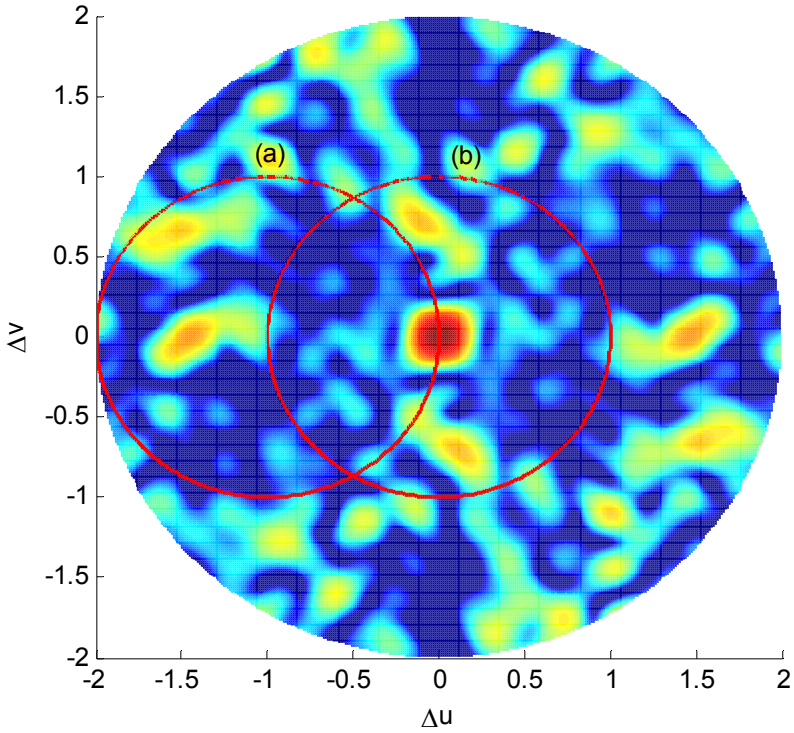

Figure 9.3: Pattern-space representation for a planar array. The circles indicate the pattern exhibited by the array when it is steered to the horizon (a) and to zenith (b). Plotted for a 5x5 array with 0.75λ average spacing between antennas. The color scale is from -20 to 0 dB relative to the main lobe.

9.2.4 Volumetric Arrays

Randomly distributed volumetric arrays have been previously studied [38-41]. Ender's Crow's Nest Antenna [39] is a practical example of a randomly distributed volumetric array. Voles showed methods of radiation pattern optimization for spherical shell arrays [40]. More recently, Carr and Tittensor demonstrated a volumetric array using an optical feed network [41], avoiding scattering from traditional coaxial feed networks. However, optimization algorithms for reducing the sidelobes of volumetric arrays have not been applied, and no pattern-space substitution analyses of volumetric arrays have been reported. A UV, or in this case UVW, substitution analysis is not

intuitive for volumetric arrays because the radiation pattern of such an array changes dramatically during beam steering. Without simplification, optimization of a volumetric array requires a four-dimensional analysis for radiation pattern and scan angle.

The simplification can be applied by representing the beamformer as

$$\mathbf{y} = \sum_{i=1}^{N} \exp\left[jk\left(X_i \Delta u + Y_i \Delta v + Z_i \Delta w \right) \right], \tag{9.6}$$

where $\Delta w = c_\theta - c'_\theta$. For a given steering direction, there are two orthogonal angles in the far field pattern (ϕ, θ), so the values Δu, Δv, and Δw are not independent. Coordinate triplets must satisfy the equation $u^2 + v^2 + w^2 = 1$. Because $\Delta u = u - u'$, this is rewritten as

$$\left(\Delta u + u'\right)^2 + \left(\Delta v + v'\right)^2 + \left(\Delta w + w'\right)^2 = 1. \tag{9.7}$$

Therefore, the set of valid triplets $(\Delta u, \Delta v, \Delta w)$ is described by the surface of a sphere of radius 1 centered at $-(u', v', w')$, or $-\left(c'_\phi s'_\theta, s'_\phi s'_\theta, c'_\phi\right)$. Changing the steering direction translates the center of this sphere and, consequently, the set of valid triplets $(\Delta u, \Delta v, \Delta w)$. Notably, the equation $u^2 + v^2 + w^2 = 1$ remains unchanged.

When considering all possible steering directions (ϕ', θ'), the set of all possible values of $(\Delta u, \Delta v, \Delta w)$ is contained within the volume of the sphere $\Delta u^2 + \Delta v^2 + \Delta w^2 = 4$. This volume defines a three-dimensional pattern-space. For any particular steering angle, the radiation pattern of the array corresponds to the intersection of the pattern-space with the surface of the sphere defined by Equation (9.7). Figure 9.4 shows this concept. The translation of this sphere through the pattern-space causes the

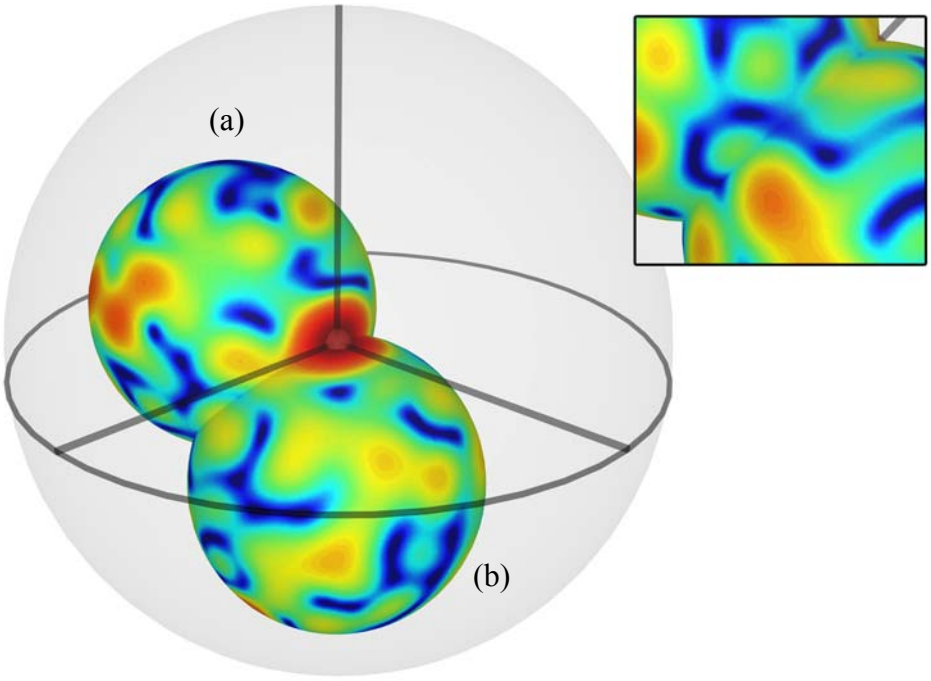

Figure 9.4: Pattern-space representation for a volumetric array. Two spheres intersect the main lobe at the origin, and indicate patterns for an array steered to the horizon (a) and the same array steered to zenith (b). Plotted for a 3x3x3 array with 0.75λ average spacing between antennas. The color scale is from -20 to 0 dB relative to the main lobe. The inset image shows the intersection of the two spheres.

radiation pattern of volumetric arrays to change dramatically during beam steering, as opposed to cases with planar or linear arrays.

Optimizing the pattern-space reduces the number of dimensions required to evaluate the sidelobe level from four $(\phi, \theta, \phi', \theta')$ to three $(\Delta u, \Delta v, \Delta w)$, thereby significantly reducing the computational requirements of the optimization algorithm. Processing time is further reduced by observing the symmetry about the origin and only optimizing the pattern–space necessary for the scan requirements of the array. Separating (9.6) into the product of the exponentials involving Δu, Δv, and Δw reduces the number of exponential calculations.

9.2.5 Similarity to Planar and Linear Arrays

The 3D pattern-space representation for a volumetric array must also apply to planar and linear arrays. For a planar array whose elements are distributed only in the *xy*-plane, the pattern-space has no structure along the Δw-axis. Therefore, the pattern-space collapses to a two dimensional structure in Δu and Δv consisting of columns of lobes. A slice of this pattern-space appears as the plane shown in Figure 9.3. The circles in Figure 9.3 indicate the planar projection of the surface of the sphere in Figure 9.4.

A similar process is followed for a linear array. If all elements in the array are distributed on the *y*-axis, the pattern-space is differentiated only along the Δv-axis. The pattern-space can be thought of as a series of stacked planes with constant gain, a cross section of which yields a pattern such as that in Figure 9.2. The intersection of the sphere in Figure 9.4 with this pattern-space results in a radiation pattern that is rotationally symmetric along the axis of the array, as is expected for linear arrays.

9.3 Array Models and Results

9.3.1 Basic Array Models

With an understanding of the optimization and analysis methods, array models and optimization results are now presented. The first model examined is the defined aperture model, shown in Figure 9.5a, which is similar to the model presented in [16]. The antenna positions are optimized with respect to their proximal grid points, which are distributed throughout the aperture at intervals of $\overline{S}$. This model was used for the linear, planar, and volumetric arrays.

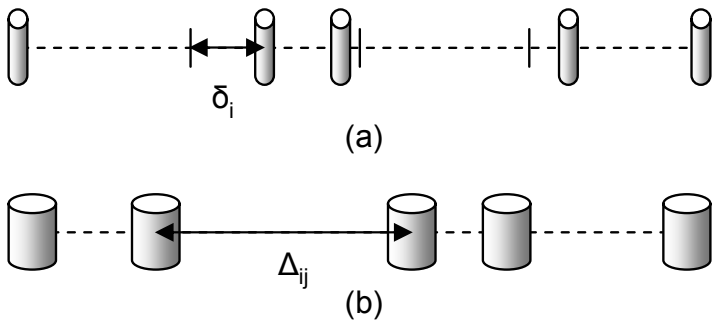

Figure 9.5: The aperiodic array models used in this study. (a) Defined aperture model. The difference between the position of an antenna and its proximal grid point is indicated by δ_i. (b) Minimum spacing model. The distance between adjacent antennas is indicated by Δ_{ij}.

The minimum spacing model, shown in Figure 9.5b, is useful when the proximity of adjacent elemental antennas is restricted. This is necessary when the elemental antennas are large, such as in arrays of electronically steered subarrays or dish antennas. Optimizing the model in Figure 9.5b determines the best aperture size for a given minimum spacing. Despite the usefulness of this model to the task of optimizing arrays of large antennas, no previous studies of this type have been conducted.

9.3.2 Optimization Results

Figure 9.6 contains plots of the optimized sidelobe levels of linear, planar, and volumetric arrays. In all cases, the pattern-spaces of the arrays are optimized for operation over all possible scan angles. Figure 9.6 shows the incremental increase in sidelobe levels with increasing aperture size decreases as the aperture becomes large. Sidelobe levels are slightly increased when a given aperture size is found with the minimum spacing model instead of the defined aperture model.

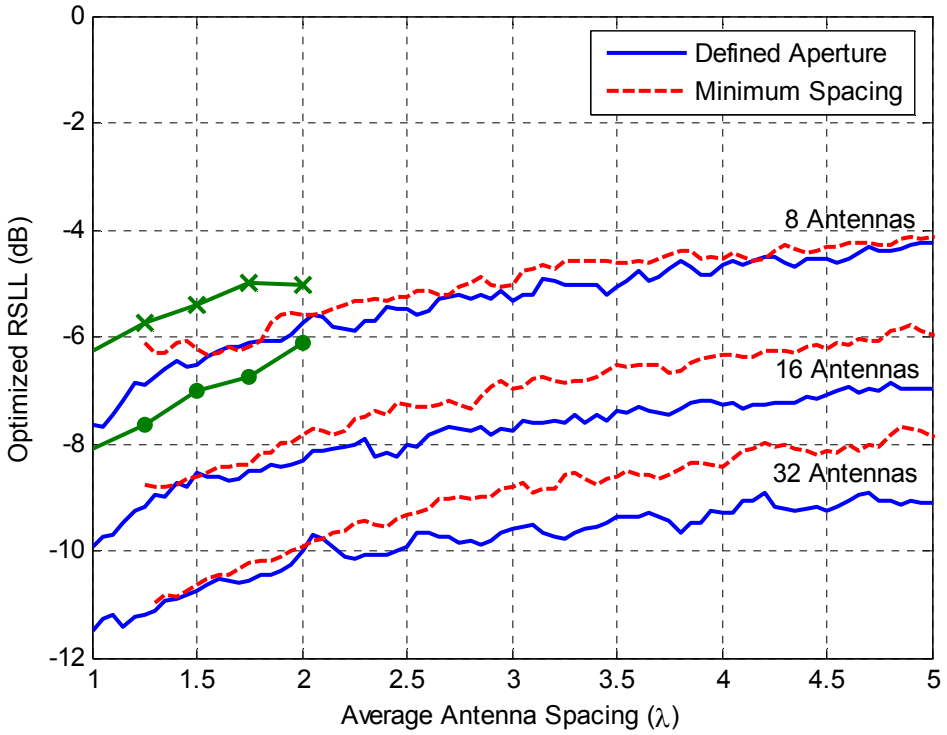

Figure 9.6: Sidelobe levels versus antenna spacing for the linear array models. Data for 5x5 planar (dot) and 3x3x3 volumetric (x) arrays are also included.

The results in Figure 9.6 for the planar and volumetric arrays were obtained using the defined aperture model. Optimized planar arrays with 25 antennas (5x5) and volumetric arrays with 27 antennas (3x3x3) exhibit similar sidelobe levels to a linear array with 8 antennas. Volumetric arrays exhibit higher sidelobes than planar arrays for a similar number of antennas. This is because the algorithm optimizes the pattern space of volumetric arrays in three dimensions and only optimizes the pattern space of planar arrays in two dimensions. This added dimension gives volumetric arrays an advantage over planar arrays: the shape of the main beam of the volumetric arrays is constant throughout scanning, whereas a planar array loses resolution when scanned beyond $\theta = 45°$.

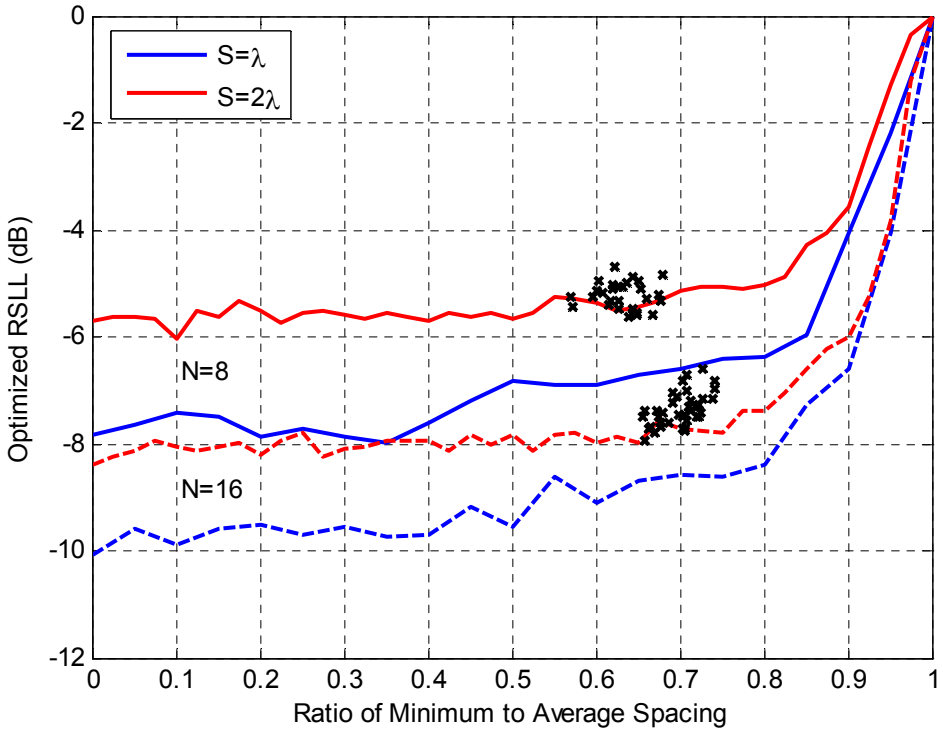

Figure 9.7: Sidelobe level versus the ratio minimum to average spacing for the defined aperture model with the minimum spacing requirement for linear arrays.

Figure 9.7 shows the relationship between the minimum antenna spacing, average antenna spacing (aperture size) and sidelobe level using a model that constrained both the distance between antennas and the aperture size. As in Figure 9.6, these arrays were optimized for operation over all possible scan angles. Plots of the RSLL versus the ratio of minimum-to-average-spacing are shown, using average antenna spacings of $\overline{S} = \lambda$ and $\overline{S} = 2\lambda$ for arrays with 8 and 16 antennas. For these spacings, a ratio of 0.75 indicates a minimum spacing of 0.75λ and 1.5λ, respectively.

Larger values of this ratio indicate that the algorithm has less freedom to move the antennas within the aperture. The sidelobe level increases significantly when the minimum distance between antennas is greater than 80% of the average distance between

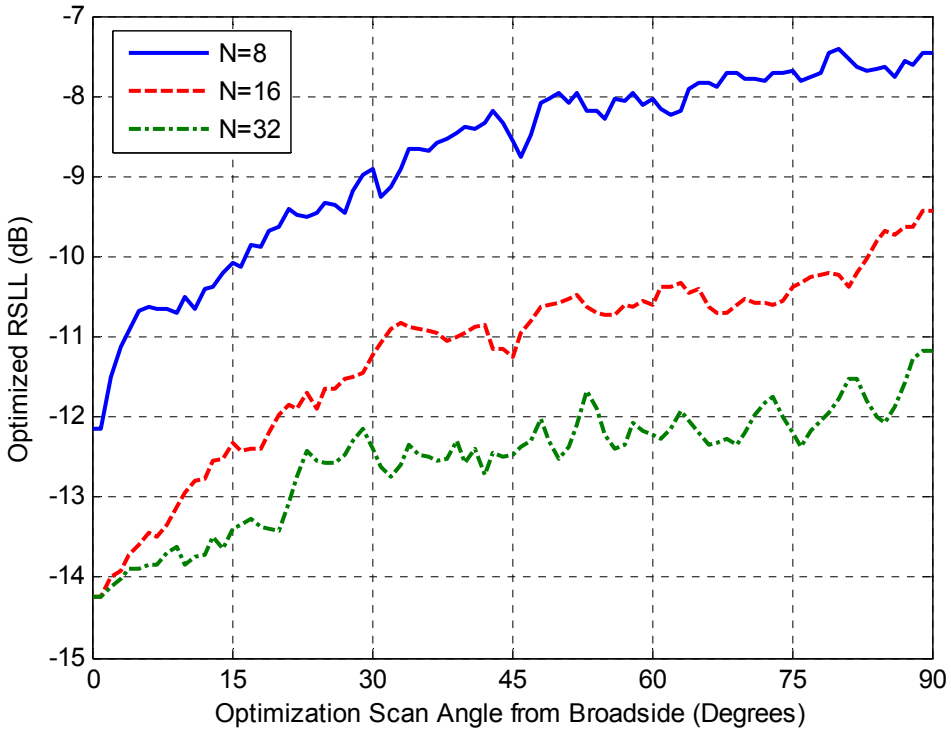

Figure 9.8: Sidelobe level versus scan angle for aperiodic arrays. The defined aperture model with an average spacing of one wavelength is used.

antennas. The "x" marks in Figure 9.7 indicate the optimum ratios obtained from analysis using the minimum spacing model and that the optimized average spacing between antennas is 25% to 60% larger than the minimum distance between the antennas.

9.3.3 Additional Linear Analysis

Figs. 9.8 and 9.9 contain additional data for aperiodic linear arrays. The data presented in Figure 9.8 shows the optimized sidelobe level versus the optimization angle from broadside, which is equivalent to the maximum scanning angle. As the scan angle increases, the sidelobe level also increases; a larger area of the pattern-space is involved in the optimization. This contradicts results from a previous study by Bray and Werner [16], who reported that sidelobe levels cannot be optimized for a scan angle near $90°$.

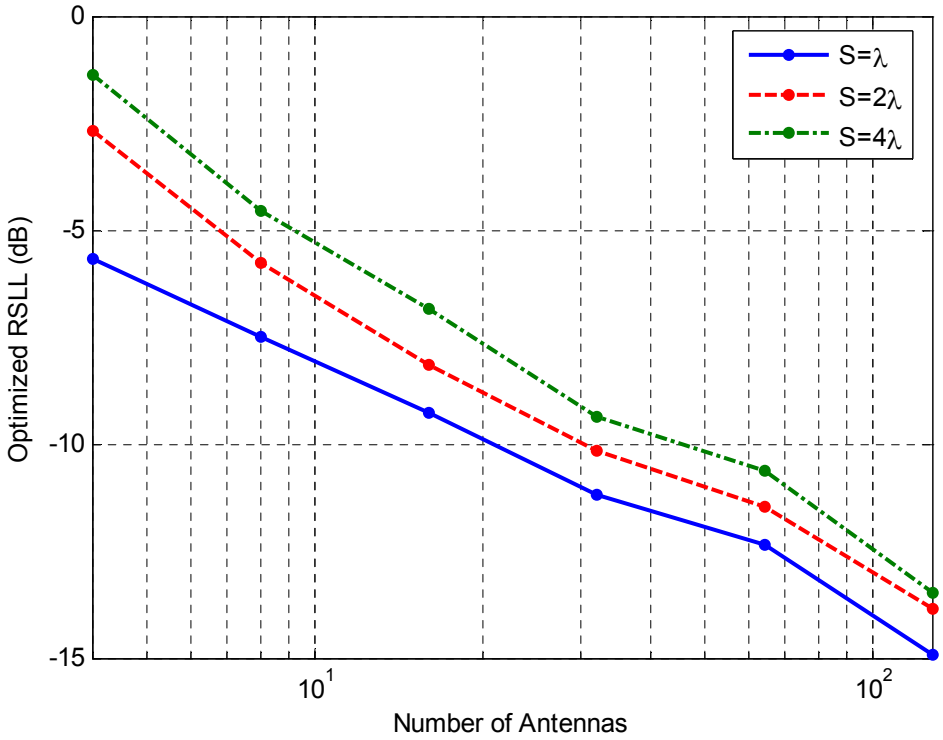

Figure 9.9: Sidelobe level versus the number of antennas. The defined aperture model is used. The arrays consist of between four and 128 antennas.

This misinterpretation was likely due to the widening of the main lobe of the array at scan angles near $90°$, as previously explained in section 9.2.1 .

The second plot, Figure 9.9, shows the optimized sidelobe level as a function of the number of antennas for several different values of $\overline{S}$. The optimized sidelobe levels decrease in an approximately log-log relationship with the total number of antennas in the array.

CHAPTER 10.
TRACKING WITH VOLUMETRIC ARRAYS

10.1 Direction Finding and Grating Lobes

The radiation pattern of a volumetric array changes dramatically as the array is steered. The patterns of linear and planar arrays also change when they are steered, but the strength of grating lobes and sidelobes, as well as their relative location to the main lobe (as evaluated in pattern-space), does not change. In a volumetric array, the radiation pattern is determined by the intersection of a spherical surface with a three dimensional pattern-space, so grating lobes, sidelobes, and other structures actually fade in and out of the pattern during steering.

Aside from nulling and interference considerations, the problem with grating lobes in an array for direction finding is that they cause ambiguities in the estimated positions for the location of the source, or target. As the target moves, the "aliased" (incorrect) position estimates move as well, making it impossible to differentiate between the target and the aliases. Placing the antennas close together or optimizing the array can remove grating lobes from the pattern. Placing the antennas very far apart can provide much better resolution for a direction finding system but limits or eliminates the ability of an optimization algorithm to suppress grating lobes in the radiation pattern.

Because the grating lobes of a volumetric array fade with steering, it is possible to differentiate between a target and an alias as long as the target traverses an arc of sufficient length. Whereas aliases will fade, appearing and disappearing, only the target will remain at a relatively stable amplitude and follow a coherent path through the two-

dimensional array steering space (azimuth and elevation). The limitations of this technique for target tracking and algorithms for application are presented in the remainder of this chapter.

10.2 Limitations and Requirements

To accurately determine the position of the target, it is necessary to determine the minimum required arc length that the target must traverse through the array steering space. It is assumed the volumetric array consists of N^3 antennas distributed in a cube with spacing $\overline{S}$ between adjacent antennas. The pattern-space first-null-beamwidth from the peak in any direction $(\hat{u},\hat{v},\hat{w})$ is estimated by

$$BW_{FN} \approx 1/\left(N\overline{S}\right). \tag{10.1}$$

Stutzman and Thiele [11] also estimate the half-power beamwidth as

$$BW_{3dB} \approx BW_{FN} \cdot \sqrt{3}/4. \tag{10.2}$$

Grating lobes are distributed on a grid every $1/\overline{S}$ units in pattern-space.

A grating lobe, which causes an alias, becomes visible when intersected by the pattern-space. The lobe becomes invisible again when the pattern-space is rotated such that it no longer intersects the lobe. The angle of rotation, 2α, required for the grating lobe to completely pass through the pattern-space, indicates the ease with which the alias is differentiated from the target. Smaller values of α mean the target must traverse a smaller angle through the sky before the alias is differentiated. The converse is also true,

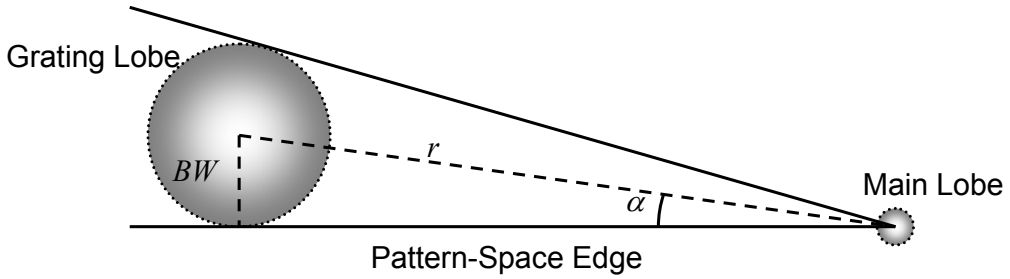

Figure 10.1: Geometry of a normal intersection of a grating lobe with the pattern-space.

so grating lobes with a larger value of α require the target to traverse a larger path through the sky before the alias is differentiated.

For the first case, consider the geometry of Figure 10.1. This is a special case in which the pattern-space boundary is normal to the direction of motion at the point of intersection with the grating lobe. The angle that must be traversed by the target is found by rotating the pattern-space. As seen in Figure 10.1, if a grating lobe is located a distance r from the main lobe, then the angle α is given by

$$\alpha = \arcsin\left(\frac{BW}{r}\right). \tag{10.3}$$

In the case of the grating lobe closest to the main lobe and using the first null beamwidth, $\alpha = \arcsin\left(1/N\right)$.

In practice, the grating lobe intersects the pattern-space at a skewed incidence angle. The scan angle required to differentiate the grating lobe is a problem of spherical geometry and is left as further work. However, it is noteworthy that the worst case is exhibited as a tangential intersection with some cross section of the pattern-space, as shown in Figure 10.2. The required half-arc for alias differentiation is given by

$$\alpha = \arctan\left[\frac{(r+BW)\cdot\sin(2\Phi)}{r+(r+BW)\cdot\cos(2\Phi)}\right], \tag{10.4}$$

where

$$\Phi = \arccos\left(\frac{r-BW}{r+BW}\right). \tag{10.5}$$

Grating lobes closer to the main lobe in pattern-space require the target to traverse a greater angle to differentiate the alias. This observation can be exploited in the optimization algorithm. For example, the algorithm might only optimize the pattern-space to reduce lobes that are close to the main lobe, improving the quality of the optimization.

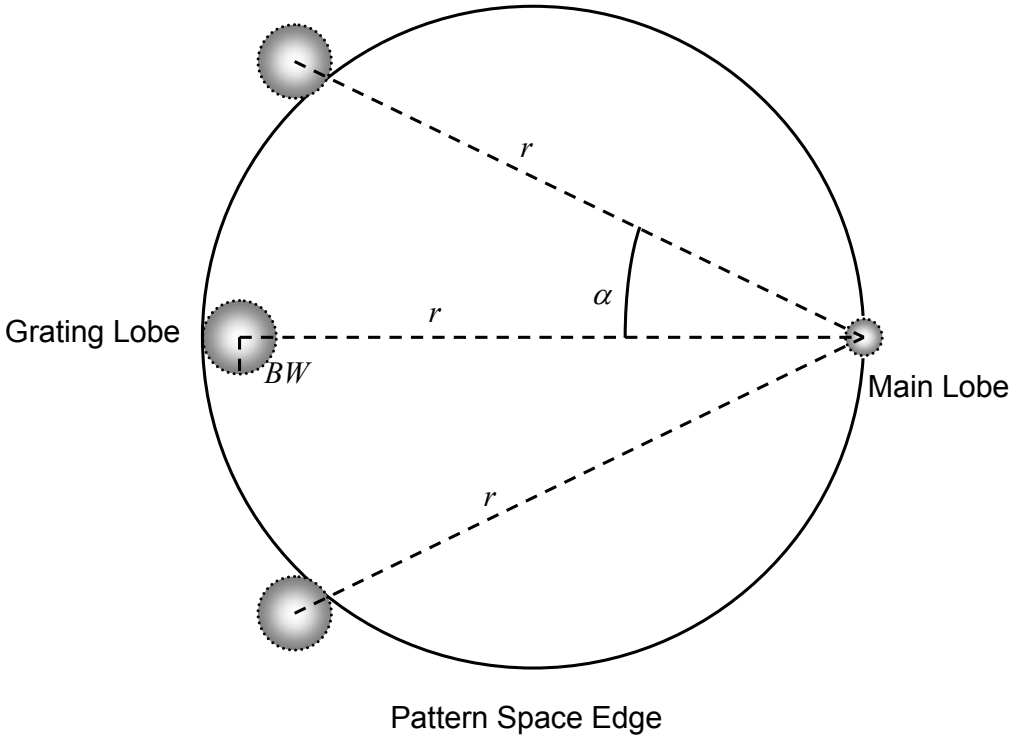

Figure 10.2: Geometry of a tangential intersection of a grating lobe with the pattern-space.

10.3 Tracking Algorithm

A simple algorithm has been developed to demonstrate this technique for successfully tracking a target among many aliases. This algorithm has three fundamental steps: peak identification, temporal peak tracking, and alias differentiation.

10.3.1 Peak Identification

The first step in the algorithm is peak detection. The algorithm processes the array stimulus vector to determine the direction from which a signal, or signals, is likely to have originated. Several methods can be used to perform this task, such as simple beamforming [12], MUSIC [42], and ESPRIT [43]. The first of these, simple beamforming, is sufficient for demonstrating the tracking algorithm.

Peak detection via beamforming requires electronically steering the array to many directions and identifying which directions correspond to the maximum beamformer output. For a given phasor stimulus on the array, $\mathbf{x}$, the beamformer output $\mathbf{y}_{\phi,\theta}$ looking in the direction (ϕ,θ) is found by

$$\mathbf{y}_{\phi,\theta} = \mathbf{a}_{\phi,\theta}^{H}\mathbf{x}. \tag{10.6}$$

The operator H represents the Hermitian, and the vector $\mathbf{a}_{\phi,\theta}$ is the steering vector, which is determined by the ideal array stimulus when a signal is incident from the direction (ϕ,θ). The number of coordinate pairs (ϕ,θ) limits the resolution of this method. A typical plot of this type is shown in Figure 10.3 for a volumetric array with nine antennas spanning an aperture of 5λ in $\hat{x}$, $\hat{y}$, and $\hat{z}$. The layout of this array is shown in Figure 10.4. The *xy*-coordinates of the antennas are positioned on a 2.5λ grid,

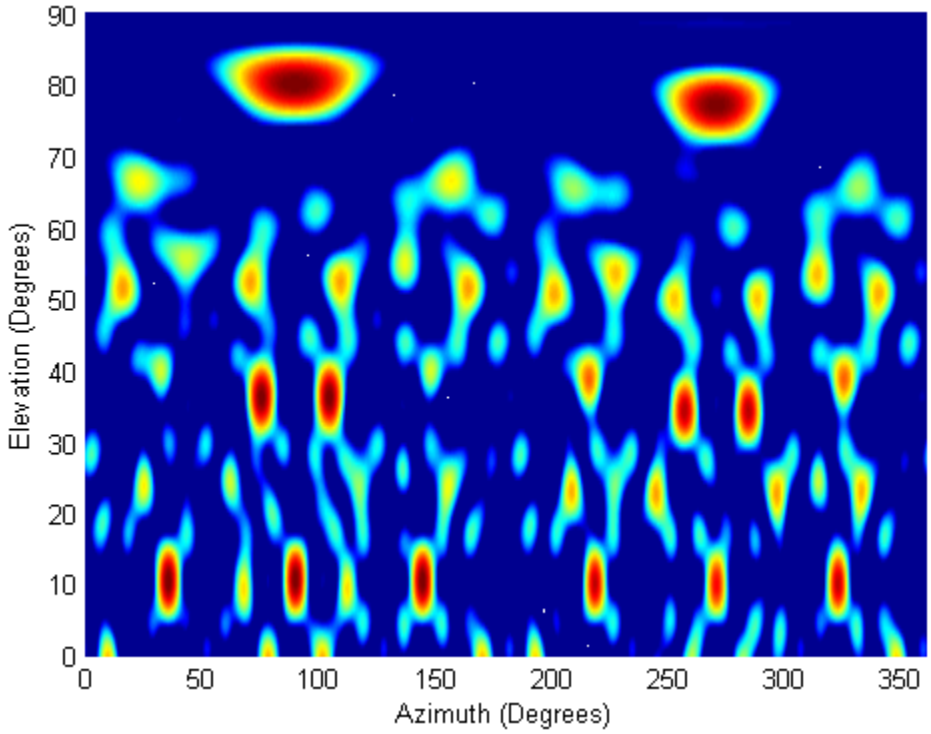

Figure 10.3: Beamformer output as a function of direction. The color scale varies from -10 dB to 0 dB relative to the main lobe.

and the *z*-coordinates are selected for symmetry. The target in Figure 10.3 is located at $90°$ azimuth and $10°$ elevation, but is indistinguishable from its aliases.

This algorithm determines the peak locations by finding the maximum output of the beamformer where the gradient, $\nabla \mathbf{y}$, is close to zero. Mathematically, this is given by

$$\mathbf{p} = \max\left[\mathbf{y} \,|\, \nabla \mathbf{y} \approx 0\right], \tag{10.7}$$

where

$$\nabla \mathbf{y} = \frac{\partial \mathbf{y}}{\partial \phi}\hat{\phi} + \frac{\partial \mathbf{y}}{\partial \theta}\hat{\theta}. \tag{10.8}$$

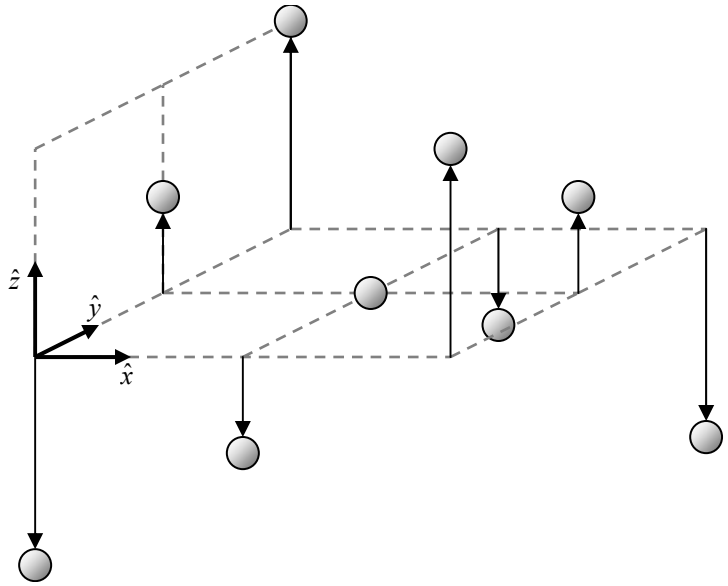

Figure 10.4: Volumetric array used to demonstrate the tracking algorithm. Shaded circles indicate the 9 antenna positions. Grid spacing is 2.5λ.

Areas within one beamwidth of an identified peak are omitted as the algorithm iteratively searches for further peaks. For a single source, the number of iterations should be larger than the number of grating lobes and significant sidelobes expected in the pattern. This process generates a list of peak directions such that $\mathbf{p}_i = (\phi_i, \theta_i)$.

10.3.2 Peak Tracking

The list of peaks is generated for a data set at a particular time t. For many data sets, many such lists are generated, creating a list $\mathbf{p}(t)_i$. These peaks are not inherently associated. It is possible for the target to appear in the slot $i = j$ at one time and $i = k$ at another time, where $j \neq k$. Points are associated by calculating the angle between the vectors $\mathbf{p}(t)_j$ and $\mathbf{p}(t + \Delta t)_k$ for all (j,k). The peak $\mathbf{p}(t)_j$ is assigned an association with the peak $\mathbf{p}(t + \Delta t)_k$ such that the angular difference Φ, given by

$$\cos\Phi = \frac{\mathbf{p}_1 \bullet \mathbf{p}_2}{\|\mathbf{p}_1\|\|\mathbf{p}_2\|}, \tag{10.9}$$

or more explicitly,

$$\begin{aligned}\cos\Phi = &\cos\phi_1 \sin\theta_1 \cos\phi_2 \sin\theta_2 \\ &+ \sin\phi_1 \sin\theta_1 \sin\phi_2 \sin\theta_2 \\ &+ \cos\theta_1 \cos\theta_2 ,\end{aligned} \tag{10.10}$$

is minimized. This association is made only if the angle Φ is less than a threshold angle, which is chosen based on the estimated angular speed of the target.

10.3.3 Alias Differentiation

The final task is to filter the data to identify the true path of the target among the aliases. Many possibilities exist for implementing this filter. One such implementation is to calculate the arc traversed by a coherent set of associated data and to suppress any data that does not traverse an arc of sufficient length. The arc length (s) is found from the line integral of the path, $s = \int_\gamma |d\ell|$, which for a tracked peak becomes

$$s = \int_{t_1}^{t_2} \left\| \frac{dP(t)}{dt} \right\| dt \, . \tag{10.11}$$

The function $P(t)$ describes the location of the peak as a function of time, and the start and end times of the track are given by t_1 and t_2. Alternatively, the arc length can be defined as the angle between the start and end points,

$$s = \Phi_{12} , \tag{10.12}$$

using the definition of Φ from Equation (10.9). Finally, the metric of the path can be defined as the lifetime of the path,

$$s = t_2 - t_1 . \tag{10.13}$$

For a single target, the arc length of the target will be the longest evaluated, and the rest of the track lengths are noticeably shorter.

The properties of aliased tracks were evaluated using the volumetric array shown in Figure 10.4. A simulated target traversed an arc of constant azimuth from $El = 0°$ to $El = 90°$ at a constant speed of $1°$ per sample interval; 180 azimuth coordinates were evaluated, ranging over a $180°$ arc in increments of $1°$. A typical radiation pattern for this array, such as that in Figure 10.3, has 12 strong lobes and about 30 weaker lobes, so the tracking algorithm was allowed to track up to 50 peaks at a time. The algorithm requires many tracks when the received signal is in the presence of strong noise and many aliases have a stronger power than the target.

This array is considered to have 3 antennas per dimension with a spacing of 2.5λ between antennas. The estimated UVW spacing of grating lobes is $1/\overline{S} = 0.4$. The estimated first-null beamwidth is given by (10.1) as 0.1333 and the 3 dB beam width is given by (10.2) as 0.0577. The estimated angle of differentiation for a normal alias is calculated by (10.3). For the closest grating lobe to the main lobe $2\alpha = 38°$ for BW_{FN} and $2\alpha = 16°$ for BW_{3dB}. The estimated angle of differentiation for a tangential alias is calculated with Equation (10.4) and is $147°$ for BW_{FN} and $90°$ for BW_{3dB}.

The likelihood an alias exceeds a given length is shown in Figure 10.5, using the previously described target tracks from $El = 0°$ to $El = 90°$. The three methods of evaluating a track from Equations (10.11) through (10.13) are applied to this data. The analysis used 90 time samples, each representing a change in the target position of $1°$, so the metric of total time is easily compared to the other two.

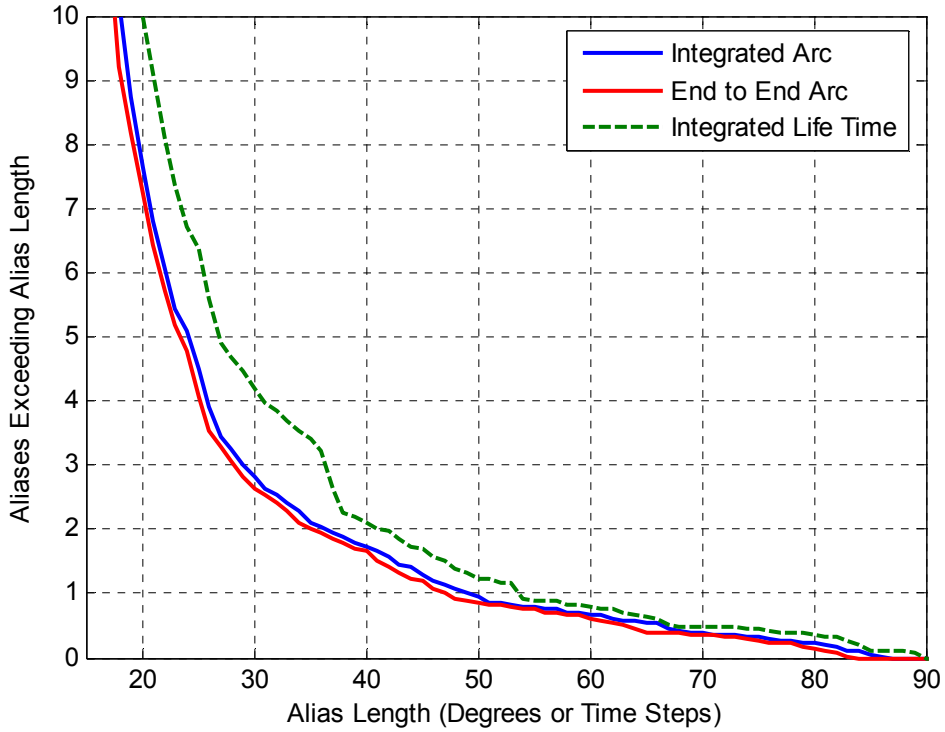

Figure 10.5: Expected number of aliases exceeding a given length for a $90°$ target track.

The *x*-axis of Figure 10.5 represents the track length of the alias, in degrees or sample points. The *y*-axis represents the number of aliases that exceeded the indicated track length, normalized by the number of azimuth positions of the target. For example, an average of two aliases per-track (target motion from $El = 0°$ to $El = 90°$) exceed a track length of $35°$. Less than half of the tracks exhibit even one alias longer than $70°$.

10.3.4 Final Thoughts

The ODIN array described in Part 4 of this dissertation implements this tracking algorithm to determine the observed path of the NASA satellite EO-1 in the presence of many aliases. This process is discussed further, with presentation of measured data, in Part 5.

This method can also be employed if multiple targets are present in the data. However, the implementation will become more complex, as the aliases of one target might become intermingled with the aliases of another target. Better tracking filters, such as Kalman filters [44], would be employed in such an implementation. This is a possible subject for further research.

CHAPTER 11.
REDUCED FOURIER PROJECTION BEAMFORMING

11.1 Introduction

In addition to the optimization of the topology of a phased array, it is necessary to consider optimal methods for beamforming with the array. Beamforming refers to the process of combining the data from each antenna to create a data set representing the output of the entire array. The radiation (or reception) pattern of the array is steered to a desired direction and incorporates independently steered nulls by altering the relative weights and phases of each antenna during beamforming.

Beamforming with the Fast Fourier Transform (FFT) [45] is a well established means to reduce the complexity of forming multiple beams (multibeaming) in a phased array system [46]. The orthogonal projection method is a technique used for placing pattern nulls [47-50]. Recently, Ellingson and Cazemier [50] demonstrated that FFT beamforming can be combined with the orthogonal projection technique to allow placement of arbitrary nulls with only a small increase in the computational cost as compared to the FFT alone.

Many applications require a spatially extended phased array to increase angular resolution. However, fully populating the array aperture with antennas on a $\lambda/2$ grid can be both unnecessary and costly. In such cases, thinning techniques are used to optimize the positions of the antennas to satisfy requirements such as sidelobe minimization. Although it was suggested that the beamforming methods of [50] are applicable to such arrays, the presentation in [50] focused only on arrays with $\lambda/2$ spacing. This study has

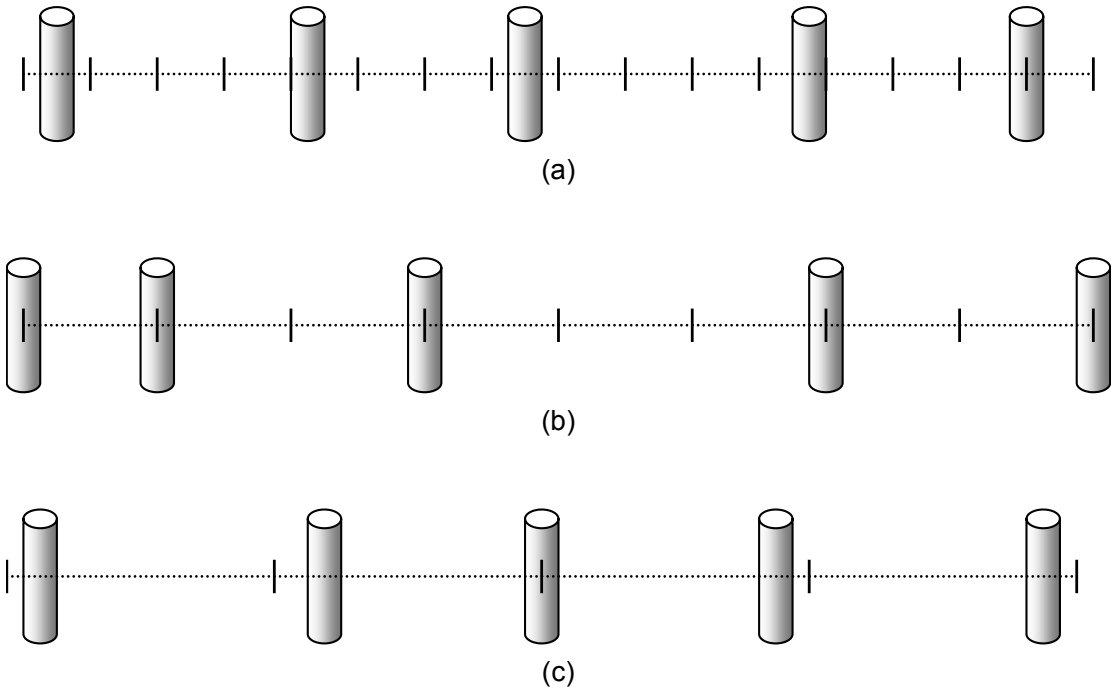

Figure 11.1: Diagrams of the three layout strategies that were investigated. (a) The antennas positions are aperiodic and the sample grid is dense, but most of the FFT inputs are zero. (b) The antenna positions are constrained to lie on a wider sample grid. (c) Few sample grid points are used and the antennas are close to the grid points.

aimed to determine the most efficient methods of applying such techniques to thinned linear arrays.

Three strategies have been explored for applying FFT beamforming with projection nulling to a thinned linear array; these will be compared for both beamforming accuracy and computational cost. The first strategy uses an arbitrarily dense sample grid with many of the input points set equal to zero, as was suggested by Ellingson and Cazemier [50]; this is shown in Figure 11.1a. The second uses thinned arrays in which the antenna positions are constrained to a wider sample grid, as shown in Figure 11.1b. The final approach uses beam-space beamforming with a reduced set of FFT beams.

In this analysis, a metric for evaluating computational cost is defined as the number of operations $\left(n_{ops}\right)$, as per Ellingson and Cazemier [50]. Each multiplication or addition of two real numbers represents a single operation; complex multiplication and addition therefore represent six and two operations respectively. It will be shown that the computational cost of beamforming with a thinned array most closely correlates with the size of the aperture and spacing of the sample grid, with a lesser dependence on the number of antennas. Furthermore, an improved algorithm will be demonstrated that decreases the computational cost when only a subset of FFT beams is desired. In addition to the lower computational cost, this algorithm can create a set of independently steered and orthogonal beams, which is particularly appropriate to multibeaming communications arrays.

A new thinned array model has been developed, which leads to a design that further reduces the computational cost of the new algorithm, as shown in Figure 11.1c. The reduction is achieved by widening the sample grid beyond $\lambda/2$. Potentially, the sample grid spacing could be increased up to the average antenna spacing. By constraining the characteristics of the antenna positions, this approach can effectively suppress grating lobes while retaining the computational efficiency of the FFT. Some results from optimizations with a genetic algorithm will be presented using this model.

11.2 BIP Algorithm

Because the methods described by Ellingson and Cazemier will be referenced extensively, their fundamental derivation is restated. Although various windowing

techniques were applied in [50], only the direct projection nulling algorithm, known as beamforming with interference projection (BIP), will be considered here.

If the vector containing the outputs of N antennas in an array at a time t is given by $\mathbf{x}(t)$, and the matrix $\mathbf{A}$ contains the concatenated steering vectors, then a vector $\mathbf{Y}(t)$ containing the beamformer outputs at any time t is given by the expression for the conventional beamformer (CBF),

$$\mathbf{Y}(t) = \mathbf{A}^H \mathbf{x}(t) , \tag{11.1}$$

where H represents the Hermitian operator. Interferers can be nulled by pre-multiplying $\mathbf{x}(t)$ by an orthogonal projection operator, given by

$$\mathbf{P}_\mathbf{V}^\perp = \mathbf{I} - \mathbf{P}_\mathbf{V} = \mathbf{I} - \mathbf{V}\left(\mathbf{V}^H \mathbf{V}\right)^{-1} \mathbf{V}^H , \tag{11.2}$$

where $\mathbf{V}$ contains the concatenated steering vectors of the interferers. The output vector is then given by

$$\mathbf{Y}(t) = \mathbf{A}^H \mathbf{P}_\mathbf{V}^\perp \mathbf{x}(t) . \tag{11.3}$$

If a full set of beams is desired so that the number of beams equals the number of antennas, the computational cost of (11.3) is $O(N^2)$. Efficient multibeaming is accomplished by setting $\mathbf{A}^H$ equal to $\mathbf{F}$, the matrix form of the Discrete Fourier Transform (DFT). Then the Fast Fourier Transform, or FFT, can be employed. Because $\mathbf{P}_\mathbf{V}$ is Hermitian, it can be rewritten in terms of its eigendecomposition $\mathbf{U}\Lambda\mathbf{U}^H$. Since $\mathbf{P}_\mathbf{V}$ is also rank k, the eigendecomposition can be rewritten as

$$\mathbf{P}_{\mathbf{V}} = \sum_{i=1}^{k} \mathbf{u}_i \mathbf{u}_i^H \ , \tag{11.4}$$

where $\mathbf{u}_1 \ldots \mathbf{u}_k$ are the columns of $\mathbf{U}$ associated with the nonzero eigenvalues. Applying (11.4) to (11.3) and using the FFT for $\mathbf{A}^H$ gives the functional form of the BIP algorithm,

$$\mathbf{Y}(t) = \mathbf{F}\mathbf{x}(t) - \sum_{i=1}^{k} \left[\mathbf{u}_i^H \mathbf{x}(t) \right] \mathbf{F}\mathbf{u}_i \ . \tag{11.5}$$

When different beams require different nulls resulting in Q discrete sets of null vectors, $\mathbf{V}_1 \ldots \mathbf{V}_Q$, then (11.5) is modified. The modification to (11.5) is applied by computing Q separate eigen-decompositions and summations, and applying chosen null sets to the appropriate beams.

Ellingson and Cazemier demonstrated the ability of the BIP algorithm to efficiently form arbitrary nulls in the beam patterns of a uniformly spaced planar array. Although they demonstrated BIP only with uniformly spaced arrays, they stated the value of having a method to apply BIP to non-uniformly spaced arrays. This problem was explored, and in the following sections, three such methods are presented.

11.3 Approaches to Beamforming

11.3.1 Dense Grid Approximation

As discussed above, the BIP algorithm is best applied to phased arrays of antennas uniformly spaced on a grid. If the array is thinned to reduce the number of antennas in an aperture and if the resulting distribution is aperiodic, then the antenna positions will not correspond to the sample grid. The first method of applying BIP to a

non-uniformly spaced array is to increase the sample grid to an arbitrary density so each antenna is close to a grid point; grid points not proximate to an antenna are set to zero [50]. Because the antenna positions do not conform to any underlying grid, there will be an unavoidable grid approximation error; this will manifest itself as a phase error characterized by

$$\phi_n = 2\pi\delta_n \sin\theta, \tag{11.6}$$

where n is the element index, θ is the scan angle from broadside, δ_n represents a uniformly distributed random variable between $-\frac{1}{2}S_g$ and $+\frac{1}{2}S_g$, and S_g is the grid spacing in units of wavelengths.

Phase errors in beamforming have been examined in great detail [51-52] and alter the resulting beam in several ways. They can produce reductions in the gain of the main beam, shift the position of the main beam, and degrade sidelobe performance. The positions of the nulls given by the steering vector $\mathbf{V}$ will not be affected by the phase errors because the errors are systematic and, can therefore be accounted for in the construction of $\mathbf{V}$.

If the errors are small and uniformly distributed, then the expected decrease in the power of the main lobe can be approximated from Hansen [12] by

$$\begin{aligned} G/G_0 &= \left| mean\left[\exp(j\phi)\right]\right|^2 \\ &\approx \exp\left(-\sigma^2\right) \approx 1/\left(1+\sigma^2\right), \end{aligned} \tag{11.7}$$

where $\sigma = \phi_{\max}/\sqrt{3}$ and G_0 is the array gain with no phase errors. Although Hansen gives the expected sidelobe performance as

$$SLL = SLL_0 \sqrt{1 + \sigma^2 / \left(G_0 SLL_0^2 \right)}, \tag{11.8}$$

where SLL_0 is the original sidelobe level, the observed degradation in the worst performing sidelobe is higher. A worst case approximation of the sidelobe performance, given by

$$SLL = SLL_0 + \phi_{\max} / 2\pi \,, \tag{11.9}$$

where $\phi_{\max} = \pi S_g \sin\theta$, is in better agreement with observations. The sidelobe levels in dB are found from the values in (11.8) and (11.9) by $SLL_{dB} = 20 \cdot \log_{10}\left(SLL\right)$.

These equations imply that there exists a maximum acceptable grid spacing for this method, which will vary based on the requirements of the application. Generally, the grid spacing must be much less than $\lambda/2$. For example, a grid spacing of $\lambda/20$ represents a main lobe degradation of less than 0.05 dB, but worst-case sidelobes that were originally -10 dB are increased by nearly 1 dB, and sidelobes that were originally -20 dB are increased by up to 2 dB.

Many methods have been described to mitigate the effects of phase errors in beamforming [51-52], but most of these are suited to quantization errors in periodic arrays. For example, the phase added method [52] suggests adding a random delay into each channel to alleviate the problems of periodic phase error. However, since the grid quantization errors are themselves random, the phase added method is inappropriate. In addition, the small grid spacing implies a high computational cost. Therefore, a method requiring fewer sample points is desirable.

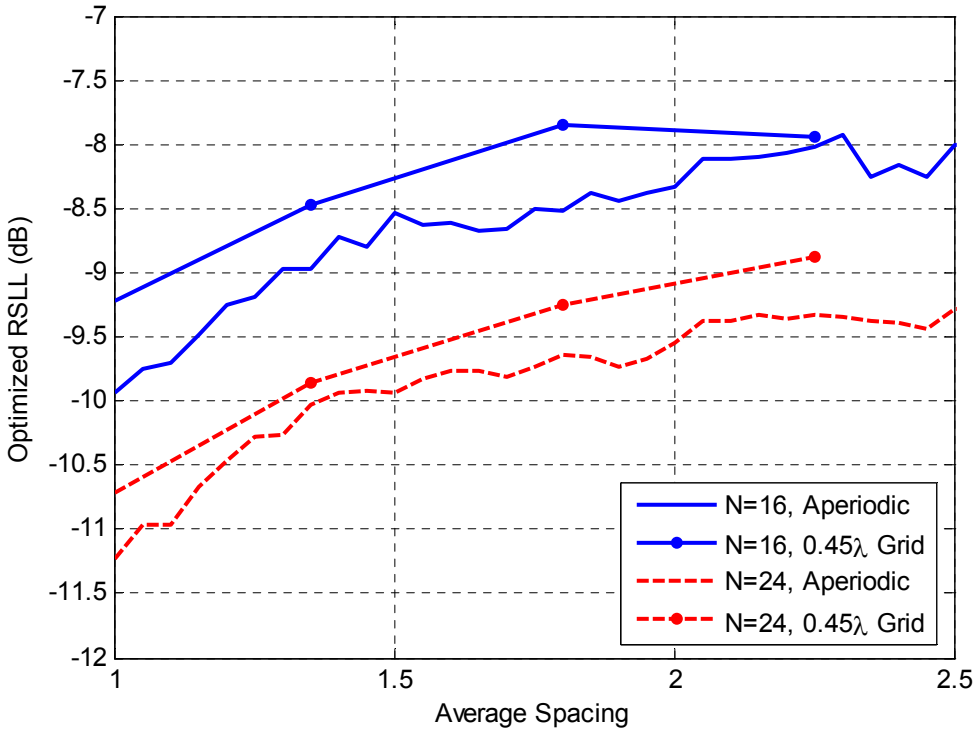

Figure 11.2: Optimized sidelobe levels of thinned linear arrays as a function of the average spacing $\overline{S}$ between antennas.

11.3.2 Quantization Grid Arrays

The potentially high computational cost of the dense grid approximation method is avoided if the antenna positions conform to an underlying grid. The GA used in Chapter 9 optimized the sidelobes for arrays in which the antennas are constrained to lie on a quantization grid of 0.45λ. Optimization results for arrays consisting of 16 and 24 antennas are compared to similar results obtained using an unconstrained aperiodic optimization. Both array types were optimized for end-fire radiation. The optimized sidelobe levels are presented in Figure 11.2 as a function of the average spacing between adjacent elements, $\overline{S}$.

The aperiodic arrays have slightly lower sidelobes than the arrays that use the 0.45λ quantization grid. However, the maximum difference in sidelobe levels is 1 dB and, in some cases, is less than a 0.1 dB. For large arrays, quantization grids that are almost as large as $\lambda/2$ result in only a negligible increase in sidelobe levels. If the quantization grid corresponds to the sample grid, then there will be no beamforming errors and the number of points in the FFT can be significantly reduced. However, a different approach must be used for sample grid spacings larger than $\lambda/2$.

11.3.3 Selective Fourier Beam Combining

An alternative method of FFT beamforming with aperiodic arrays requires an additional step in the beamforming process. This step consists of selective beam combining of the Fourier beams and is possible because the columns of the DFT form an orthogonal basis [53]. For the system defined in Equation (11.1), it is possible to perform beamforming in Fourier beam-space rather than in element-space. A single Fourier steering vector $\mathbf{b}$ is defined as the Fourier transform of the steering vector $\mathbf{a}$,

$$\mathbf{b} = \mathbf{F}\mathbf{a}. \tag{11.10}$$

Applying the Hermitian of the steering vector to the Fourier transform of the inputs gives

$$\mathbf{y}(t) = \mathbf{a}^H \mathbf{F}^H \mathbf{F}\mathbf{x}(t), \tag{11.11}$$

which simplifies to (11.1) because the DFT is unitary. If a masking operator $\mathbf{m}$ is defined as a diagonal matrix of ones and zeros, and represents the selective combining process, (11.10) can be rewritten as

$$\mathbf{b} = \mathbf{mFa}\,, \tag{11.12}$$

which in turn alters (11.11) to become

$$\mathbf{y}(t) = \mathbf{a}^H \mathbf{F}^H \mathbf{mFx}(t)\,. \tag{11.13}$$

The middle three terms are rewritten as a filtering operator $\mathbf{G}$ so that

$$\mathbf{G} = \mathbf{F}^H \mathbf{mF}\,. \tag{11.14}$$

This can be applied to a vector as either a matrix multiplication or a subscript operator

$$\mathbf{x}_G(t) = \mathbf{Gx}(t)\,. \tag{11.15}$$

When $\mathbf{m}$ is properly selected, this operator will take the Fourier transform of a signal, select the most significant bins, and recombine those bins while ignoring the rest. This process is analogous to an ideal bandpass filter, in which the pass-bands are chosen to allow all of the significant information to proceed unattenuated. If the subject signal is monotonic, such as a plane wave incident on an aperture, the number of significant bins will be small and independent of N.

Interference nulling can be accomplished as in BIP by the application of a projection operator. It is necessary to null the element-space interference steering vectors after the application of $\mathbf{G}$. It is also necessary to extend the mask to cover the bins stimulated by the interference vectors. The projection operator becomes

$$\mathbf{P}_\mathbf{V} = \mathbf{V}_G \left(\mathbf{V}_G^H \mathbf{V}_G \right)^{-1} \mathbf{V}_G^H\,, \tag{11.16}$$

which simplifies to

$$\mathbf{P}_{\mathbf{V}} = \mathbf{V}\left(\mathbf{V}^H \mathbf{V}_G\right)^{-1} \mathbf{V}^H . \tag{11.17}$$

This projection operator is applied to the steering vector to obtain

$$\mathbf{b} = \mathbf{mF}\left[\left(\mathbf{I} - \mathbf{P}_{\mathbf{V}}\right)\mathbf{a}\right]. \tag{11.18}$$

The output of a single beamformer becomes

$$\mathbf{y}(t) = \left[\mathbf{F}\left(\mathbf{I} - \mathbf{P}_{\mathbf{V}}\right)\mathbf{a}\right]^H \mathbf{mFx}(t), \tag{11.19}$$

which simplifies to the form of (11.3) as

$$\mathbf{y}(t) = \mathbf{a}^H \left(\mathbf{I} - \mathbf{P}_{\mathbf{V}}\right) \cdot \mathbf{x}_G(t). \tag{11.20}$$

The algorithm is implemented as

$$\mathbf{y}(t) = \sum_i \left[\mathbf{F}\left(\mathbf{I} - \mathbf{P}_{\mathbf{V}}\right)\mathbf{a}\right]_i^H \left[\mathbf{Fx}(t)\right]_i , \tag{11.21}$$

where the values of the summation are defined by the nonzero indices of the mask. The algorithm given by (11.21) is called the Reduced Fourier-space Projection method, or RFP.

The BIP interference nulling algorithm from Section 11.2 can be incorporated into RFP by substituting $\mathbf{Fx}(t)$ with results from (11.5). This would reduce the number of computations required to form each beam by pre-forming nulls that are common to all of the beams. The relative computational costs of the algorithms and the situations where pre-forming nulls is appropriate are discussed in Section 11.4 .

Additionally, the RFP method has two significant advantages over BIP: independent beam steering and independent nulling. Equation (11.21) is the method for

forming a single beam. Multiple beams are formed by repeating the process using different pre-calculated steering vectors. These beams can also be made orthogonal, a task BIP cannot efficiently accomplish.

11.3.4 Further Cost Reduction through Array Optimization

To this point, the derivation of the RFP method has made no assumptions about the structure of the phased array. The beamforming algorithm and computational cost are valid whether the RFP method is applied to an aperiodic array or an array with quantized antenna positions. Additionally, no assumptions were made about the sample grid. Since the algorithm selects the most significant bins of the FFT for combining, the sample grid spacing can be increased until the number of sample points is equal to the number of antennas; however, increasing the grid spacing will increase the number of significant bins and the computational cost of using the algorithm.

It is possible to structure the phased array so the number of significant bins remains small compared to N as the grid spacing is widened past $\lambda/2$. The approach involves extending the sample grid and allowing the element placements to deviate by a small amount from the grid. If the deviation is sufficiently small, the vector of the element outputs expressed as phasors, Φ_n, can be described by

$$\begin{aligned}\Phi_n &= \exp\left[j2\pi \sin(\theta)\cdot\left(n\cdot\overline{S}+\delta_n\right)\right] \\ &\approx \left(1+j\delta_n\right)\cdot\exp\left[j2\pi\overline{S}\sin(\theta)\cdot n\right],\end{aligned} \tag{11.22}$$

where n is the element index, θ is the scan angle from broadside, $\overline{S}$ is the average spacing between adjacent antennas, and δ_n is the deviation of the position of the n_{th}

element from its proximate grid position. Equation (11.22) is rewritten as $\Phi_n = (1 + j\delta_n) \cdot \Phi'_n$, where $\Phi'_n = \exp\left[j2\pi \bar{S} \sin(\theta) \cdot n \right]$.

The concatenated values of δ and Φ' can be considered as signals. The values of Φ' are sinusoidal with a spatial frequency determined by the scan angle θ. The values of δ are pseudo-random and determined by the optimization algorithm. When considering these values as signals, it is clear that δ phase-modulates Φ' to produce Φ. The simplification of (11.22) is achieved by assuming that δ_n is small compared to a wavelength and treating it as phase noise [54].

In the derivation of RFP, it was stated that the filtering operator $\mathbf{G}$ is constructed based on the significant indices of $\mathbf{F}\mathbf{x}(t)$ and that it is important to keep the number of these significant indices small. It is possible to analyze $\mathbf{F}\Phi$ because Φ is the phasor expression for $\mathbf{x}(t)$, and the Fourier transform of (11.22) becomes $\left[\mathbf{F}(1 + j\delta)\right] * (\mathbf{F}\Phi')$. The signal Φ' has one frequency component and its transform has few significant indices, but the convolved spectrum of $\mathbf{F}(j\delta)$ with $\mathbf{F}\Phi'$ can have many significant indices. Their significance compared to the significant indices of $\mathbf{F}\Phi'$ depends on the amplitude and spectral profile of δ [55]. Constraining the amplitude or the spectral profile of δ during the array optimization will limit the number of significant indices of $\mathbf{F}\Phi$, and thus of $\mathbf{F}\mathbf{x}(t)$.

The tradeoff involved in selecting the deviation profile balances grating lobe suppression with spatial FFT bandwidth. A GA was constructed to limit both the amplitude and the bandwidth of the deviation signal. The genome of the spacing deviation ($\mathbf{s}$) was modified so the genes contained the Fourier transform of the spacing deviation rather than the deviation itself. The spacing gene was also allowed to contain

complex rather than real valued data, and the vector of spacing deviations was found by calculating the real part of the inverse Fourier transform

$$\delta = real\left[IFFT\left(\mathbf{s}\right)\right]. \tag{11.23}$$

Ideal band limiting was achieved by applying a mask of ones and zeros to the spacing gene, and amplitude limiting was achieved by normalizing the spacing gene by the maximum value of the spacing offsets. The spacing gene was optimized using a population fitness defined by the maximum sidelobe level exhibited when the array is steered to a scan angle of $90°$ from broadside.

The GA was used to optimize the spatial configuration of a linear array with $\overline{S} = \lambda$. The use of a $90°$ scan angle maximizes the phase difference between adjacent antennas and represents the worst-case behavior of the optimization process. Better results are obtained by limiting the scan range of the array and optimizing the array at the maximum scan angle from broadside. This improvement is because a smaller area of the pattern-space is optimized when the maximum scan angle is reduced and because the spatial phase noise in Equation (11.22) depends on the scan angle.

The GA analysis was performed for arrays consisting of 16 and 24 antennas, and Figs. 11.3 and 11.4 contain plots showing the trade-off between the spatial FFT bandwidth and grating lobe suppression. The spatial FFT bandwidth is related to the number of nonzero indices of the masking operator. This number is given by the index length of the main beam, c_m, and determines the computational cost of the algorithm. For a particular choice of c_m, the RFP algorithm applied to an array exhibits a beamforming error. This beamforming error is given by the reduction in gain of the main

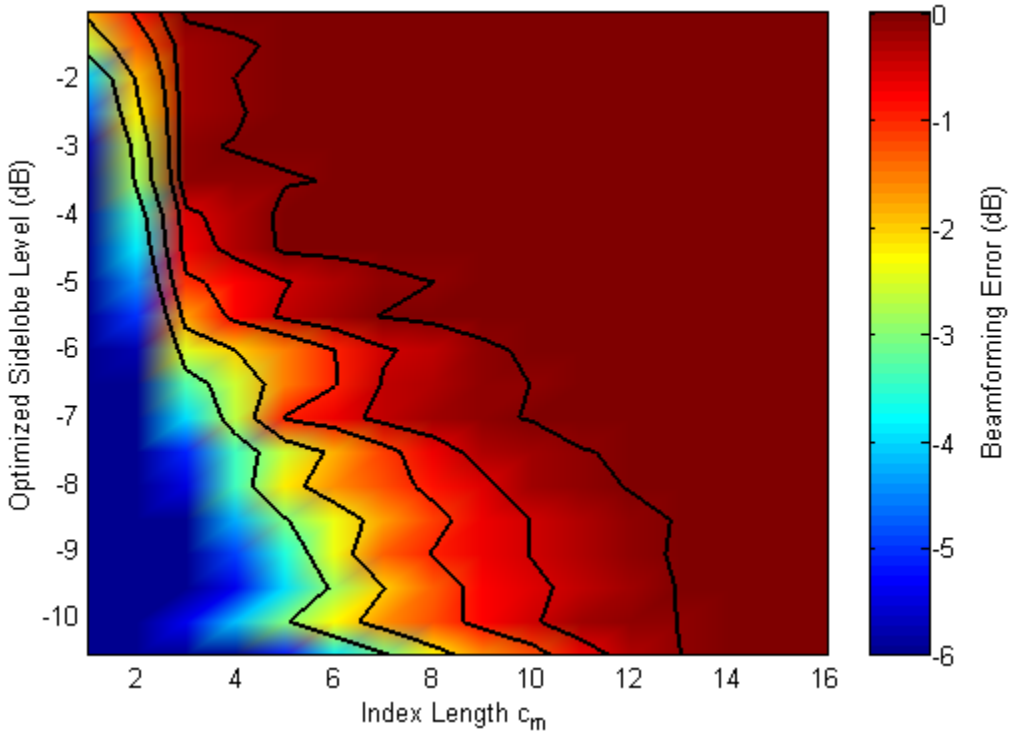

Figure 11.3: The 16 element array sidelobe performance as a function of index length for various GA trials. Contours are for 3, 2, 1, 0.5 and 0.1 dB beamforming error (left to right).

lobe as compared to the ideal value, similar to that given in (11.7). The beamforming error is plotted on the color axis of Figs. 11.3 and 11.4.

The contour lines in Figs. 11.3 and 11.4 represent the relationship between c_m and the optimized sidelobe level for the arrays when the beamforming error is held constant. The sidelobe levels in these figures are the optimized sidelobe levels, and do not include the effects of the beamforming error. It is undesirable to use any value of index length (c_m) that results in a significant amount of error. Several of these contours are overlaid in Figure 11.5 to compare the performance of the 16-antenna and 24-antenna arrays. The contours follow very similar traces, indicating that, for these results, the performance

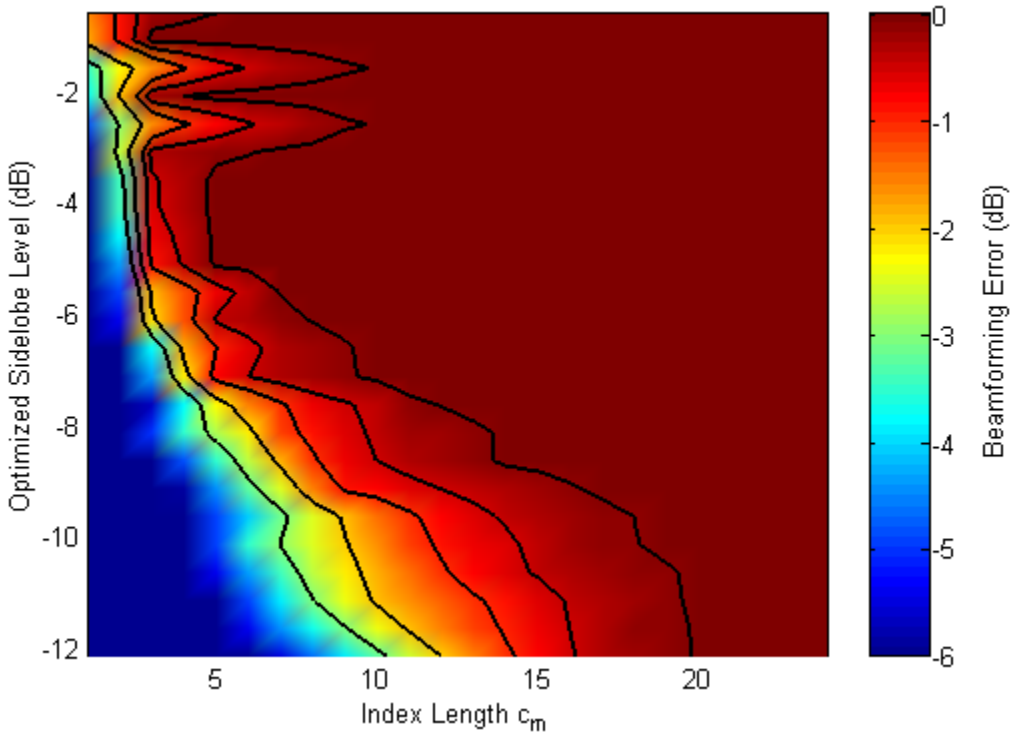

Figure 11.4: The 24 element array sidelobe performance for various GA trials. Contours are for 3, 2, 1, 0.5, and 0.1 dB beamforming error (left to right).

does not vary significantly when the number of antennas is changed. If the number of antennas is increased significantly, the best-case sidelobe levels should improve [32]. It is not known whether the curves will be shifted or simply extended.

There is a tradeoff between the three variables in these plots; it is simultaneously desired to have an array with low sidelobes, low beamforming computational cost, and low beamforming error. It is not possible to simultaneously satisfy all of these requirements. For example, a 16 element array with fully optimized sidelobes and less than 0.1 dB of pointing error requires an index length of 13. A similar array with an index length of five and less than 0.5 dB of pointing error has sidelobes that are 4.5 dB above the optimal level.

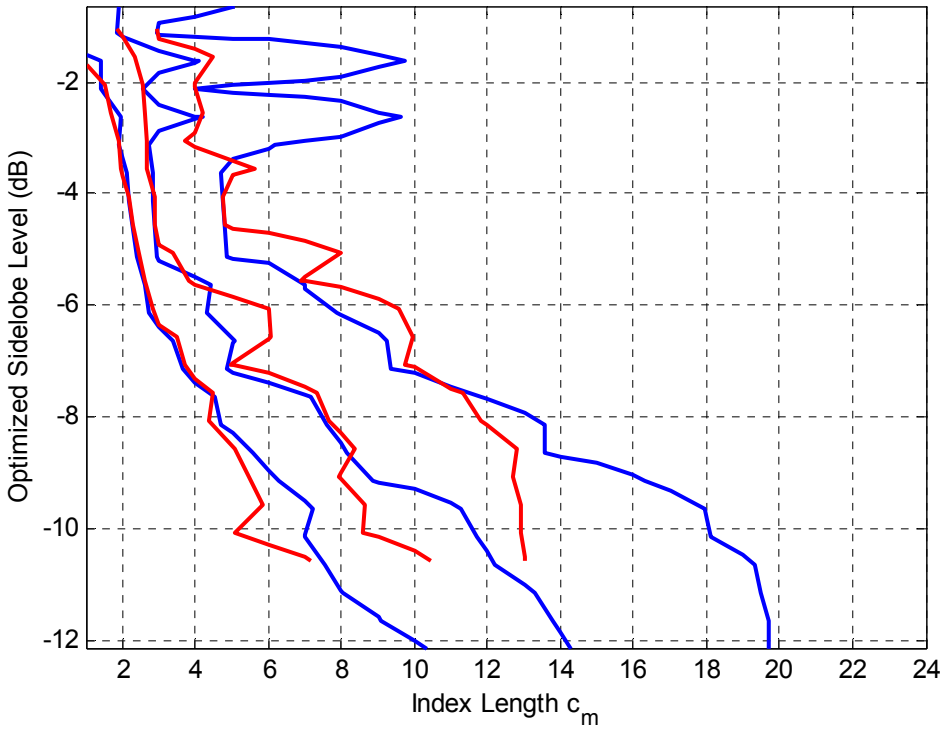

Figure 11.5: Comparative sidelobe performance of the 24 (blue) and 16 (red) element thinned linear arrays. Contours are for 3, 1, and 0.1 dB beamforming error (left to right).

Another concern is selecting the number of bins required to null interfering signals. No significant effect was observed by varying the interference index length, or c_n, other than a slight reorganization of the sidelobes. This number must be at least 1 so that a sufficient number of degrees of freedom is maintained; it will be shown that a value of 2 results in an equal computational cost per-null for the full beam-set BIP and RFP.

11.4 Computational Costs

11.4.1 Number of Operations of a Thinned FFT

One of the significant differences in the computational costs of the three beamforming methods presented here is the number of operations required to calculate

the FFT. When the number of FFT points is high compared to the number of antennas, many inputs to the FFT will be zero, and many of the outputs of the FFT might not correspond to beams in real space. These can be ignored by a process called pruning to reduce the computational cost of the FFT. When comparing the computational cost of the beamforming methods, it is necessary to have an understanding of how the computational cost of the FFT is changed by pruning a set of inputs or outputs.

This computational cost of the pruned FFT can be found by inspection of the FFT butterfly, as presented by Markel [56], but the form given by Lewis [57] is easier to adapt to the present problem. If the FFT of length N has $L = N \cdot 2^{-p}$ nonzero inputs, where p is a positive integer, then the computational cost of the algorithm is approximated by

$$n_{ops} = 6N\left(\log_2 L + \sum_{a=1}^{p} 2^{-a} \right). \tag{11.24}$$

This analysis can be repeated if only $M = N \cdot 2^{-q}$ outputs are needed. Providing that $LM/N \geq 1$ so that the pruned regions of the inputs and outputs do not overlap, (11.24) becomes

$$n_{ops} = 6N\left[\log_2 \left(LM/N \right) + \Sigma_L + \Sigma_M \right], \tag{11.25}$$

where

$$\Sigma_L, \Sigma_M = \sum_{a=1}^{p,q} 2^{-a} . \tag{11.26}$$

Many FFT algorithms exist with a computational cost on the order of $N \log_2 L$, or $O\left(N \log_2 L\right)$ [58-62]. An exception is the wavelet approximate Fourier transform

algorithm, for which Guo and Burrus claim $O(N)$ computational cost for $L < N/2$ [63]. It is also possible to use the chirp-z transform (CZT) [64] for applications requiring certain sampling intervals or ranges; the CZT is a part of several beamforming algorithms [65, 66]. Although [56-63] may be referenced for the exact complexity of various pruned FFTs, Equation (11.25) provides a basis for comparing the beamforming methods.

Because the computational cost of the FFT is linearly dependent on the total number of points, it is necessary to keep the number of non-significant points of the FFT low. If a large number of inputs do not correspond to antennas, then FFT techniques become more complex than direct computation. With the cost of the conventional beamformer (CBF) in (11.3) defined as $8L^2 - 2L$, where L is the number of inputs and outputs, setting the ratio N/L to

$$\frac{N}{L} = \frac{4L-1}{3\cdot(\log_2 L+1)} \tag{11.27}$$

gives the point where the cost of the pruned FFT is equal to that of the CBF.

11.4.2 Computational Cost of Basic and Thinned BIP

The computational cost of Ellingson and Cazemier's BIP algorithm is found by examining the number of complex additions and multiplications that are performed [50]. The total number of operations is $6N\log_2 N + 16Nk - 2k$, where k is the number of interferers that are nulled. If multiple sets of nulls are used, the number of operations increases to $6N\log_2 N + 8Nk + Q(8Nk - 2k)$, where k is the average number of nulls per set and Q is the number of null sets.

When using the beamforming methods presented in this chapter, the sample grid spacing might be smaller than the average element spacing, and the cost of the pruned FFT in (11.25) must be used to determine the computational cost of the algorithm. It is also useful to determine the relationship between the number of antennas (L), the number of desired beams (M), and the number of sample points (N). If the average element spacing and sample grid spacing are defined as $\overline{S}$ and S_g and are in units of wavelengths, then the number of sample points in a linear array is given by

$$\begin{aligned} N_{1d} &= (L-1)\cdot\left(\overline{S}/S_g\right)+1 \\ &\approx L\cdot\left(\overline{S}/S_g\right), \end{aligned} \tag{11.28}$$

where N_{1d} is rounded to the next-highest integer. Note that the approximation holds when the number of antennas is large. For planar arrays this becomes

$$\begin{aligned} N_{2d} &= \left[\left(\sqrt{L}-1\right)\cdot\left(\overline{S}/S_g\right)+1\right]^2 \\ &\approx L\cdot\left(\overline{S}/S_g\right)^2. \end{aligned} \tag{11.29}$$

If the sample grid spacing is less than $\lambda/2$, not all of the Fourier beams will correspond to locations in real space. The desired number of outputs M can be defined as the number of beams in real space. This definition is trivial for a linear array and is given by

$$M_{1d} = 2S_g N. \tag{11.30}$$

A modification of the equation given by Chiavacci and Locke [67] gives the value of

$$M_{2d} = \pi S_g^2 N \tag{11.31}$$

for a planar array. Assigning a value to M is more complex for a volumetric array because few of the beams are in real space.

Given these relationships between L, M, and N, the general form of the computational cost of applying the BIP algorithm to a thinned array is given by

$$n_{ops} = 6N\left[\log_2\left(LM/N\right) + \Sigma_L + \Sigma_M\right] + 8Mk + 8Lk - 2k, \tag{11.32}$$

where Σ_L and Σ_M are given by (11.26). If M and L are small compared to N, this becomes

$$n_{ops} = 6L\left(\overline{S}/S_g\right)\left[\log_2\left(2LS_g\right) + 2\right] + \left(16\overline{S} + 8\right)Lk - 2k \tag{11.33}$$

for a linear array and

$$n_{ops} = 6L\left(\overline{S}/S_g\right)^2\left[\log_2\left(\pi LS_g^2\right) + 2\right] + \left(8\pi\overline{S}^2 + 8\right)Lk - 2k \tag{11.34}$$

for a planar array. Although the computational cost of the algorithm depends on the number of antennas in the array, it also depends strongly on the average spacing between antennas and on the spacing of the sample grid points.

It is clear from (11.32)-(11.34) that the high number of sample points in the dense grid approximation method makes it an unsuitable choice for efficient FFT beamforming with projection nulling. When the antenna positions are quantized to a grid, the sample grid density and the corresponding computational cost of beamforming are significantly

reduced. In the quantization grid approach, if the sample grid is equal to the quantization grid and is almost $\lambda/2$, then FFT beamforming will be exact and the computational cost for a linear array will be given by

$$12L\overline{S}\left(\log_2 L+1\right)+\left(16\overline{S}+8\right)Lk-2k\,. \qquad (11.35)$$

Although this method is much more efficient than the dense grid approximation, the complexity still rises linearly with the average spacing. Using (11.27) it can be shown that, for a linear array of 1024 antennas, the cost of the FFT is equal to that of the CBF for an average spacing of more than 62λ. However, if the array is distributed on a plane, the average spacing drops to only 5.5λ. Furthermore, if the array is distributed in a volumetric cube, this spacing drops to only 2.5λ.

11.4.3 Computational Cost of RFP

The computational cost of the Reduced Fourier-space Projection method is found by examining the implemented form of (11.21). As with the BIP method, the FFT of the inputs need only be computed once. Unlike the BIP method, the other quantities can be precomputed. The execution of (11.21) will require M inner products of length C, where M is the number of beams to form and C is the total index length of the algorithm, given by c_m+c_nk. The computational cost of the RFP algorithm is given by

$$n_{ops}=6N\cdot\left(\log_2 L+1\right)+\left[8\left(c_m+c_nk\right)-2\right]\cdot M\,, \qquad (11.36)$$

where N is the number of sample grid points, c_m and c_n are the index lengths of the main beam and required nulls, k is the number of required nulls, and M is the number of beams formed. The index lengths are related to the number of significant bins in the

Fourier transform of the inputs, and they determine the accuracy of the algorithm. The relations in (11.28) and (11.29) also apply in (11.36) for finding N, but the optimized thinned linear array model allows the sample grid spacing to be larger than $\lambda/2$, which significantly reduces the cost of the FFT as compared to the BIP methods.

The decision of whether to pre-form common nulls with BIP or to compute all nulls with RFP can be made by comparing the computational costs of the algorithms. The cost-per-null of (11.21) and (11.5) is equal for the case when $M = L/(c_n - 1)$. For the case when the left side of the equation is larger, then it is more efficient to pre-form nulls with BIP. For the case when the right side of the equation is larger, then it is more efficient to use the RFP nulling.

The overall complexities of (11.5) and (11.21) can also be compared for a situation where the M desired beams correspond to a subset of the Fourier beams. The complexities of the algorithms are equal for the case when

$$M = \frac{Lk - 0.25k}{(c_n - 1)k + 0.75}. \tag{11.37}$$

For the case when M is larger than the quantity on the right side of the equation, it is faster to use the BIP algorithm, but when M is smaller than the quantity on the right side, it is faster to use RFP.

11.5 Comparing Methods

The equations describing the cost of the CBF, sparse FFT, BIP with the dense grid approximation (DG), BIP with quantization grid arrays (QG), and RFP with $S_g = \overline{S}$ were implemented for an array of 1024 elements with a one-wavelength average spacing. The

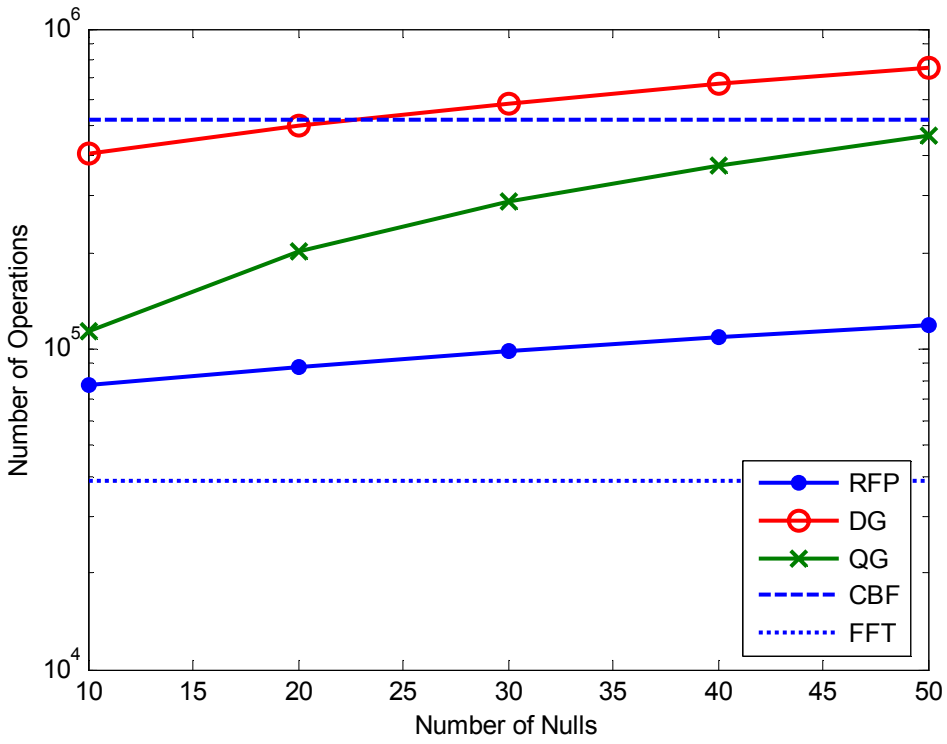

Figure 11.6: Algorithm complexity for a 1024 element thinned linear array with 64 beams as a function of the number of nulls.

dense grid approximation used a sample grid spacing of $\lambda/20$; the quantized grid array used a sample grid spacing of just under $\lambda/2$. The RFP cost function employed a main beam index length of 12 and an interference index length of 2.

Figure 11.6 contains plots comparing the costs as a function of the number of nulls for a scenario in which 64 beams are formed. As expected, RFP requires the fewest number of operations, followed by the quantization grid array and the dense grid array. The computational cost for each method increases as the number of nulls increases. The CBF requires fewer operations than the dense grid approximation when as few as 24 nulls are formed on each beam; it is faster than the quantization grid array method when as few as 52 nulls are formed on each beam. The RFP method requires less than half the number

Table 11.1:
Overview of Beamforming Methods for Aperiodic Arrays

Method	Solution Type	Orthogonal Beams	Steerable Beams	Approximate Base Cost	Approximate Null Cost
CBF	Exact	Yes	Yes	$O(LM)$	-
DG	Approx	No	No	$O(N \log_2 L)$	$8M + 8L$
QG	Exact	No	No	$O(N \log_2 L)$	$8M + 8L$
RFP	Approx	Yes	Yes	$O(N \log_2 L)$	$8c_n M$

of operations as the quantization grid array, and can form more than 400 nulls per beam before requiring more operations than a conventional beamformer.

11.6 Conclusions of RFP Beamforming

Several strategies were examined for applying FFT beamforming methods with interference projection nulling to thinned array geometries; an overview of these is contained in Table 11.1. The conventional beamformer (CBF) creates exact beams and represents optimal performance, yielding exact shapes and locations for both beams and nulls, and serves as an upper bound for the computational cost of useful algorithms. The dense grid approximation (DG) is a successful application of the BIP algorithm to an arbitrary aperiodic array, but requires a prohibitively large number of sample points. The quantization grid method (QG) restricts the geometry of the thinned array to which it can be applied and achieves a significant cost reduction compared to the dense grid approximation by increasing the sample grid spacing to almost $\lambda/2$.

Although the Reduced Fourier-space Projection method (RFP) requires the array to conform to a specific design, it significantly reduces the cost of beamforming by both

increasing the sample grid beyond $\lambda/2$ and reducing the per-null computational cost. Additionally, the RFP algorithm allows for steerable beams with independent nulls, something not provided by the BIP-derived algorithms. Further study of the thinned linear array model will determine the performance of this method for a large number of antennas with large average spacing. It is desired to produce both an extended set of simulated results from the genetic model, as well as an analytical description of the performance properties of the thinned linear array.

Part 4:

The Omni Directional Interference Nulling Array

CHAPTER 12.
OVERVIEW OF THE ODIN ARRAY

The new elemental antenna and array theories presented in this dissertation are integrated in the phased array demonstrated as a part of this research. This Omni Directional Interference Nulling array, or ODIN, consists of six elemental PLMA antennas. The antennas have a center frequency of 2245 MHz and a bandwidth of 10%, as was shown in Chapter 5. The elements are distributed in a volumetric configuration to provide a uniform beamwidth during scanning and to provide an opportunity to demonstrate the volumetric target tracking techniques of Chapter 10.

The number of antennas is too few to apply any grating lobe optimization, so the choice of topology, shown in Figure 12.1, was somewhat arbitrary. The *x*-axis of the array points to 352° azimuth. This choice was made because the orbit of the NASA

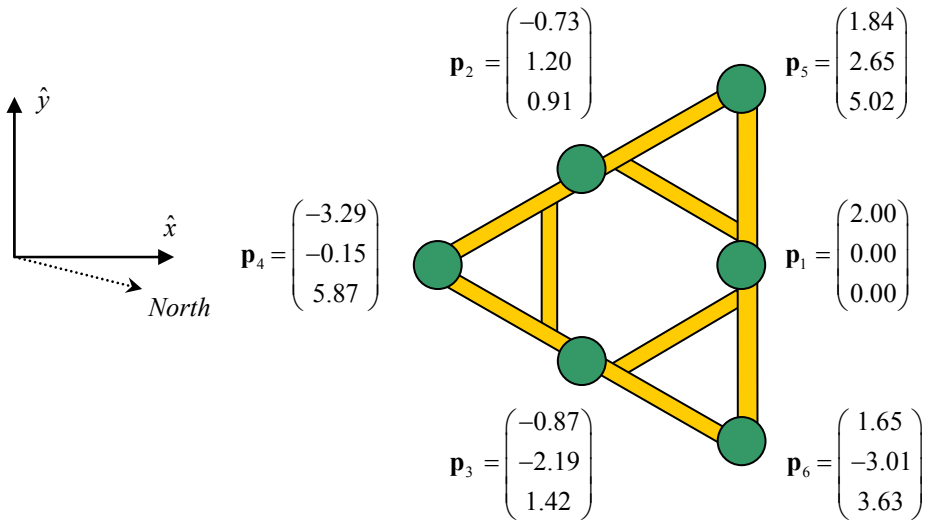

Figure 12.1: Diagram of the array layout. Positions are in wavelengths at 2245 MHz.

Figure 12.2: Photograph of the final array.

satellite EO-1 used in testing the array is inclined to $98°$. For the night passes recorded for this research, the nominal azimuth at the acquisition of signal (AOS) of the satellite is $172°$ and the nominal azimuth at the loss of signal (LOS) is $352°$. Figure 12.2 contains a photograph of this array on the roof of the Van Leer Electrical and Computer Engineering Building. Four square meters of Eccosorb^{TM} microwave absorbing foam were distributed around the base of the array and the receiver enclosure, as shown in Figure 12.3. This foam reduced signal reflections from the roof and was necessary because the antennas have non-zero gain at angles below $El = 0°$, as was shown in Chapter 5.

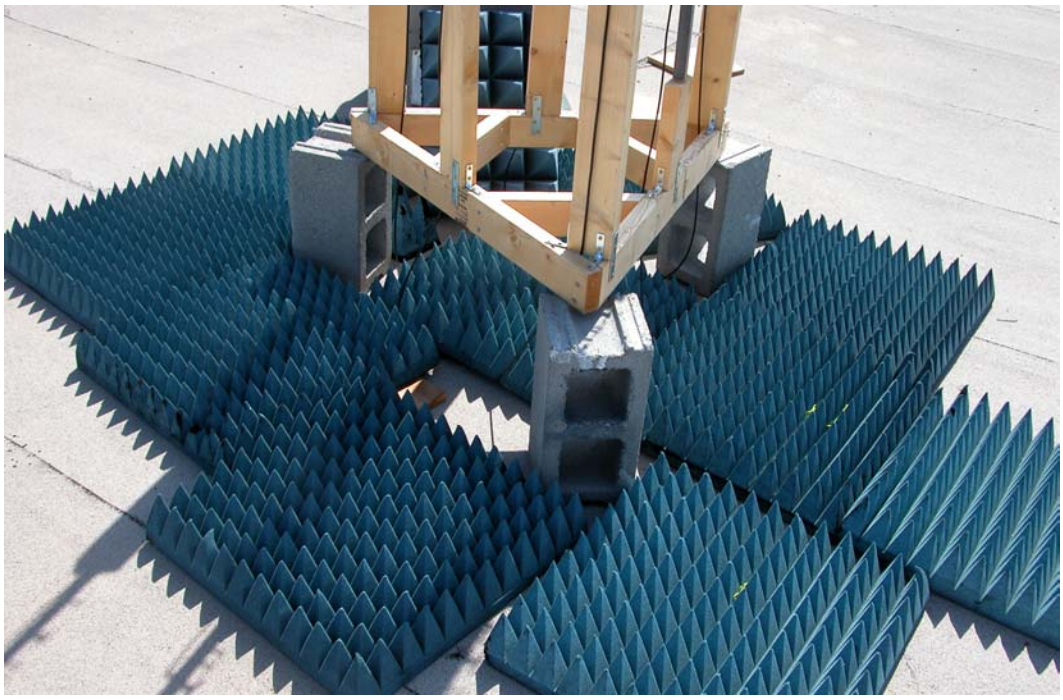

Figure 12.3: Photograph of the Eccosorb surrounding the array.

The isolation between the receivers used with each element is estimated at 50 dB. This number can be improved by better sealing of the receiver enclosures and by using signal cables that have better isolation than the RG-316 used inside the enclosure containing the individual receivers. Mutual coupling between antennas in this array was measured with a network analyzer. The magnitude of coupling S_{ij} between any two channels was estimated at less than -20 dB. As a result, the effects of mutual coupling were ignored.

Chapter 13 focuses on the RF receiver system of this array; Chapter 14 focuses on the final system configuration and the back-end synchronous digital recording system. This array was used to record data from four pass events with the NASA satellite EO-1. Data from these passes is contained in Part 5 of this dissertation.

CHAPTER 13.
MULTICHANNEL RADIO RECEIVER SYSTEM

13.1 Introduction

A custom receiver system was designed and constructed to facilitate demonstration of the ODIN array. Complete design and construction information is available in the receiver documentation [68]. This chapter covers an overview of the properties of this receiver.

These boards were dubbed JENNIE, an acronym for "Just Enough Nearly Impeccable Electronics." The collection of JENNIE receiver boards is referred to as the JBoard subsystem in the Matlab-based code that operates the ODIN array. The six boards constructed serve as the interface between the antennas and the digital capture boards and include low-noise amplification in their function. A basic block diagram is shown in Figure 13.1. A photo of an assembled board is shown in Figure 13.2. A summary of the characteristics of the receiver is contained in Table 13.1.

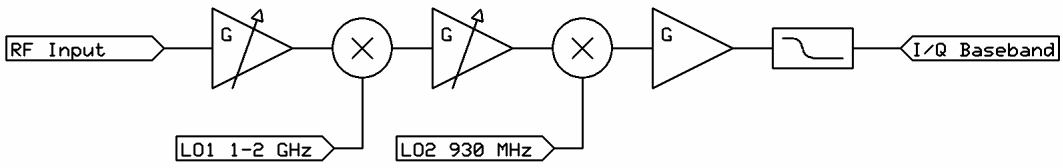

Figure 13.1: Functional block diagram of the receiver.

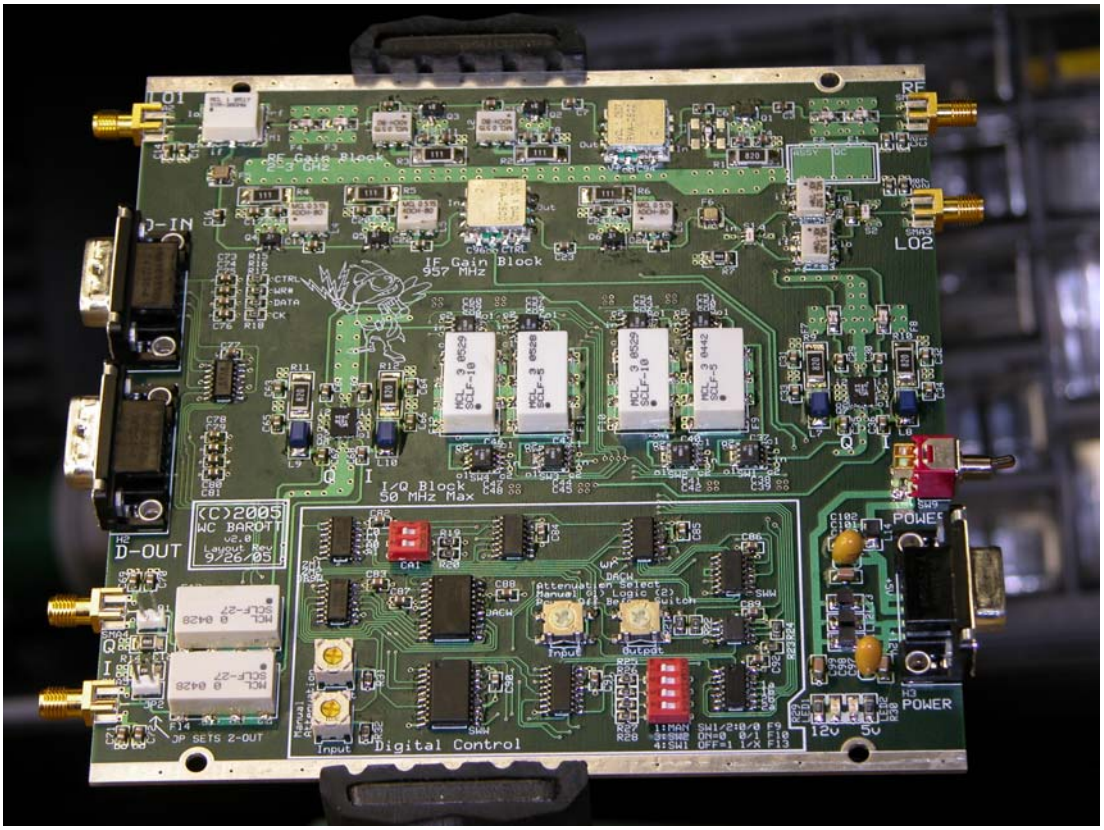

Figure 13.2: Photograph of an assembled JENNIE receiver board.

Table 13.1:
Characteristics of the JENNIE Receiver

Characteristic	Value
Signal Inputs	
RF Input Frequency	2000 – 2650 MHz**
Maximum Input Power*	-87 dBm
Input Referred Noise Temperature*	270K
Estimated Sensitivity*	-144 dBm / KHz
Oscillators	
First Local Oscillator	Variable, +17dBm
Second Local Oscillator	930 MHz, +16dBm
Signal Outputs	
Output Bandwidth	Selectable 6 MHz, 12 MHz, 30 MHz
Maximum Output Power P_{1dB}	+19 dBm
Normal Output Power	0 dBm
Power and Connections	
Power Dissipated	10.1W
Est. +12V Current	800mA
Est. +5V Current	100mA
Powerline RFI Immunity	>100 MHz
Signal Connections	5x SMA
Control Connections	1 DB9/M input, 1 DB9/M buffered output
Power Connections	1 DB9/F with +12V and +5V lines
Economics	
Total Cost per Board	$335
Assembly Time	8 Hours

*Specified for least RF and IF attenuation.

**Upper operating frequency limited by the third order mixing product $LO_1 - 2LO_2$.

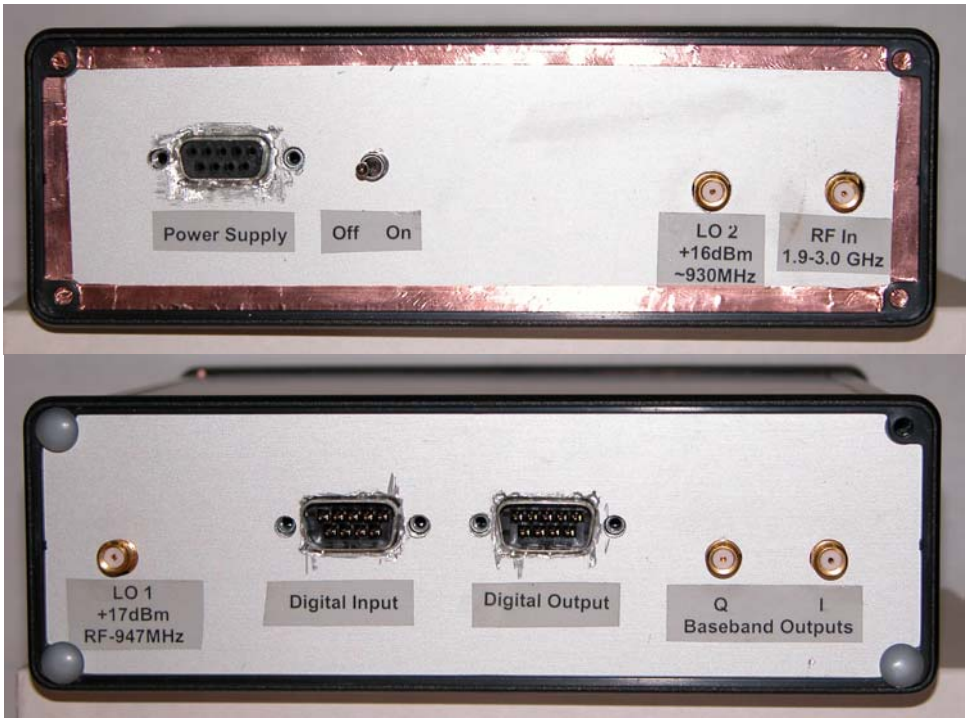

Figure 13.3: Photographs of the front panel of a JENNIE receiver (top) and back panel (bottom). Input and output ports are labeled.

13.2 Ports

13.2.1 External Ports

The JENNIE board has five SMA ports, two DB9/M ports, and one DB9/F port. They are distributed between the front and back panel of the device, as shown in Figure 13.3. The SMA ports include inputs for the RF signal, two local oscillators, and inphase and quadrature baseband outputs. The DB9/M ports include an input and a buffered output for the control bus; the DB9/F port is used to provide power to the board.

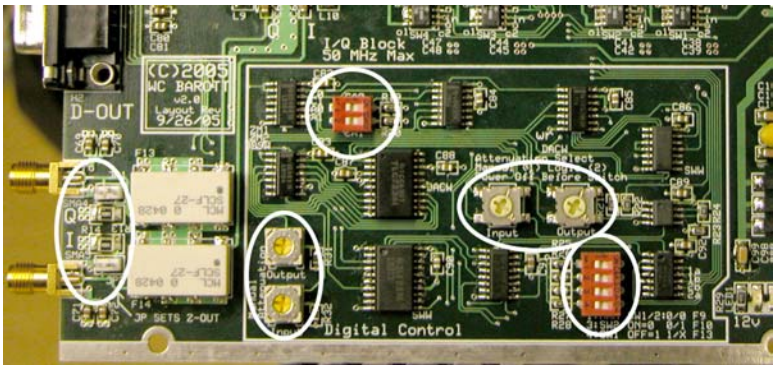

Figure 13.4: Locations of the internal connections. From left to right: Termination jumper, attenuation potentiometer, card address setting, manual attenuation enable, and manual switch selection.

13.2.2 Internal Connections

Although the JENNIE board is programmed by a computer, it has several internal switches, shown in Figure 13.4. These include the 2-Position DIP for card address selection, 4-Position DIP for manual bandwidth selection, trimpots and switches for manual attenuation control, and jumper headers for 50Ω termination of the output signals.

13.3 Theory of Operation

The board layouts were created using the ExpressPCB™ design tool. The microstrip analysis tool Sonnet™ evaluated the performance of selected trace geometries, such as RF vias. The boards were assembled using a combination of hand and manual reflow soldering. The board has four layers, and the 50Ω trace width is 20 mils [28]. All traces are kept short to minimize transmission line effects. The board utilizes a three-stage down-conversion process and a digital control subsystem controls the gain and bandwidth of the receiver.

Special care was taken in the selection of the RF components with regard not only to noise figure (NF) and power capacity, but also to the third order intercept point (IP3). The third order intercept point relates to the strength of intermodulation (IM) products in the signal output of a device; these are largely third-order mixing products caused by nonlinearities [54]. Many narrow-band communications systems use filtering before the LNA to mitigate IM. In a wide-band receiver, such as the JENNIE receiver, IM distortion caused by strong signals can mask the presence of weaker signals. S-band satellite receivers are particularly vulnerable to IM because of the strong signals radiated by terrestrial repeaters of Sirius and XM satellite radio. These repeaters broadcast signals that are not only 60 dB stronger than received LEO satellite signals, but are also only 50 MHz away from the desired satellite signals [69].

13.3.1 The RF Subsystem

The RF subsystem, shown in Figure 13.5, consists of the components between the RF input and the IF output of the first mixer. This block contains input filtering, low noise gain, variable attenuation, and mixing to IF.

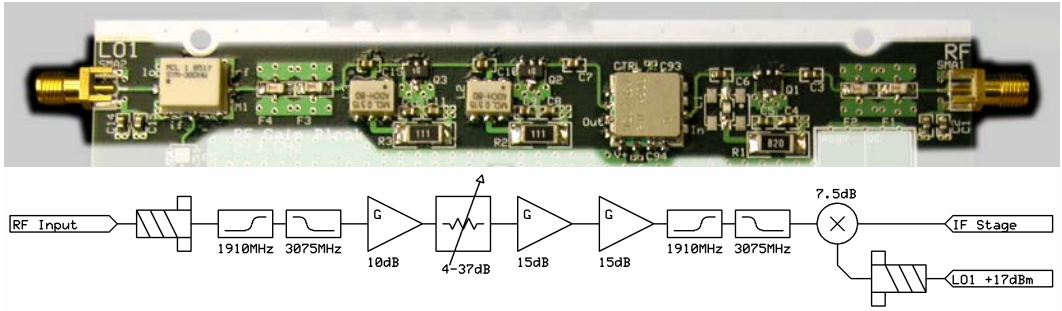

Figure 13.5: Photograph and block diagram of the RF subsystem.

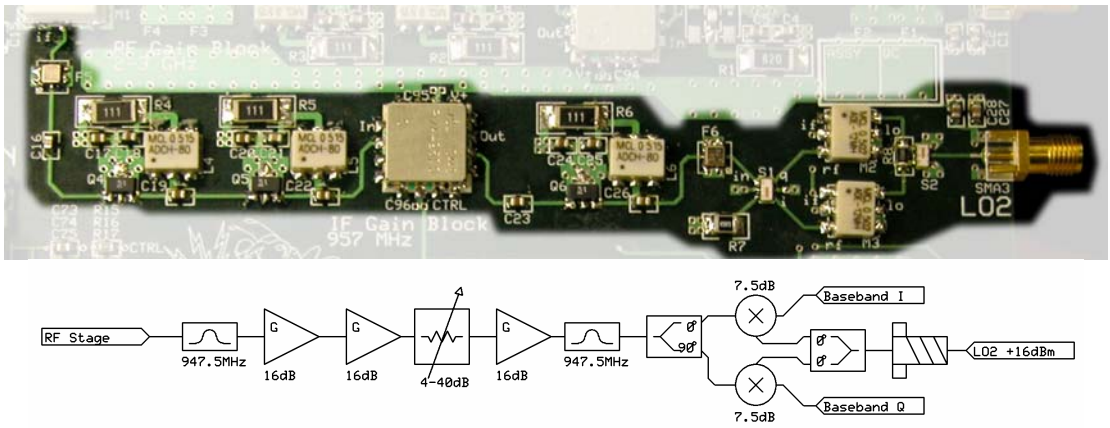

Figure 13.6: Photograph and block diagram of the IF subsystem.

13.3.2 The IF Subsystem

The IF subsystem, shown in Figure 13.6, consists of the components between the output of the first mixer and the output of the second mixer. It contains blocks for filtering, gain, variable attenuation, and I/Q splitting of the signal. The IF filter is a 30 MHz filter centered at 947 MHz. While inexpensive, this choice makes the board vulnerable to interference from transmitters in this band.

13.3.3 Attenuator

The RF and IF attenuator is Minicircuits RVA-2500 voltage variable attenuator. This unit requires a +5V reference voltage and a 0-12V control voltage. A typical curve of attenuation versus control voltage is shown in Figure 13.7.

13.3.4 The Baseband Subsystem

This subsystem is shown in Figure 13.8 and consists of the components between the IF stage and the signal output. It contains gain, selectable bandwidth filtering, and optional 50Ω termination. A bank of semiconductor SPDT switches is used to allow the

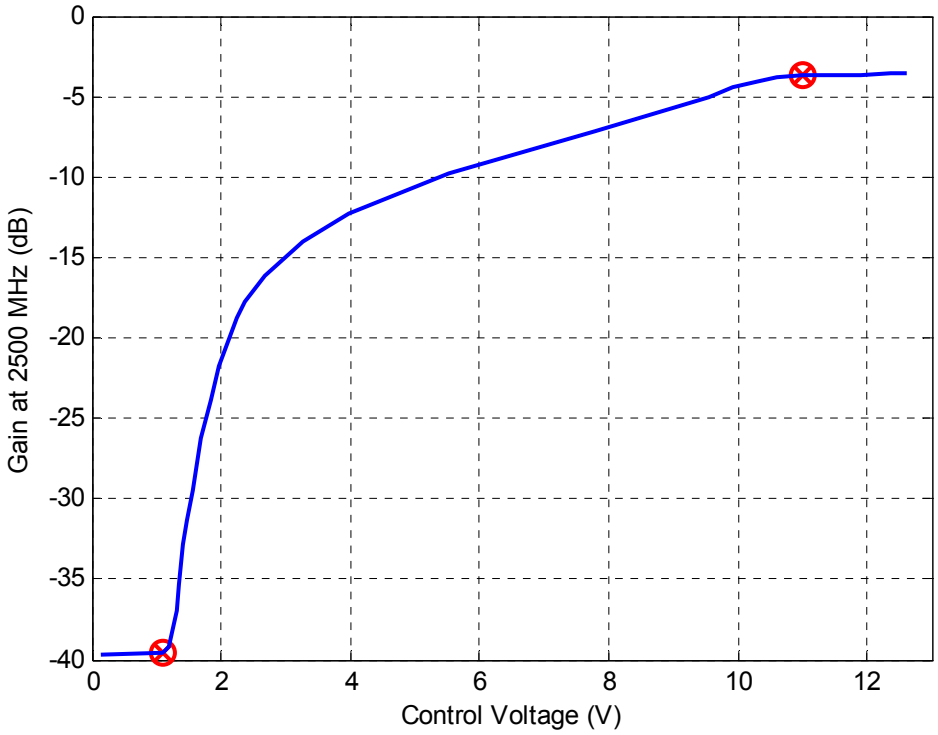

Figure 13.7: Attenuation versus control voltage for the variable attenuator. Marks indicate full attenuation and minimum attenuation points at approximately 1.1V and 11.0V.

board to select one of three filters to apply to the output signal. These filters are 6 MHz, 12 MHz, and 30 MHz. The control line of this switch is coupled to the power planes to prevent electromagnetic interference (EMI) from modulating the switch.

13.3.5 Digital Control Subsystem

The digital control subsystem, shown in Figure 13.9, accomplishes three specific tasks. It processes data received from the computer, sets the baseband switch control values, and sets the attenuator voltages. It is noted that an extensive search was required to locate the op-amp used to control the attenuators. This amplifier must provide up to 30 mA of current at voltages within 100 mV of the +12V supply.

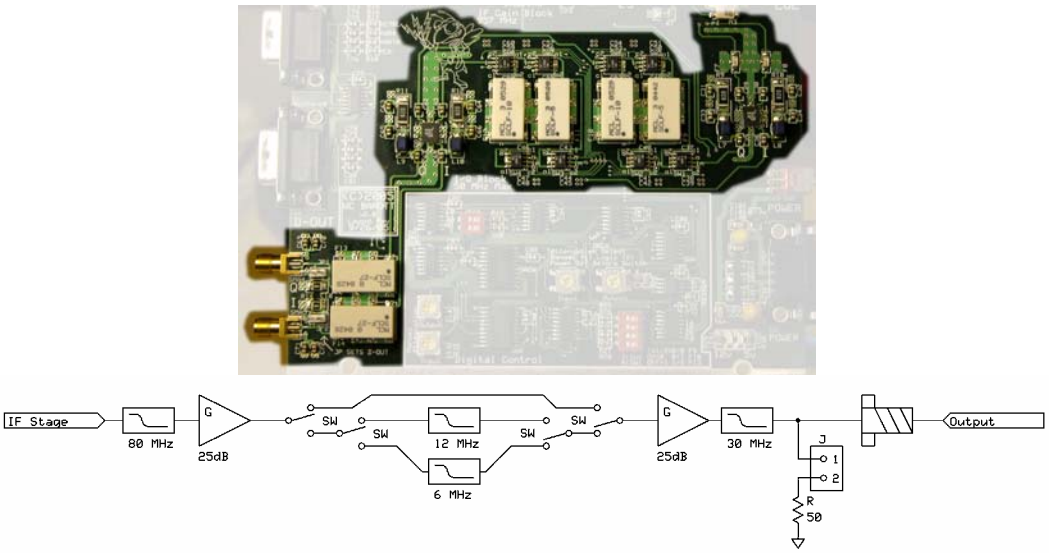

Figure 13.8: Photograph and block diagram of the baseband subsystem.

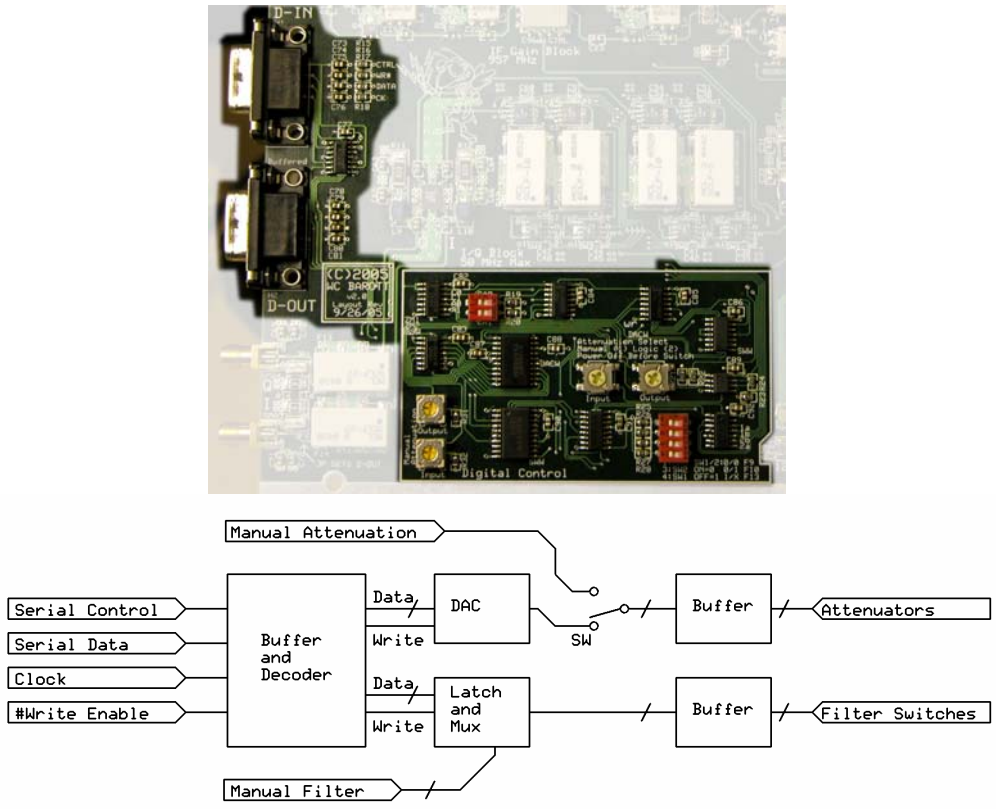

Figure 13.9: Photograph and block diagram of the digital control subsystem.

13.4 Programming the Board

The RF attenuation, IF attenuation, and output bandwidth are programmable. The receiver is programmed through a four-wire serial interface bus by loading two serial shift registers with data and then momentarily asserting the write enable pin. Each board buffers the input control signals to an output port, where they can be repeated to the next board on the bus. Boards can be assigned unique addresses or, as was the case in this research, be assigned the same address so that they are programmed simultaneously.

Programming signals originate onboard the digital output block of a CH3160 PCI data acquisition card (discussed further in the following chapter). Programming is accomplished through a Matlab-based interface. The code is abstracted so that Matlab maintains a structured variable with entries mirroring the programmable characteristics of the receiver. Values on the boards are changed by assigning new values to the structured variable. Full descriptions of the programming interface can be found in the JENNIE documentation.

13.5 Calibration

The boards are calibrated so the characteristics of the RF input signal can be inferred from the measured baseband signal. Several megabytes of calibration data are stored for each board. This data includes the gain as a function of input frequency, output frequency, and attenuator voltage. Values are also stored for the phase differential between the I and Q channels, as well as the phase differential among different boards.

13.6 Assembly into the JBoard Receiver

Six completed JENNIE receivers were assembled into one enclosure for the purposes of the array demonstration. This enclosure is shown in Figure 13.10. The enclosure is self powered and includes amplification and splitting for the local oscillators. It also included multiple fans to disperse the heat generated by the estimated 80W of dissipated power. The unit was stored near the antenna structure in a climate controlled enclosure.

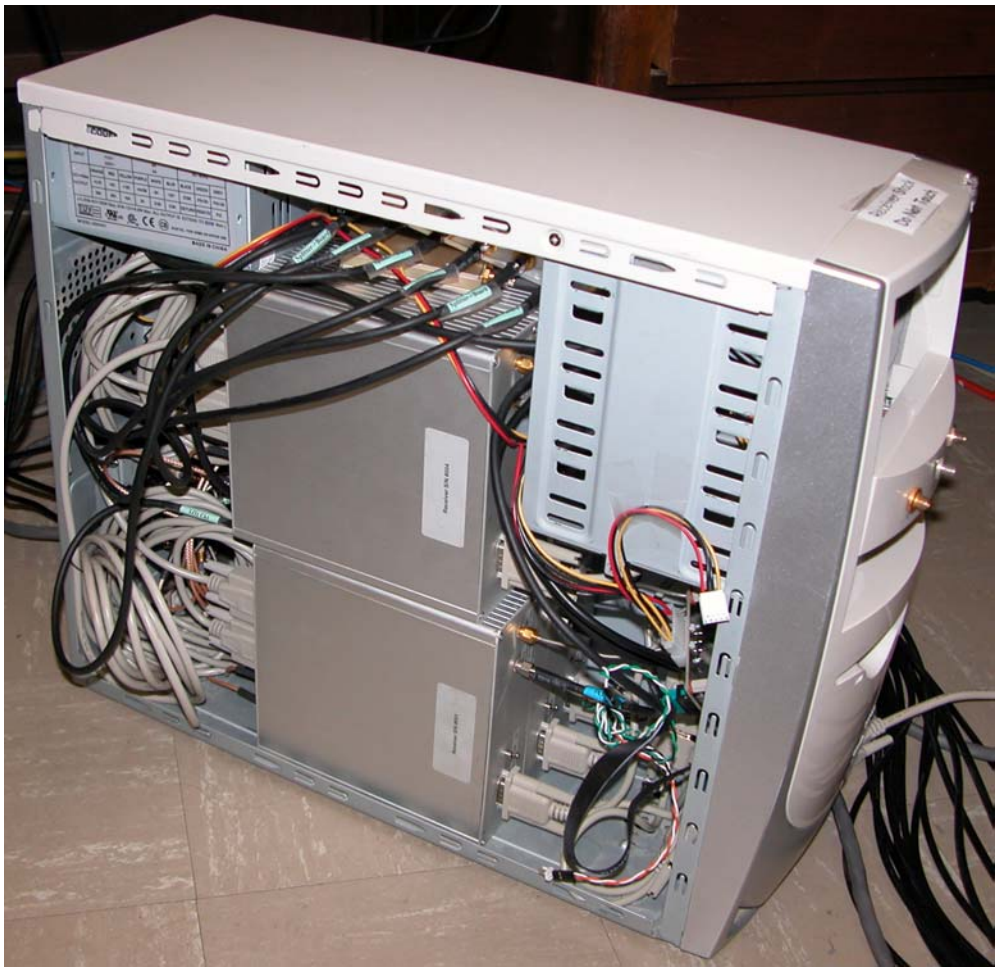

Figure 13.10: Photograph of the six channel receiver stack.

CHAPTER 14.
SYNCHRONOUS DATA ACQUISITION SYSTEM

14.1 Digitizing Baseband Data

Three PCI data acquisition cards (Exacq Technologies model CH3160) were obtained to record the signals produced by the JBoard unit. Each card has four synchronously sampled inputs and can sample a total of 40 mega-samples-per-second (MS/s), or 10 MS/s per-input [70]. The digitizers sample in-phase and quadrature signals from each JENNIE receiver channel at 10 MS/s for a total of 20 mega-complex-samples per second per-channel (MCS/s). The digitizers can phase-lock their internal clocks to an external 80 MHz clock and can start a capture cycle based on an external trigger.

These cards are integrated into three computers (designated Pebbles, Dino, and BamBam) linked via Ethernet and operated with Matlab-based programs so the master computer, Pebbles, controls data acquisition on the slave computers. Several signal sources are integrated into the system and controlled through a GPIB interface. A photograph of the final capture system is Figure 14.1, and a block diagram is contained in Figure 14.2. The system can be controlled remotely through a LAN interface.

Integrating this system and ensuring synchronous data capture required completion of three primary tasks. First, the synchronization error between digitizers was determined to a resolution better than 1 ns, even though the time between consecutive samples is 100 ns. Second, synchronous trigger pulse generation was accomplished to initiates capture sequences. Finally, a calibration program was developed to synchronize the digitizers, measure the synchronization errors, and select the trigger pulse timing.

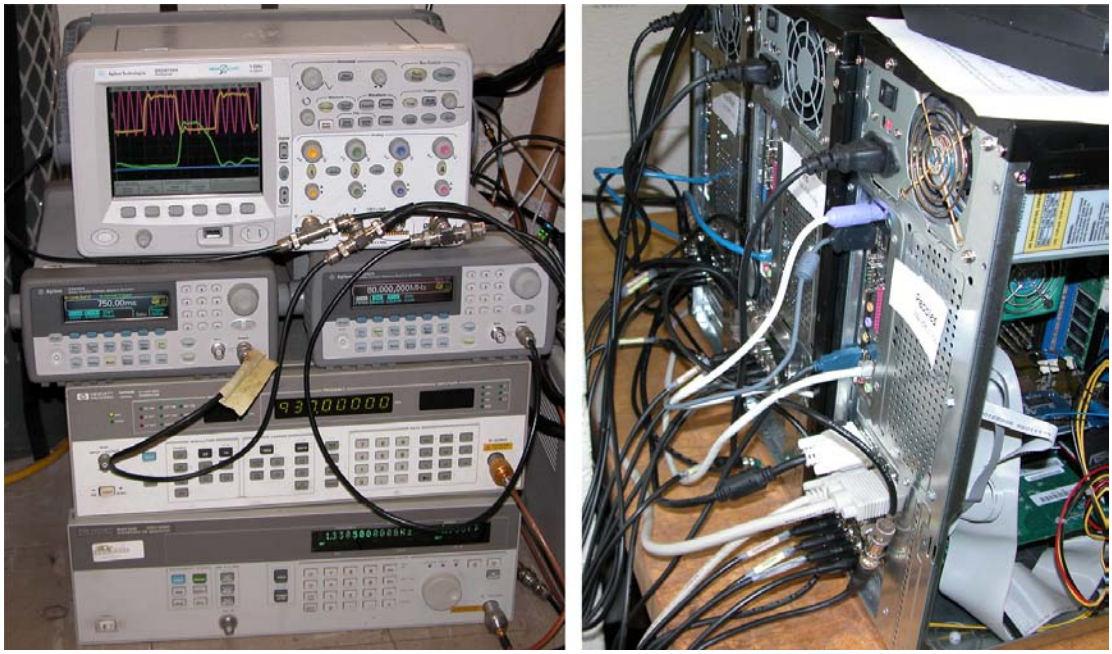

Figure 14.1: The signal sources, except for the sawtooth wave generator (left). The three computers housing the digitizers (right).

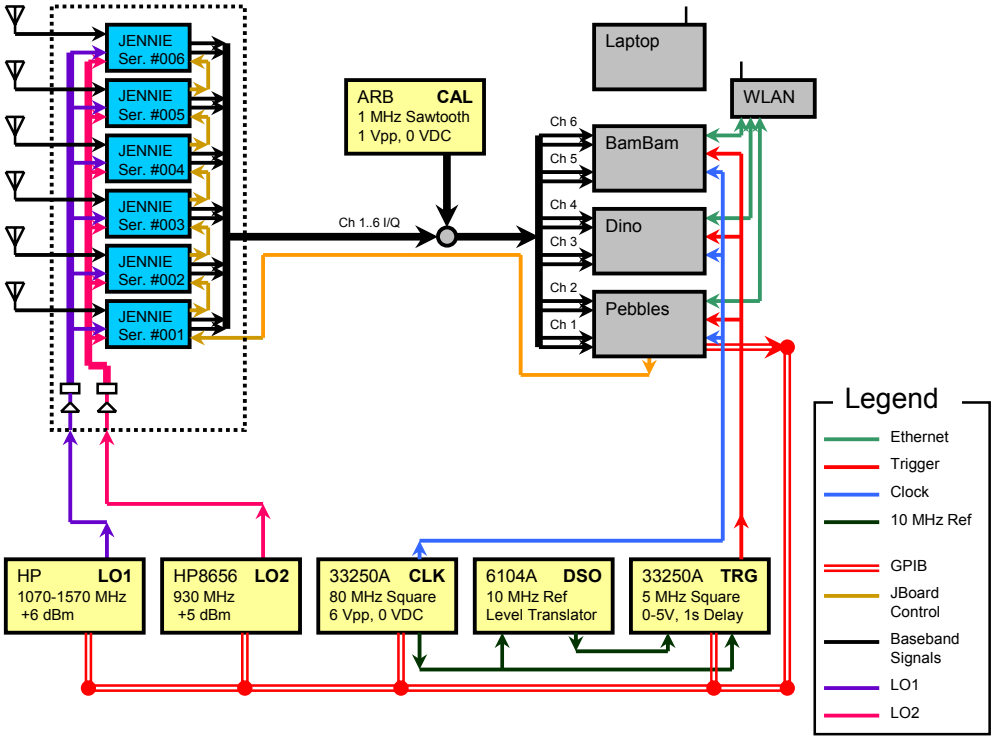

Figure 14.2: Block diagram of the final data acquisition system.

14.2 Determination of Sample Offset

For an accurate phased array system, it is imperative that the digitizers capture data synchronously (at the same time) and any synchronization errors, or timing offsets, be well characterized. Although the time between samples taken at 10 MS/s is 100 ns, a timing offset of just 10 ns results in more than a 20° phase offset at a baseband frequency of 6 MHz. Several processes cause timing offsets between channels, and two such processes are considered here.

First, if two digitizers record data based on different sample clocks, then the timing difference between the clocks will result in a timing offset in the recorded data. This effect is exacerbated if an asynchronous trigger initializes a capture sequence, because the timing of the trigger pulse determines which digitizer begins recording first. An example of this type of error is shown in Figure 14.3. If the trigger fires at $t = 20$ ns, then the data from the second digitizer will lead the data from the first digitizer by 30 ns. If the trigger fires at $t = 40$ ns, the data from the second digitizer will lag the data from the first digitizer by 70 ns. Methods of preventing this type of error are discussed later in this chapter.

Even if the digitizers record data based on the same sample clock, a second effect can cause timing offsets between channels. These errors are due to the difference in propagation time of a signal, such as a clock, from the signal source to the digitizers. These errors are systematic and can be corrected in the recorded data. For example, in the system shown in Figure 14.2, the clock and trigger signals experience a time delay as they propagate from the first computer (Pebbles) to the second computer (Dino) and

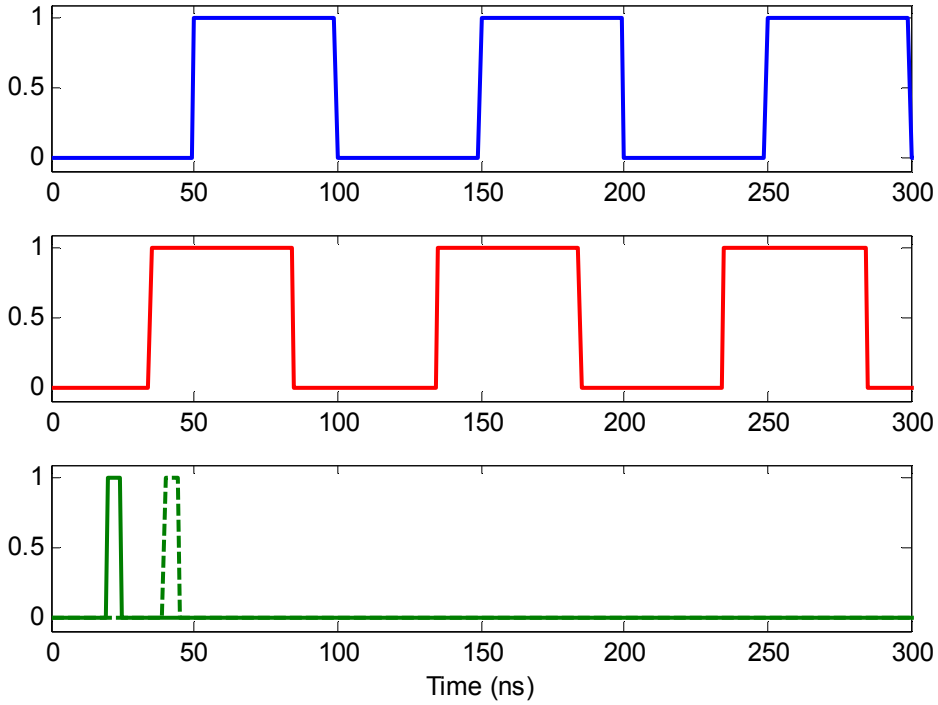

Figure 14.3: Illustration of synchronization errors due to different sample clocks and an asynchronous trigger. The second clock (red) is 30 ns ahead of the first clock (blue). Possible triggers are indicated at 20 ns (green, solid) and 40 ns (green, dash).

finally to the last computer (BamBam). Between Pebbles and Dino, both signals exhibit a delay of 2.1 ns; between Dino and BamBam, the delay is 2.5 ns.

The first step to ensuring synchronization between digitizers is accurately determining the timing offsets. The timing offset between channels is measured by switching the signal source of the digitizers from the JBoard system to the arbitrary wave generator shown in Figure 14.2. The sawtooth wave synthesized by this generator has a frequency of 1 MHz and a voltage range of $\pm 0.5\,\mathrm{V}$; this wave is recorded by each digitizer. Because the system must measure the time delay to a resolution much better than one sample period, it cannot simply estimate time delay by a sample offset. Instead, the time delay between the sampled data, $x_1(t)$ and $x_2(t)$, is determined by the

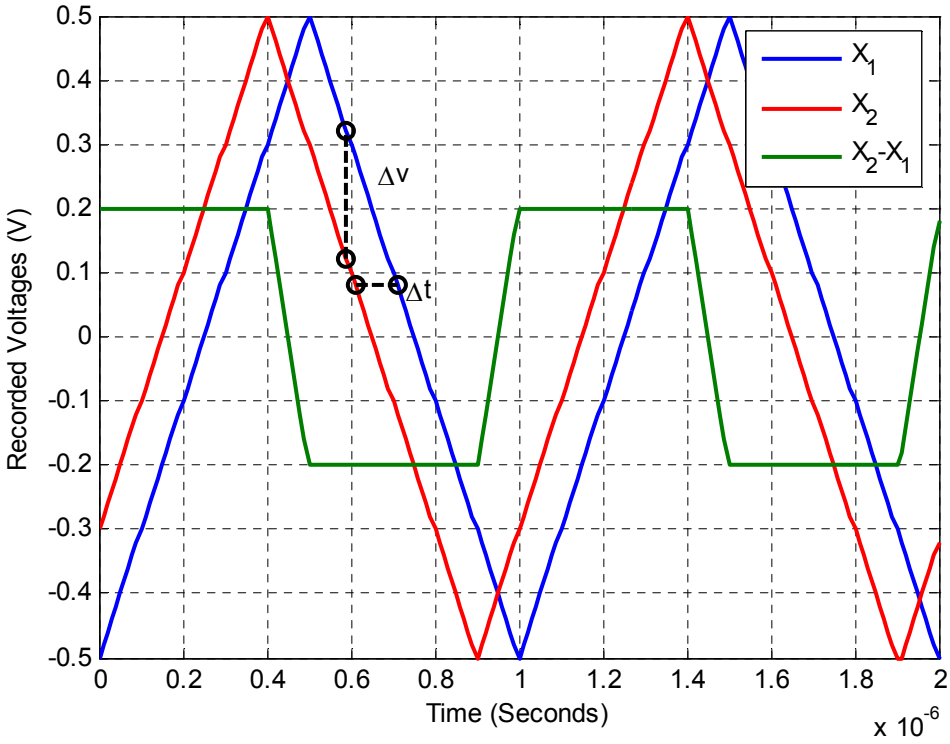

Figure 14.4: Illustration of time delay measurement using a sawtooth signal.

difference in recorded voltage as compared to the slew rate of the input signal, as shown in Figure 14.4. The time delay between channels is calculated by

$$\Delta t_s = \left| \frac{\overline{\overline{(x_1 - \mu_1) - (x_2 - \mu_2)}}}{SR} \right|, \tag{14.1}$$

where μ_1 and μ_2 are the mean values of x_1 and x_2, and the slew rate is found by

$$SR = \left| \overline{\overline{\frac{dx_1}{dt}}} \right|. \tag{14.2}$$

The double bar, $\overline{\overline{X}}$, is a mean operator that only acts on the largest 50% of the data and eliminates the samples near the peak of the sawtooth wave from the analysis. This is

necessary for two reasons. First, the voltage difference in the transition regions, such as between $0.4\ \mu s$ and $0.5\ \mu s$ in Figure 14.4, does not accurately reflect the time difference between the two signals. Second, the sawtooth wave used in the calibration process exhibits a lower slew rate near the peaks than over the rest of the wave. The slew rate is scaled to volts-per-nanosecond so Δt_s is in units of nanoseconds.

The data recorded by the digitizers contains zero-mean Gaussian white noise (GWN) with a standard deviation of $\sigma \approx 0.50$ mV. If the measured timing offset, Δt_s, is larger than 1 ns, this noise corresponds to zero-mean GWN in the estimated timing offset of a single sample (prior to evaluating $\overline{\overline{X}}$) with a standard deviation of $\sigma \approx 0.35$ ns. The mean operator in Equation (14.1) averages 500 sample points, reducing the standard deviation of the GWN in the estimated value Δt_s by a factor of $\sqrt{500}$ to about 16 ps. The accuracy limit of the timing offset measurement, as given by the 3σ (99.7%) confidence range, is ± 48 ps [55]. The actual accuracy might be worsened by the use of the $\overline{\overline{X}}$ operator in the presence of noise.

The GWN in the recorded data establishes a lower bound for the timing offsets that can be determined by this method. If the timing offset is less than 1 ns (chosen based on the 3σ point of the GWN) then the samples of the recorded voltage difference between the signals $x_1(t)$ and $x_2(t)$ will not all have the same sign for the rising (or falling) edge of the sawtooth wave. Negative samples of the estimated timing offset will be mirrored on top of positive samples by the absolute value operator in Equation (14.1), changing the sample distribution, as shown in 14.5. The distribution of samples for the estimated timing offset no longer represent a GWN process, and the mean of the measured data does not match the actual timing offset between the signals.

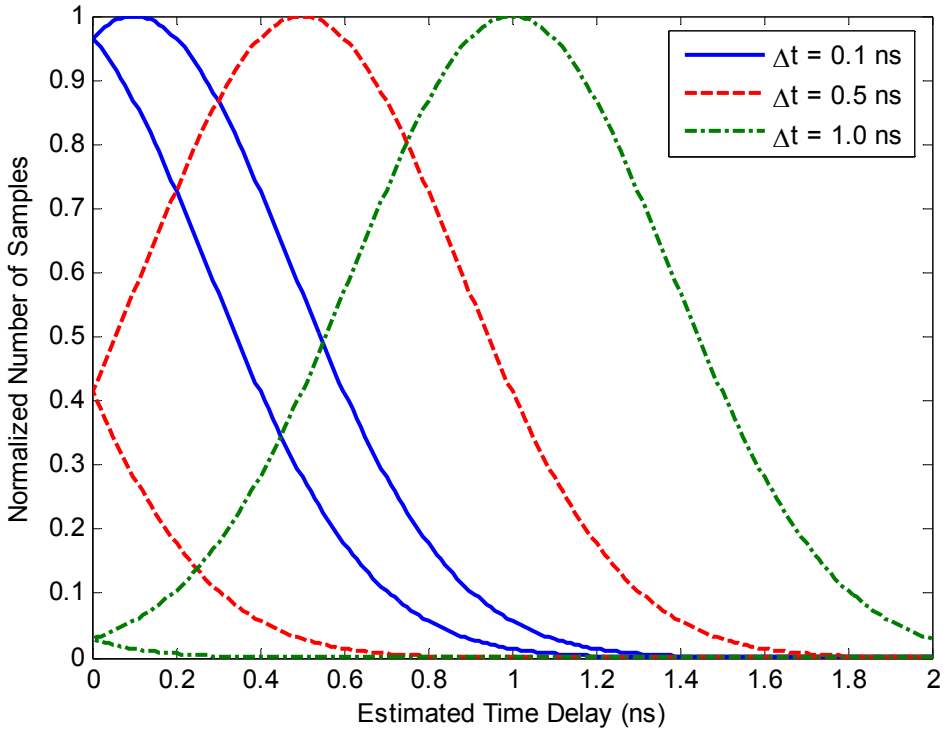

Figure 14.5: Predicted Gaussian distribution of samples used to estimate time delay as a function of the actual delay, using the Gaussian noise of the digitizers.

The delay between channels on the same board is smaller than the lower bound of the delay determination method. This confirms the manufacturer's specification that channels on the same board capture data synchronously. Figure 14.6 contains measured delay between computers for 1000 sample points. The mean measured delay between computers varied based on the calibration (to be discussed in the following section) but was similar to the expectations of 2.1 ns between Pebbles and Dino and 4.6 ns between Pebbles and BamBam.

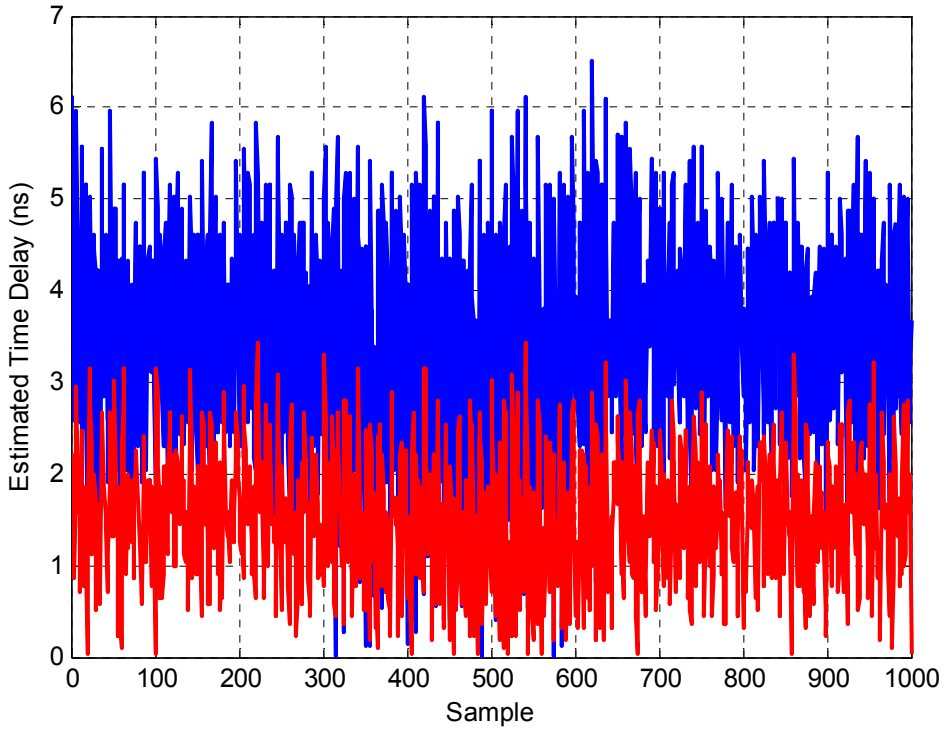

Figure 14.6: Time delay estimated per sample from Pebbles to Dino (red) and to BamBam (Blue).

14.3 Creating a Synchronous Clock and Trigger

The digitizing PCI boards were required to synchronously capture data over a total of twelve channels (four per board). Achieving this synchronization was a major component of this work and was complicated by two factors. First, the digitizers can operate based on an external 80 MHz clock, but do not allow access to their own internal 10 MHz sample clock, which is derived from the external clock. As a result, two boards can have synchronized 80 MHz clocks without having synchronized sample clocks.

The second factor is the determination of the trigger pulse timing. Whereas the sample clock tells the boards when to acquire each sample, the trigger pulse tells the

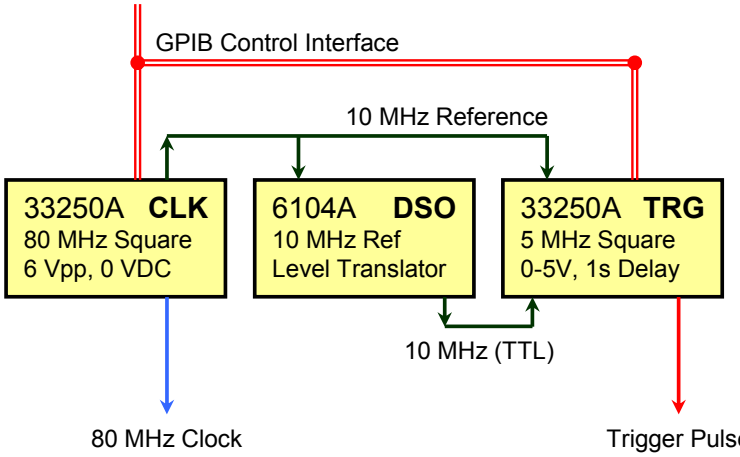

Figure 14.7: The synchronization subsystem consisting of the 80 MHz clock generator (CLK), 5 MHz trigger generator (TRG), and the digital storage oscilloscope (DSO) used to translate the 10 MHz reference to a TTL-compatible signal.

boards when to begin acquiring a collection of many samples. An asynchronous trigger can fire at any time during the sample period. However, initiating a trigger during certain intervals of the capture cycle can cause the boards to sample out of sequence. The probability of a synchronization error was measured at 13% for an asynchronous trigger. The problem is solved by using a synchronous trigger with a programmable timing offset. Because the 10 MHz sample clocks are not accessible off the board, the trigger timing is determined empirically each time the system is calibrated.

Shown in Figure 14.7, the final synchronization subsystem ensures the delay between boards is both small and known and that triggering errors will not occur. The system consists of an 80 MHz clock to operate the digitizers, a 10 MHz reference signal to phase-lock the subsystem components, and a 5 MHz trigger pulse to start a capture sequence with the digitizers. The trigger pulse is synchronous and initiated by a copy of the 10 MHz reference signal.

After initiation, the trigger pulse generator waits for one second, plus a programmable offset, before synthesizing a trigger pulse. The one second delay ensures the computers are all ready for capture before the trigger pulse fires. The programmable offset determines the synchronous trigger timing relative to the 10 MHz reference.

14.4 Calibrating the Digitization System

The digitization system is calibrated each time the system is turned on and after any change affects the synchronization lock between computers. Toggling the external clock, enabling or disabling the external clock input on the digitizers, and reinitializing the digitizers (such as by restarting Matlab) all affect the synchronization lock. Because the calibration process is time consuming, the system may not be altered after it is calibrated.

Calibration entails utilizing the sawtooth measurement system from the previous section and running a calibration program. Because the 10 MHz sample clocks used by the digitizers are not directly accessible, this program executes a brute-force process to synchronize the boards. Toggling the 80 MHz external clock input reinitializes the clock timing of the digitizers. Each time the input is toggled, each digitizer has a 1-in-8 chance of locking the 10 MHz sample clock to any particular cycle of the 80 MHz clock. The inputs are continuously toggled until the digitizers are synchronized, as detected by a measured delay of less than 5 ns.

After the digitizers are synchronized, the calibration program measures the likelihood of a synchronization error as a function of the time delay between the 10 MHz reference and the trigger pulse. The program gathers statistical data for 180 different

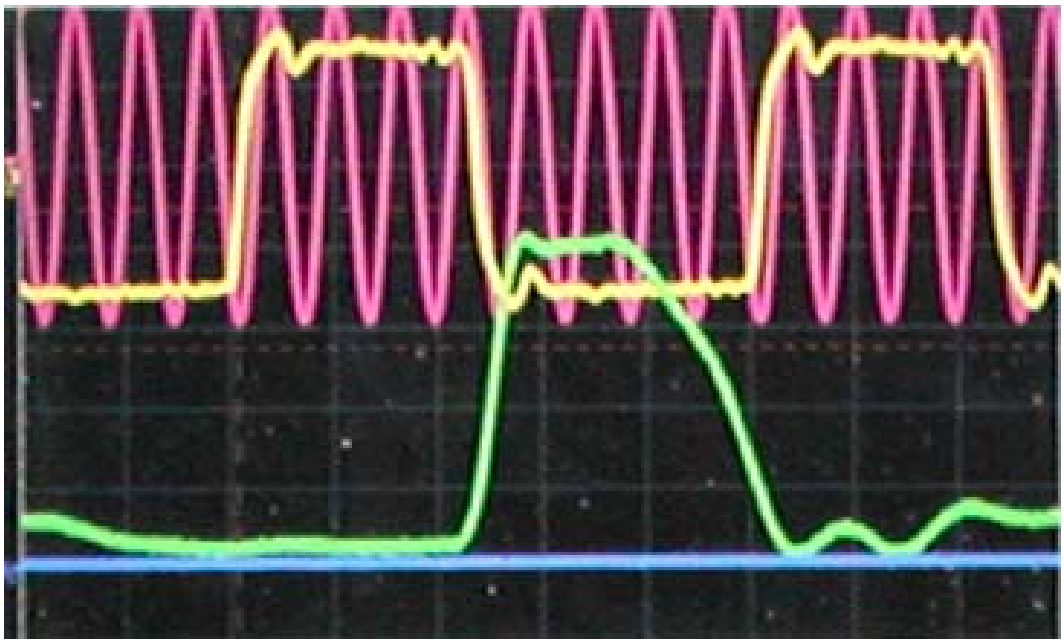

Figure 14.8: Oscilloscope screen capture of the timing signals including the 80 MHz clock (red), 10 MHz reference (yellow), and trigger pulse (green).

time delays between 0 ns and 100 ns and selects a time delay for the synchronous trigger that results in high-reliability data capture. The reliability of a synchronized system is better than 99.9%, as estimated by zero errors in 1000 tests. Figure 14.8 shows an example of calibrated timing of the clock and trigger.

The sample time delay for each channel was corrected in the spectral domain by applying the appropriate Fourier transform identity [71]. The signal x_i' is a time delayed copy of the signal x_i, such that

$$x_i(t) = x_i'(t + \delta_i). \tag{14.3}$$

The signal x_i' is recorded by the digitizer. The corrected (non-delayed) spectrum of x_i, denoted X_i, is obtained by

$$X_i(f) = \exp(+j2\pi\delta_i f) X_i'(f). \qquad (14.4)$$

The corrected spectrum is used in the beamforming process.

In addition to the calibration program, a Matlab-based interface was written to control the system and to autonomously capture and process large amounts of data. A Matlab-based control interface for the digitizers was developed in C++, to supplement the incomplete Matlab-based interface provided by Exacq. A summary of these programs is contained in Appendix B.

Part 5:

Demonstration, Conclusions, and Future Work

CHAPTER 15.
TRACKING THE NASA EARTH ORBITER (EO)-1 SPACECRAFT

15.1 Introduction to the Experiment

The ODIN array (collectively referring to the volumetric array of elemental PLMAs, the JBoard receiver assembly, and the synchronous multi-channel data acquisition system) was used to record the S-band data transmitted by the NASA LEO satellite EO-1. This satellite, described in Chapter 1 of this dissertation, is a sun-synchronous earth environmental satellite. It was selected for use in this research because it has the ability to reduce its S-band data rate from 2 Mbps to 2 Kbps, thus increasing the energy per bit by a factor of 1000, allowing reception with a moderately-sized array. Additionally, established working relationships with the EO-1 mission team, as a result of previous research, enabled efficient coordination of downlink schedules [5].

Because the orbit of EO-1 exhibits both precession and nodal regression, it does not follow the same path through the sky each time it is observed from Atlanta. However, because the orbit is sun-synchronous, when it passes through zenith it does so at 11:23 am (Eastern Daylight Time, or EDT) or 11:23 pm (EDT). Paths through the local sky, or passes, occurring before these times exhibit peaks in the eastern direction; passes that occur after exhibit peaks to the west. On average, six passes (three daytime, three nighttime) every ten days have a peak elevation angle greater than $60°$. Passes with high peak elevations are desired because they are longer and less prone to blockage by buildings near the ground station.

Four low-data-rate (2 Kbps) night-time observations of EO-1 coordinated with NASA were recorded using the ODIN array. These passes occurred on April 29 and 30 of 2006 and May 7 and 9 of 2006. They facilitated demonstration of the functionality of the array, and they aided measurements comparing the beamwidth and noise figure of the array to predicted values. Such measurements were not feasible using a mobile terrestrial transmitter because the far field of the array, given by

$$r_{ff} = \frac{2D^2}{\lambda}, \tag{15.1}$$

exceeds 42m for the ODIN array [11], where D is the longest dimension of the array and is measured as 1.6m. Additionally, the elevation angle in the direction of the transmitter should exceed $El_{\min} = 5°$, and demonstration of the volumetric tracking algorithm required a source that traversed a continuous path in the far field of the antenna over a large arc of the sky.

15.2 The S-Band Downlink of EO-1

In designing the elemental PLMA used in the ODIN array, it was assumed that the source satellite transmits radiation isotropically (or directs its antenna toward the ground station), so that the propagation loss due to distance is the only angularly dependent loss factor exhibited by the communications link. This assumption does not hold for the S-band downlink of EO-1. The S-band transmitter on this satellite utilizes a RHCP antenna oriented toward nadir. The gain of this antenna, relative to an isotropic RHCP radiator, is described by the function

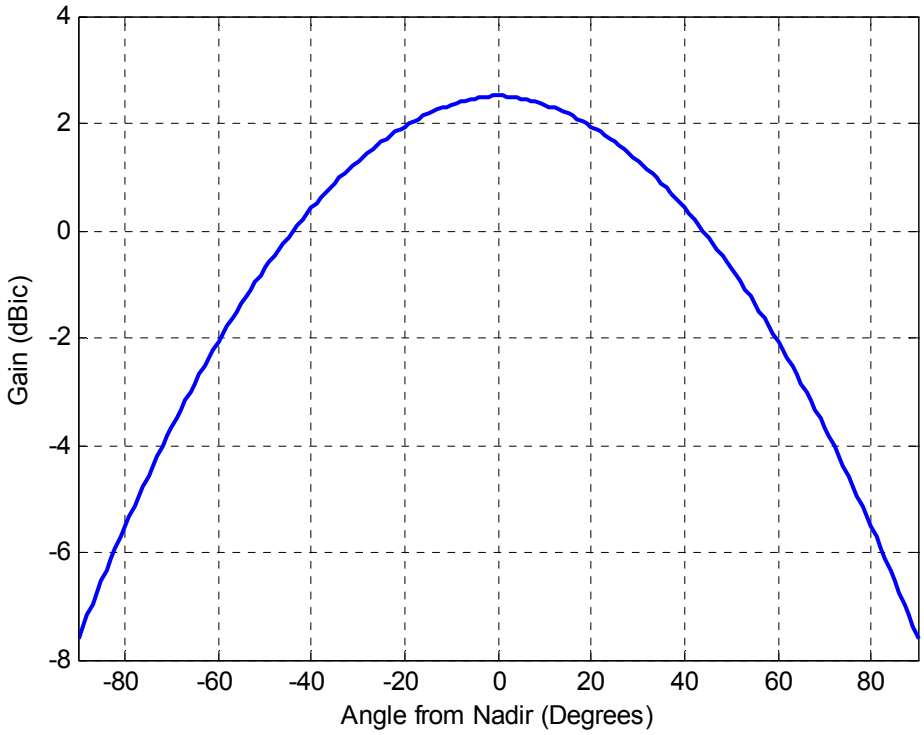

Figure 15.1: Gain of the EO-1 S-band antenna.

$$G(dBic) = -0.0012\theta^2 - 0.0044\theta + 2.5112 \qquad (15.2)$$

where θ is the angle from nadir and is in degrees. This gain is plotted in Figure 15.1.

An angle of $62°$ from nadir corresponds to $El = 5°$ as observed from the ground station; the satellite nadir corresponds to the ground station zenith. The S-band antenna of EO-1 exhibits a 4.5 dB gain variation over this range. As a result, the effective isotropic radiated power (EIRP) of this link is 4.5 dB higher when EO-1 is at zenith than when it is at $5°$ elevation. This variation is observed in the measured signal power.

An alternative to the ground station PLMA was presented in Chapter 6, where the PLMA concepts were applied to an antenna for nadir-oriented satellite use. It is noteworthy that the antenna of EO-1 exhibits the opposite gain-pattern characteristics as

Table 15.1:
S-Band Link Budget between EO-1 and the ODIN Array.

Variable	Value	Note
EIRP	-2.2 dBW	Calculated at $5°$ elevation
Path Distance	2580 km	Calculated at $5°$ elevation
Path Loss	167.8 dB	
Antenna Gain	8 dBi	
Polarization Loss	3 dB	
Implementation Loss	1 dB	
PLMA Noise	290 K	Worst-case estimation
Cable Loss	3 dB	3m of coaxial cable
JENNIE Noise	270 K	Minimum attenuation
Bandwidth	8 KHz	First-null bandwidth
Instantaneous SNR/Channel	-6.9 dB	
Averaged SNR/Channel	3.1 dB	
Averaged Array SNR	10.9 dB	No beamforming error

those desirable in a propagation-loss-matched spacecraft antenna; ideally, the antenna should have a peak gain at $62°$ from nadir, and the gain at nadir should be about 10 dB less than the peak. The difference between the antenna gains $G(62°)$ and $G(\text{nadir})$ of the EO-1 S-band downlink antenna is 14.5 dB less than it should be for an ideal PLMA.

15.3 Link Budget

A link budget for the S-band downlink from EO-1 to the ODIN array is presented in Table 15.1. Two assumptions made in preparing this link budget are that the ground station antenna exhibits an ideal radiation pattern for a parasitic dipole PLMA, and that the EIRP of EO-1 is constant for the duration of the pass. These assumptions make the estimated received SNR independent of the angle of the satellite. As previously mentioned, the radiation pattern of the EO-1 S-band antenna affects the received signal power as a function of angle, and this effect is seen in the measured signal power. Gain

variations in the elemental PLMA, as compared to the ideal PLMA, are too small to be observed in the measured results.

15.4 Observing and Tracking EO-1

15.4.1 Overview of the Passes

The first two low-data-rate passes that were observed occurred on April 29, 2006 (designated P_1, for pass #1), and April 30, 2006 (P_2). For these passes, the array was positioned about 1m from the north-east corner of the fifth-floor structure of the Van Leer roof. No Eccosorb was used in these passes.

A large amount of variation in the received power of the signal from EO-1 was observed during these passes. It was hypothesized that this variation was due to the proximity of the array to the fifth floor structure and reflections from the roof. As a result, the array was moved 7.5 meters from its original position, as far from the fifth-floor structure as possible. Eccosorb, a microwave absorbing foam, was positioned around the base of the array in an effort to reduce reflections from the roof.

Two additional low-data-rate passes were recorded on May 7, 2006 (P_3) and May 9, 2006 (P_4). Signal power variations similar to those observed in the first two passes were also observed for these passes. It is currently thought that these variations are caused by two factors. First, the wooden masts used to position the elemental antennas in the array are thick compared to a wavelength and undoubtedly affect the radiation pattern of the antennas. Unfortunately, the array is too large to simulate this effect with HFSS. The second factor contributing to the received power variations is multipath fading due to

reflections from the roof of the Van Leer building, the outside walls of the fifth-floor offices, and surrounding features on the roof.

The best results were obtained from the analysis of P_3, which had the highest peak elevation of the observed passes. The remainder of this chapter focuses on this pass in particular, but data for all four passes is discussed and included in detail in Appendix C of this dissertation.

15.4.2 Synchronous Data Recording and the Data Structure

The synchronous digitization system was configured to record the raw data from the JENNIE receivers to the local hard drive of each computer for the duration of each pass. This is in contrast to another mode of operation of the digitization system, in which calibrated data is returned to the master computer immediately following each capture cycle. Saving data to the local hard drive of each computer and relegating the data calibration to post-processing greatly increased the rate with which data could be captured by reducing network and processing requirements. About nineteen gigabytes of raw data was collected for a fifteen minute pass. This data took several hours to process and calibrate.

Data was recorded in 0.1-second snapshots, each of which each contained 1 mega-complex-sample (1 MCS) per elemental antenna. The time between successive snapshots was approximately 4.5 seconds, including set-up time (initializing each computer and waiting for the trigger), record time (capturing data and transferring it to local memory), and saving data to the local hard disk.

As previously discussed regarding the link budget for these experiments, the expected signal-to-noise-ratio at the output of the receivers is -6.9 dB, meaning the power

of the noise was about 5 times the power of the signal. This figure was improved at the expense of spectral resolution by averaging the contents of the data snapshots. Each snapshot is subdivided into 100 frames containing 10 kilo-complex-samples (KCS) per elemental antenna. The spectral resolution of an individual frame is 1 KHz. Averaging the spectra of 100 frames yields a 10 dB improvement in the SNR of the received signal as opposed to an individual frame alone. As shown in the link budget, this averaging improves the predicted SNR of a single channel from -6.9 dB to +3.1 dB at $El_{\min}$, or +7.6 dB at zenith.

This averaging process and the organization of the data structure are shown in Figure 15.2. Data processing also included detection of the Doppler shift of the signal and implementation of a beamformer, both of which are shown in Figure 15.2 and are discussed in the following sections.

15.5 Observation Summary

15.5.1 Received Power and Scattering

The measured power at the output port of each antenna was evaluated for each snapshot in the data set for each pass. Due to structure scattering and multipath fading, this power exhibits a rapid oscillation as a function of time. Figure 15.3 contains plots of the signal to noise ratio as a function of time for P_3, indicating the minimum signal power and maximum signal power exhibited among the six antennas. The power oscillations are caused by two factors. First, the wooden array structure and the presense of other antennas alter the radiation pattern of each antenna within the array. Second,

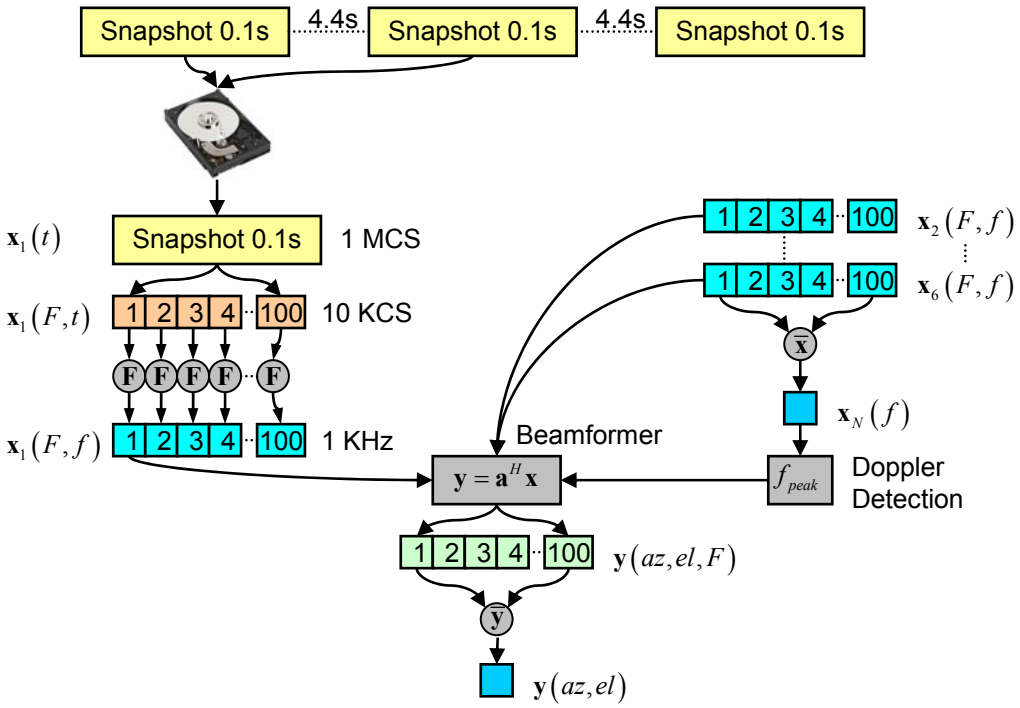

Figure 15.2: Data structure and processing for the ODIN array. Snapshots are streamed to the hard drives and processed after each pass. The outputs for each snapshot include the peak frequency and beamformer output.

large structures on the roof (including the roof itself) reflect the incoming signal, causing multipath fading. It was not possible to measure the relative strength of these factors.

Despite the gain variations, the recorded data can be compared to the signal strength predicted by the link budget. For example, the SNR predicted by the link budget for a satellite elevation of 5° is 3.1 dB. This is similar to the maximum observed SNR near the end of the pass (700 seconds, as indicated in Figure 15.3). The envelope of the maximum SNR for the second half of the pass, as defined by a line connecting the peaks of the received SNR, exhibits an increase of more than 4 dB as EO-1 nears zenith. This agrees with the predicted value based on the radiation pattern of the antenna on EO-1.

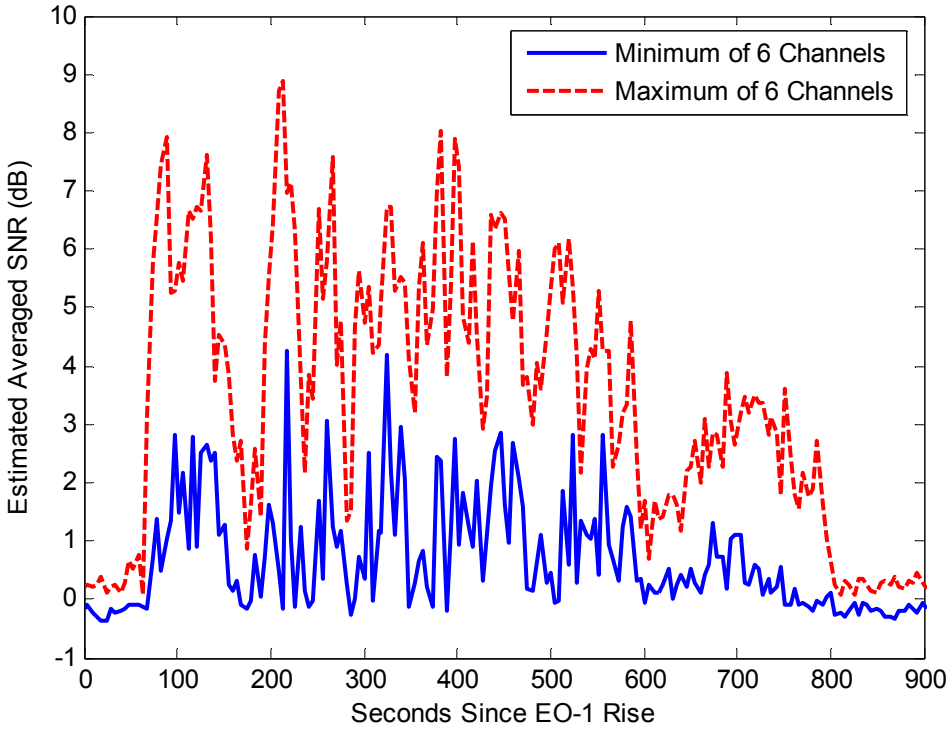

Figure 15.3: Averaged SNR of the antenna channels for pass #3.

The first half of the pass does not exhibit the same SNR envelope structure as the second half of the pass, and the received peak SNR exceeds the predicted value. This might be caused by constructive multipath interference due to the structures surrounding the array. The configuration of the array on the roof of the Van Leer building is shown in Figure 15.4; this configuration was used for P_3 and P_4. For the first half of the pass, the satellite is south of the array, and the large surface area of the roof and eastern wall of the fifth-floor structure provide a strong opportunity for multipath fading. For the second half of the pass, the satellite is north of the ground station and fewer large reflecting surfaces are available.

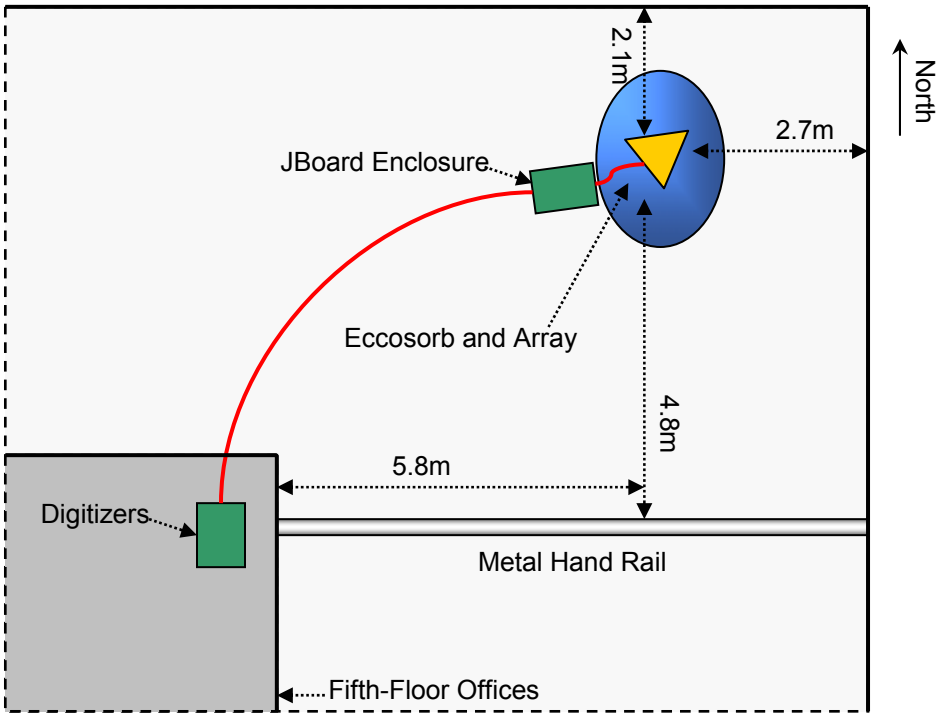

Figure 15.4: Diagram of the array on the roof of the Van Leer building. The array is positioned near the north-east corner of the building.

15.5.2 Doppler Profile

Each frame of recorded data from the passes contained ten thousand complex-samples per-antenna. After FFT processing, these samples provide the spectra of the antenna outputs with a resolution of 1 KHz. The beamformer used to determine the direction of the satellite combines the antenna outputs for each frequency independently and averages the resulting radiation pattern over 100 frames. Because of the time required to perform this task, it is necessary to limit the number of frequencies that are processed. For a slowly moving target, solely the frequency of the carrier would be selected for processing and remaining spectral data would be discarded.

For a satellite such as EO-1, the velocity of the orbit, and thus the speed of the satellite relative to the ground station, causes a large Doppler shift in the frequency of the

received downlink signal as opposed to its original frequency. The Doppler shift is calculated by

$$\Delta f = \frac{V_T}{c} f_T , \qquad (15.3)$$

where V_T is the component of the satellite velocity in the direction of the ground station, c is the speed of light, and f_T is the frequency of the transmitted signal [8].

No Doppler shift is observed when the direction of motion of the satellite is tangential to the direction of the ground station. This occurs at the peak observed elevation angle of the satellite, so determining the point where there is no Doppler shift is equivalent to determining the point of maximum elevation of the satellite. The maximum Doppler shift occurs when the satellite is near the horizon. For EO-1, the maximum Doppler shift is about 51.6 KHz. This is much larger than the bandwidth of the low-data-rate downlink signal, so it is necessary to determine the Doppler shift of the signal prior to beamforming.

The algorithm estimates the peak frequency of the signal by identifying the frequency of each antenna output that exhibits the peak intensity. Because the channels fade with time, the algorithm selects the antenna with the highest detected power as the source for this detection during any particular snapshot.

The S-band downlink of EO-1 has two methods for selecting a transmitting frequency. In the first method, used for this experiment, the satellite uses an on-board oscillator to generate the 2270.4 MHz carrier frequency. This reference is subject to drift with temperature and age. In the second method, the satellite receives a signal from a

ground station and generates the downlink carrier frequency as an exact multiple of the uplink frequency.

Because the carrier used in this experiment was subject to drift from the specified frequency, the processing algorithm estimated (and corrected for) this drift by estimating the carrier frequency by

$$f_c = \frac{f_{\max} + f_{\min}}{2}. \qquad (15.4)$$

The EO-1 carrier frequency was estimated from the measured data as +6 KHz from 2270.4 MHz. This is within the drift limits of 3 ppm listed for the on-board transponder frequency generator [7], but measurements provided by NASA show a mean offset of less than 500 Hz for the on-board transponder [72].

An error in the observed frequency can be caused by an error in the oscillators used in the receiver. Testing with a Hewlett-Packard 8564-E spectrum analyzer indicated that the HP-8656 oscillator overstated its output frequency by 2.6 KHz, which caused the EO-1 signal to appear 2.6 KHz higher in frequency than the actual value. The HP-83712B appears to overstate its output frequency by 1.4 KHz. No drift was detected for the sources used to operate the digitizers.

These measurements account for most of the observed drift of the carrier of EO-1 in excess of the data reported by NASA, and reduce the observed drift to +2 KHz. However, the accuracy of these measurements is limited by the frequency accuracy of the spectrum analyzer, which was calculated as ±3.2 KHz for the HP-8656 measurement and ±4.2 KHz for the HP-83712B measurement [73]. It is noted that these measurements

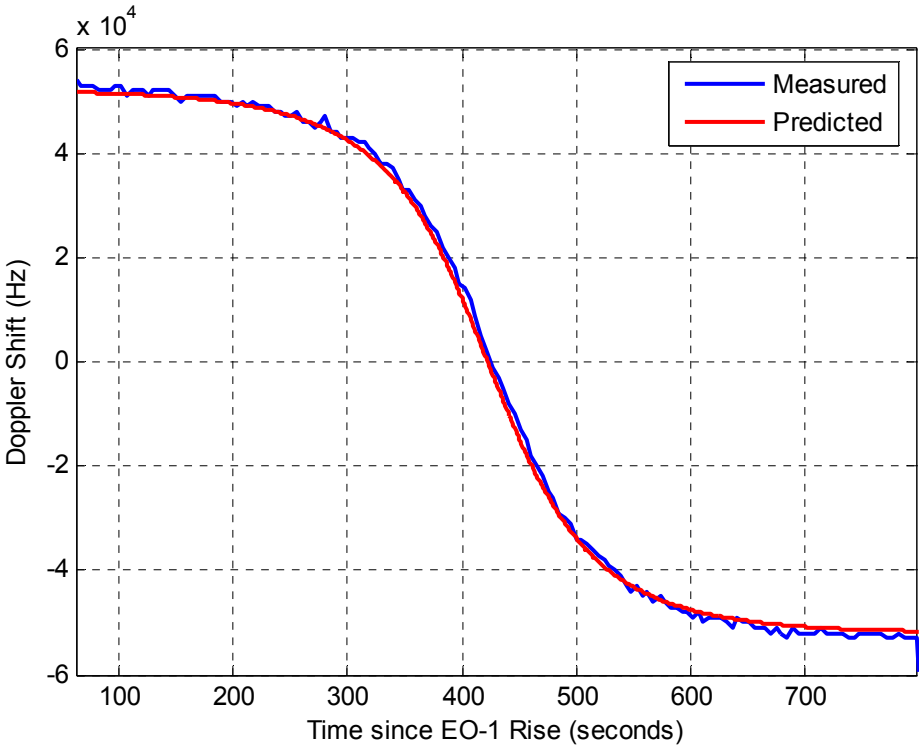

Figure 15.5: Measured and predicted Doppler shift versus time for EO-1 pass #3 (P_3).

were repeated on a second spectrum analyzer (Agilent E4407B) and were consistent (within 50 Hz) of these measurements.

The calculated Doppler shift as a function of time for P_3 is compared to the predicted value in Figure 15.5, relative to the calculated carrier frequency. The observed Doppler shift almost perfectly matches the predicted Doppler shift. The maximum error is less than 2 KHz, only a quarter of the bandwidth of the signal, and can be attributed to noise or fluctuations in the spectrum of the data, since the Doppler detection algorithm used the frequency that contained the maximum power, rather than the calculated center of the signal.

15.5.3 Beam Pattern

The array processing subsystem implements beamforming with a conventional beamformer given by

$$\mathbf{y}_{\phi,\theta} = \mathbf{a}_{\phi,\theta}^{H}\mathbf{x}, \tag{15.5}$$

which was discussed in Chapter 10. The beamformer outputs are computed for azimuth and elevation in increments of $0.5°$ for each frame of complex data at the peak frequency detected by the Doppler detection algorithm. The magnitudes of the beamformer outputs of the 100 frames within an individual snapshot are averaged to improve the SNR of the final beamformer output by 10 dB, as in

$$\mathbf{y}'_{\phi,\theta} = \frac{1}{100}\sum_{F=1}^{100}\left|\mathbf{y}_{\phi,\theta}(F)\right|, \tag{15.6}$$

where F indicates the frame number.

Figure 15.6 contains the averaged beamformer output at an arbitrary time for P_3. This is similar to the beamformer output shown for the volumetric array in Figure 10.3. The x-axis indicates the bearing relative to the axis of the array, rather than azimuth. This plot illustrates the necessity for the volumetric array tracking algorithm. The large aperture size of the array allows a very low beamwidth over a wide range of scan angles using only 6 antennas, but dozens of grating lobes and strong sidelobes obscure the position of the satellite.

15.5.4 Beam Width

The 3 dB beamwidth of the ODIN array is estimated from the output of the beamformer. The estimated value is $4°$ in both azimuth and elevation. The resolution is

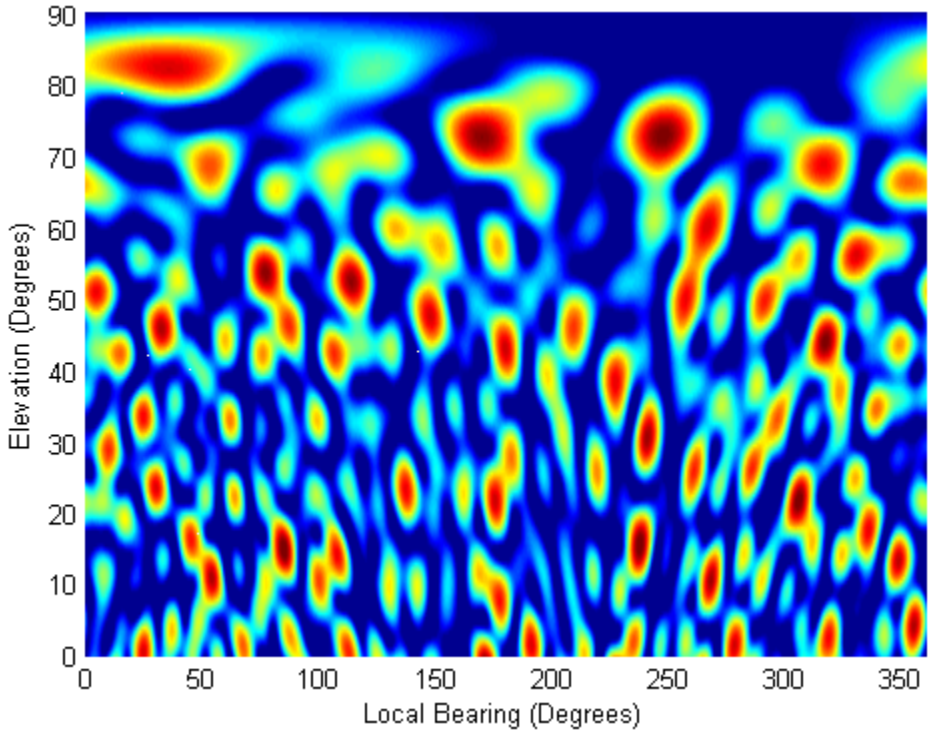

Figure 15.6: Beamformer output for P_3, snapshot 50. EO-1 is located at 177° bearing, 8° elevation. Color indicates SNR from 0 dB to 8.5 dB.

uniform over the entire hemisphere of the sky, as a result of the volumetric design of this array. Equation (10.2) predicts a 3 dB beamwidth of 4.15° for an array of 6 elemental antennas spanning an aperture of 5λ, and is similar to the observation.

15.6 Tracking

After the beamformer outputs were generated for each snapshot of a pass, the processing software implemented the tracking algorithm described in Chapter 10. The three types of track metrics described in Chapter 10 were combined to create one metric for each path detected by the algorithm. The first of these is s_ℓ, the integrated length of

the path, as in Equation (10.11). The second is s_{12}, the end to end length of the path, as in Equation (10.12). The third is s_t, the lifetime of the path, as in Equation (10.13).

The combined metric for each path is defined by the integrated arc length subject to three conditions. First, the starting and ending points of the arc must span an angle greater than $20°$. Second, the arc must exist for more than 10 snapshots (45 seconds). Finally, the estimated SNR of the received signal must be at least 1 dB at the starting time of the arc. Mathematically, this metric is given by

$$s = s_\ell \left| \left(s_{12} > 20°\right) \cap \left(s_t > 45\text{s}\right) \cap \left(SNR_1 > 1\,\text{dB}\right). \qquad (15.7)$$

This algorithm automatically selects the track corresponding to the highest evaluated value for the metric, and assigns that track as the most likely path of the satellite.

This algorithm was applied to the data for all four passes and allowed to track up to 300 peaks per snapshot. Although the true location of the satellite usually occurred in the top 20 peaks, using a large number of peaks helped to stabilize the algorithm. During several snapshots, more than 100 lobes exceeded the power of the lobe containing the satellite. Additionally, the satellite location was manifested in weaker peaks near AOS and LOS, so tracking more peaks simultaneously helped extend the tracking range.

Despite the multipath fading in the recorded signals and concerns that this fading would adversely affect the phase of the received signal (and thus the array manifold used to determine the beamformer steering vectors), the tracking algorithm yields accurate estimates of the satellite path for three of the four passes. For the fourth, P_2, the satellite was obstructed by buildings for much of the pass, and the algorithm lacked a sufficient length arc to identify the path of the satellite.

The paths from the output of the tracking algorithm for all four passes are compared to the actual path predicted by orbital models for EO-1 in Figures 15.7 through 15.10. These paths are a final demonstration of the functionality of the ODIN array: the path of EO-1 was autonomously and accurately determined by the array system. The PLMA compensated for the angularly dependant propagation loss exhibited by the communications link, enabling data capture over the entire sky while minimizing the number of required antennas. The new algorithm for target tracking with volumetric arrays enabled the system to determine the true path of EO-1 among hundreds of aliased tracks, which corresponded to dozens of aliases at any instant in time.

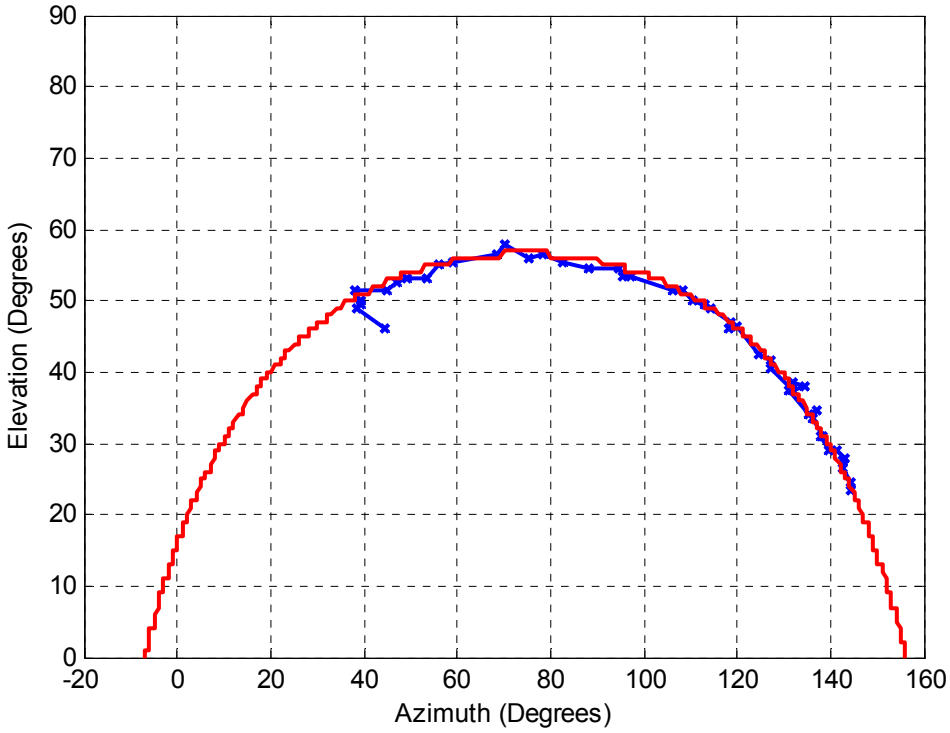

Figure 15.7: Observed track of EO-1 (Blue) and the predicted track (red) for pass #1 (4/29/2006). The observed track is obtained using the volumetric tracking algorithm, and is within a few degrees of the predicted track. Only a partial track was obtained for this pass.

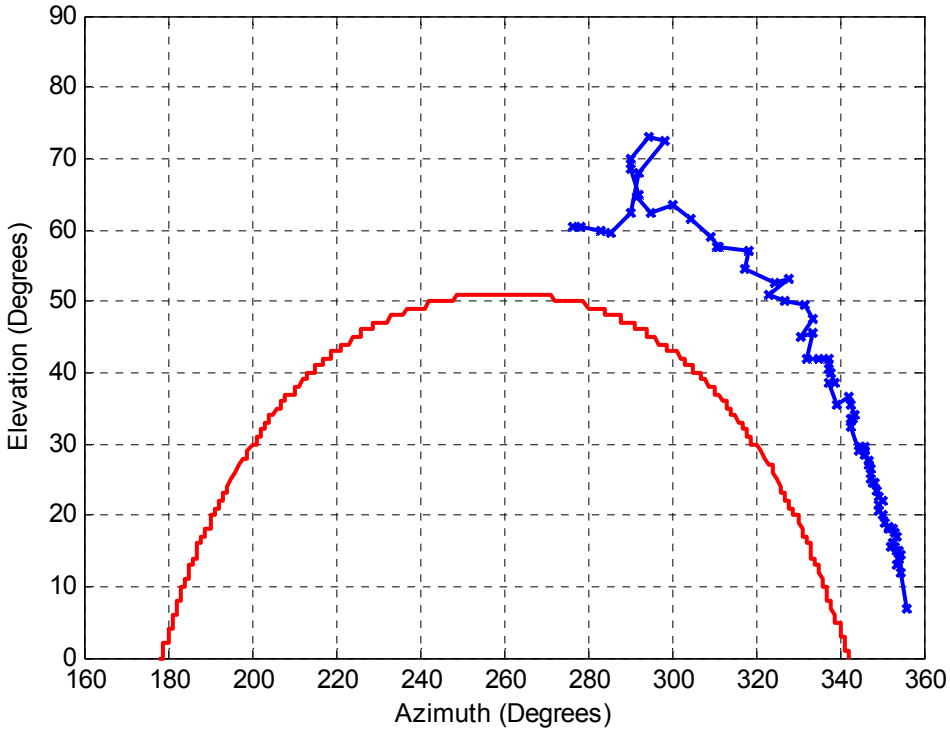

Figure 15.8: Observed track of EO-1 (Blue) and the predicted track (red) for pass #2 (4/30/2006). The observed track is obtained using the volumetric tracking algorithm. The signal was blocked for the first half of the pass due to nearby buildings. The observed track is short, and differs significantly from the predicted track. This difference could have been caused by phase errors due to multipath scattering or by the algorithm locking to an alias rather than the proper track.

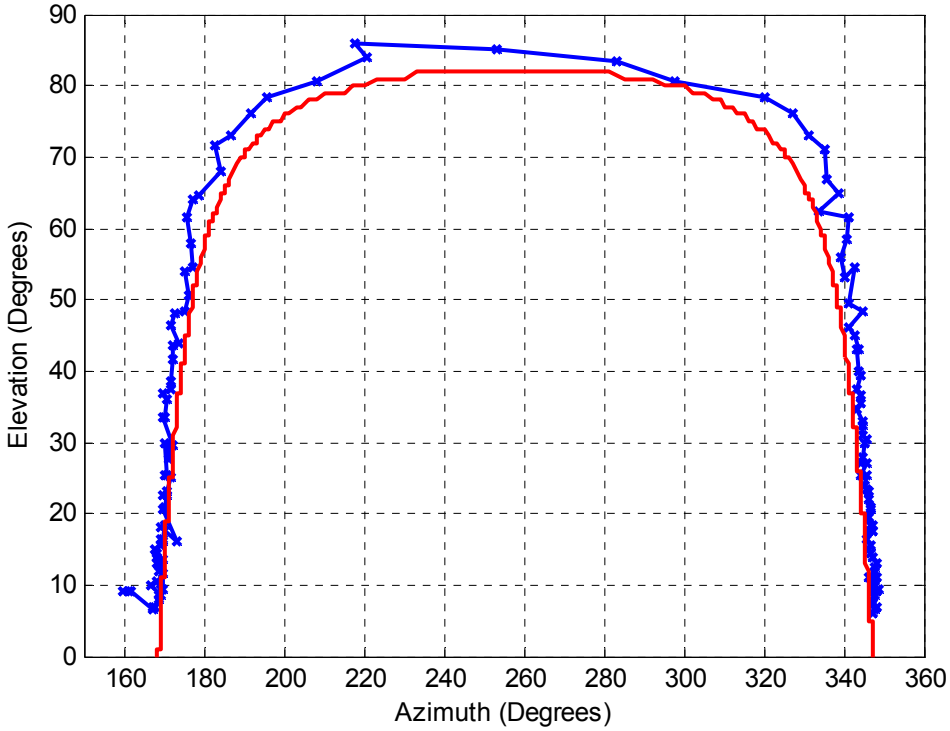

Figure 15.9: Observed track of EO-1 (Blue) and the predicted track (red) for pass #3 (5/7/2006). The observed track is obtained using the volumetric tracking algorithm, and is within a few degrees of the predicted track.

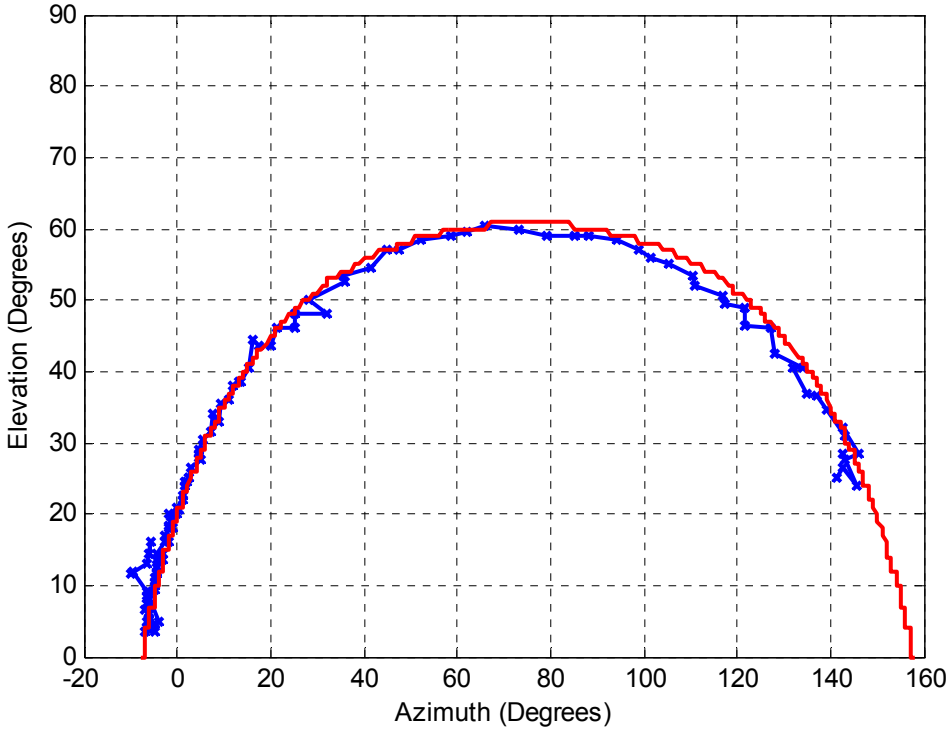

Figure 15.10: Observed track of EO-1 (Blue) and the predicted track (red) for pass #4 (5/9/2006). The observed track is obtained using the volumetric tracking algorithm, and is within a few degrees of the predicted track.

CHAPTER 16.
CONCLUSIONS, SUMMARY, AND FUTURE WORK

16.1 Conclusions of the Research

A totally electronically-steered demonstration array designed for horizon-to-horizon communication with LEO satellites was successfully demonstrated. This array is the first of its kind; as of this writing, no similar arrays have been reported. Despite the multipath and structure-scattering variations in signal power received by the ODIN array, this volumetric array successfully tracked the NASA satellite EO-1. The beneficial effect of the PLMA element was demonstrated; it was shown that this antenna compensates for the angularly dependent propagation loss of the communications link. Although this demonstration array did not contain a sufficient number of elements to utilize a genetic optimization algorithm for reduction of grating lobes, the volumetric tracking algorithm was successfully implemented. Despite dozens of grating lobes in the radiation pattern of the array, it was shown for three passes that the algorithm autonomously predicted the correct path (or section of the path) for the satellite.

Arrays for LEO satellite communications will benefit from the use of a wide-beam PLMA. However, this study demonstrated the importance of multipath fading in a phased array consisting of such antennas, even though LEO satellite communication links are line-of-sight and the ground station is in an open (e.g. rooftop) environment. Depending on the deployment scenario, reflections from objects many wavelengths from the array might dominate the multipath fading. This was discussed in the previous chapter for the case when EO-1 was south of the ODIN array. On the other hand, as

shown for the case when EO-1 was north of the ODIN array, and there were few opportunities for such reflections, the supporting structure of the array itself will scatter the received (or transmitted) radiation, causing the elements of the array to exhibit amplitude and phase variations from the predicted response. Because these variations are independent for each element, accurate calibration of the array will be a complex process for arrays consisting of a large number of elements.

While methods of adaptively combining the outputs of the ground station antennas can mitigate the effects of multipath [5], an effective alternative approach might include using a propagation loss matched antenna as the omnidirectional antenna (or as an elemental antenna in a phased array with a small number of elements) on board the satellite. One possible design for such an antenna was shown in Chapter 6. Alternatively, the elemental antennas can be designed to account for the presence of other elemental antennas in the array as well as the structure of the array, as discussed in Chapter 7, but multipath fading will still be present. A final option for achieving the benefits of a propagation loss matched antenna in a ground station while avoiding multipath is to apply the PLMA synthesis algorithm to scan-loss synthesis using a ground station consisting of fixed high-gain electronically steered antennas. This was presented in [74], and a portion of that work is contained in Appendix D.

This dissertation proceeded on the assumption that the LEO satellites under consideration will communicate directly with the ground network (GN). This might be necessary to supplement the capacity of the second-generation TDRSS as the number of high-bandwidth LEO satellites increases, and potentially exceeds the number of high-bandwidth links available from TDRSS. LEO satellites operating high-bandwidth links

at X-band (8.0-8.4 GHz), such as EO-1, will continue to communicate directly with the GN, because TDRSS only provides service in S-band and K-band.

However, TDRSS-related antennas on board a LEO satellite can benefit from the design optimizations in this research. The variation of E_B/N_0 due to angle of a TDRSS link is much smaller than that for a LEO satellite with a ground station, less than 2 dB. However, as was shown for the example of the NASA satellite EO-1 in Figure 15.1, the S-band RHCP omni is not "omnidirecitonal" at all; the design methods in Chapter 6 could be used to create a true omni antenna with RCHP designed for the link between TDRSS and a LEO satellite. Improving the TDRSS-link antennas on the LEO satellite will lessen the required transmitting power while allowing the same data rate, potentially greatly reducing the cost of the satellite, since the power requirements of a communications satellite are a primary factor in determining the cost of the satellite.

16.2 Summary of Original Work Completed

16.2.1 Genetic Optimized Antennas

- Developed a propagation loss matched antenna architecture for LEO satellite communications and conducted an exhaustive study to determine the requirements and design limitations of this antenna.
- Constructed and characterized eleven propagation loss matched antennas (three prototype, eight for the ODIN array).
- Developed a circularly polarized propagation loss matched antenna architecture suitable for use on board a satellite. Conducted a study to demonstrate the capacity of this architecture to meet the design requirements.

16.2.2 Volumetric Phased Arrays

- Developed and demonstrated a pattern-space analysis method for volumetric arrays (UVW-space).
- Developed, coded, and tested a method of identifying a moving target among many aliases when implementing direction finding using volumetric arrays.

16.2.3 FFT Beamforming with Thinned Arrays

- Developed an algorithm for applying efficient FFT beamforming with interference projection to aperiodic phased arrays.
- Developed, coded, and tested an optimization model for synthesizing the layout of aperiodic arrays for use with this algorithm.

16.2.4 Phased Array Testbed

- Designed, built, and tested a broadband RF-receiver with low noise, good intermodulation performance, high dynamic range, and computer-aided calibration.
- Designed and integrated a high-bandwidth multichannel synchronous digitization subsystem with very high reliability and calibrated timing offsets between channels.
- Designed, coded, and implemented a Matlab-based interface for control of the RF and digitization subsystem.

16.2.5 Phased Array for tracking LEO Satellites

- Designed, integrated, and tested a phased array system consisting of six independent channels, each of which includes an antenna, receiver, and digitizer.

- Demonstrated tracking of the NASA satellite EO-1 with this array during four passes observed from Atlanta. More than 73 GB of data was generated during these passes and processed to predict the path of the satellite.

16.3 Publications and Presentations

This work resulted in three conference presentations and preparation of four articles intended for publication in peer-reviewed journals.

16.3.1 Publications

W.C. Barott and P.G. Steffes, "FFT Beamforming with projection nulling for thinned array geometries," IEEE Transactions on Antennas and Propagation (in revision).

W.C. Barott and P.G. Steffes, "A Genetic wire antenna for LEO satellite communications," IEEE Transactions on Antennas and Propagation (in revision).

W.C. Barott and P.G. Steffes, "Optimization of volumetric phased arrays with genetic algorithms," for IEEE Antennas and Wireless Propagation Letters (in revision).

W.C. Barott and P.G. Steffes, "A Parasitic synthesized beam genetic wire antenna using multiple feeds in a thinned array configuration," for IEEE Antennas and Wireless Propagation Letters (in preparation).

16.3.2 Presentations

W.C. Barott and P.G. Steffes, "A Parasitic synthesized beam genetic wire antenna using multiple feeds in a thinned array configuration," to be presented at the 2006 IEEE APS/URSI Int'l Symposium, Albuquerque, NM, July 10-14.

W.C. Barott and P.G. Steffes, "Using genetic algorithms to remove grating lobes from the patterns of various thinned linear arrays," presented at the 2005 IEEE APS/URSI Int'l Symposium, Washington, DC, July 3-8.

W.C. Barott and P.G. Steffes, "Antenna and topology choices for a large N array for LEO satellite downlink," International Union of Radio Science (URSI) Programs and Abstracts: 2005 National Radio Science Meeting, Boulder, CO, Jan. 5-8 2005, p 59.

16.3.3 Intellectual Property

W.C. Barott and P.G. Steffes, "A method of radio direction finding using a volumetric phased array to differentiate aliases," in preparation.

W.C. Barott and P.G. Steffes, "Optimized multi-feed antenna for satellite communications," in preparation.

W.C. Barott and P.G. Steffes, "Synthesized pattern antenna with circular polarization for satellite communications," in preparation.

W.C. Barott and P.G. Steffes, "Fast Fourier transform beamforming for an array of aperiodic antennas," in preparation.

W.C. Barott and P. G. Steffes, "Propagation loss matched antenna for satellite communications," provisional patent filed September, 2004. Renewed September, 2005.

W.C. Barott and P.G. Steffes, "Platonic solid phased array antennas," provisional patent filed September, 2004.

16.4 Future work

Much work remains to fully explore the research areas presented in this dissertation. These areas are listed below, along with a summary of research that will be conduced in the future.

16.4.1 Genetic Algorithms with Self-Adaptive Resolution

Interesting work has been presented regarding self-adaptive genetic algorithms [19]. These algorithms offer a faster convergence rate than genetic algorithms that use fixed parameters (eg, mutation rate and population size) throughout the optimization process. No published work exists on the topic of a self-adaptive GA that adaptively controls the resolution of the algorithm, where the resolution is defined as the number of bits allocated to a gene. It is hypothesized that such a modification would significantly improve the convergence rate of the algorithm.

16.4.2 Genetic Antennas

The spacecraft PLMA discussed in Chapter 6 offers practical advantages over the omnidirectional antennas currently used in LEO satellites both because of the beneficial pattern and because of improved polarization integrity. This design architecture presents one major difficulty, which accounts for the lack of published research on such a helical architecture: this antenna will be very difficult to construct. Methods for simplifying the architecture to ease the construction process will be investigated. Additionally, research will seek automated methods of accurately constructing arbitrary genetic antennas.

The multi-feed antenna discussed in Chapter 7 will be investigated in more detail and this antenna architecture will be built and demonstrated. This antenna is beneficial to

many applications where many feeds must be placed near each other, and each feed must have a radiation pattern that is synthesized to fit the requirements of the application.

16.4.3 Volumetric and FFT Optimized Arrays

A volumetric array was demonstrated in this research but the low number of antenna elements prohibited the application of optimization algorithms to the array topology. In future work, optimized volumetric arrays consisting of a large number of antenna elements will be demonstrated to facilitate the development of the optimization and tracking algorithms.

Additionally, the reduced Fourier-space projection method discussed in Chapter 11 has yet to be demonstrated with a physical array. Optimizing and demonstrating such an array are subjects of future work.

16.4.4 High Speed Phased Array Radio Testbed

The JENNIE receiver boards were indispensable in completing this research, but many improvements are possible in a future revision to improve the quality and ease of assembly. Additionally, it is desired to construct a digitizing array radio test-bed for continuing experiments. The cost of the 40 MS/s digitizers is not high by the standards of capital equipment (approximately $1800 per digitizer and computer for up to four channels at 10 MS/s each), but reducing this cost would enable deployment of many channels.

Eventually, a custom software-defined-radio test-bed will be constructed for capturing and processing synchronous data. The peripheral component interface (PCI) bus of a computer currently limits the speed at which a computer-based test-bed can

record data. The Exacq Technologies CH3160 boards can stream 80 MB/s from the digitizers to the computer, representing 40 MS/s, but this is near the limit of the PCI bus. Some PCI digitizers are capable of recording data at much faster rates, but must buffer the data on-board the card for transfer to the computer. The custom test-bed will implement high speed synchronous data capture up to 100 MS/s or 1 GS/s per channel, and will include FPGA microchips to facilitate data processing and direct transfer to large hard drives. It is noted that the SATA 3 Gb/s standard allows data rates of up to 300 MB/s to hard drives, and this rate is expected to increase in the coming years.

APPENDIX A.
MEASUREMENTS OF THE ELEMENTAL ANTENNAS

The radiation patterns and impedances of the eight antennas that were constructed for the ODIN array were measured on July 20, 2005. This data was later processed to determine the pattern patch as a function of frequency, $\Delta P_{\max}(f)$. The impedance of these antennas meets expectations; S_{11} is about -20 dB within 50 MHz of the feed resonance at 2.2 GHz, and about -10 dB elsewhere. This data is shown in Figure A.1. It is noted that this is S_{11}, the reflected power, rather than the calculated S_{12}, or radiated power, as was used in Chapter 5.

It is believed that one of the feed cables was damaged during the measurement process or that the conditions of the feed cables changed. The cable loss as a function of frequency, taken after this series of measurements, is shown in Figure A.2. No data on the cables was taken prior to the execution of the measurements. The feature at 2.25 GHz indicates an impedance mismatch somewhere in the cable assembly. Calculated plots of $\Delta P_{\max}(f)$ for each antenna are shown in Figure A.3.

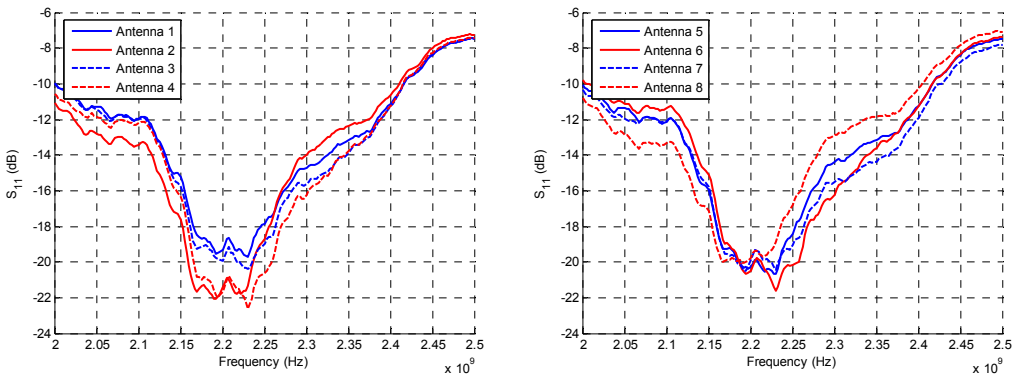

Figure A.1: Measured return loss of the ODIN antennas.

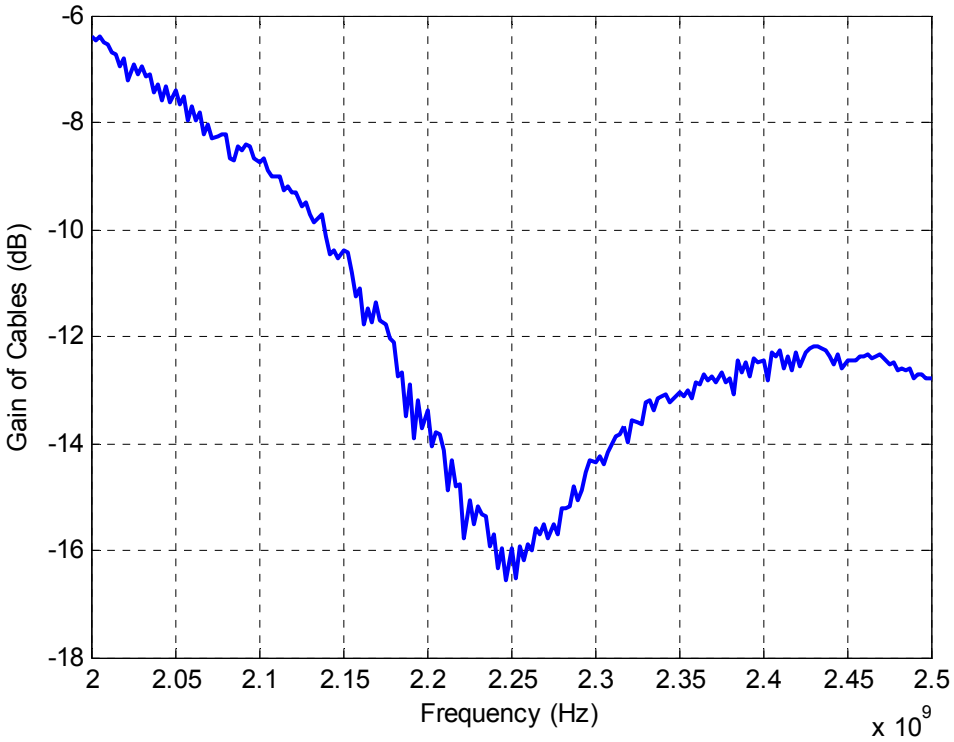

Figure A.2: Cascaded loss of the cables in the measurement system, measured after finishing the radiation pattern measurements.

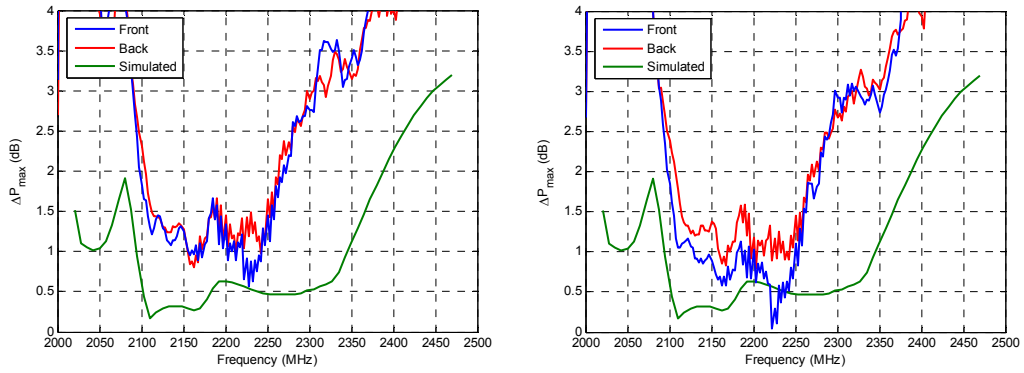

Antenna #1

Antenna #2

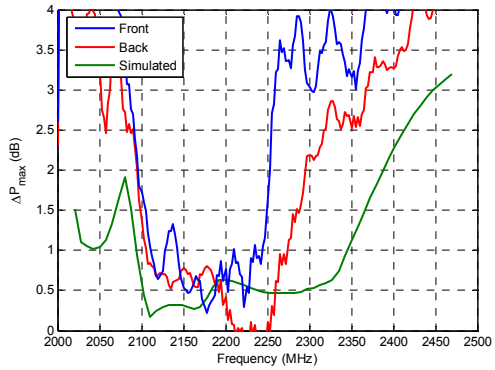

Antenna #3

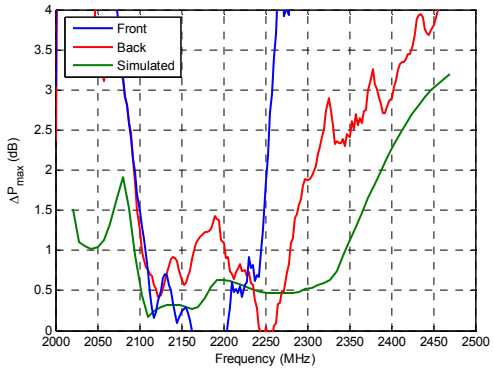

Antenna #4

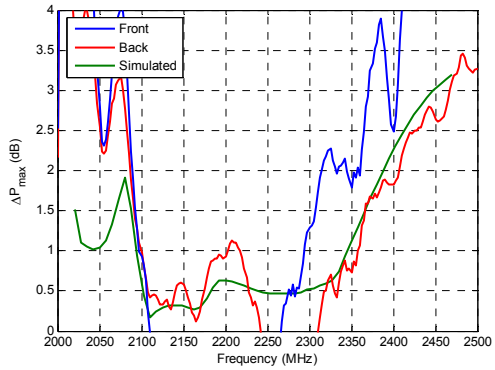

Antenna #5

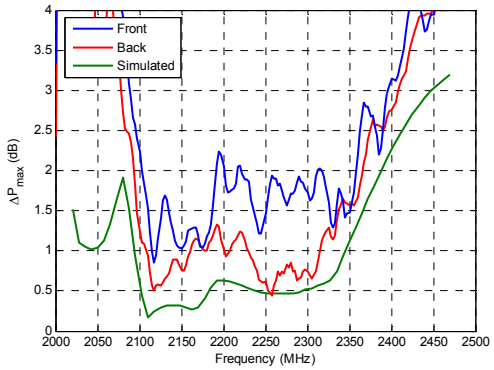

Antenna #6

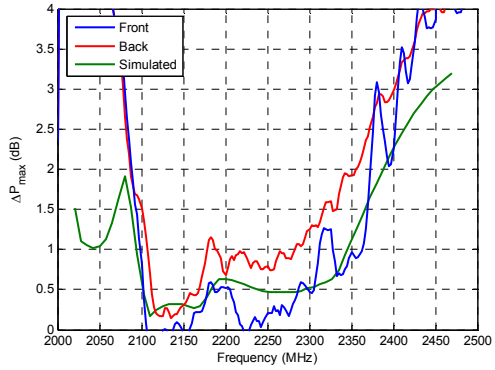

Antenna #7

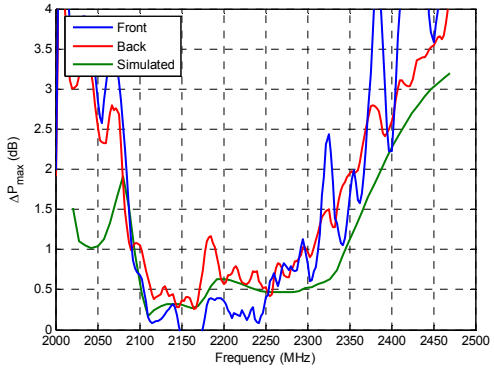

Antenna #8

Figure A.3: Measured pattern match for the ODIN antennas.

A S-band standard gain horn was used as the reference antenna for these measurements. This is a Narda Microline model 644. This antenna is intended for operation above 2.6 GHz. Operation at the frequencies of these measurements required extrapolating the gain curve of this horn and correcting for the impedance mismatch at the lower frequencies. The estimated gain was calculated based on the gain of an aperture antenna [8]

$$G = \eta_i \frac{4\pi A}{\lambda^2} \qquad \text{(A.1)}$$

where the aperture efficiency η_i is 75% (based on the manufacturer-supplied calibration of the horn) and the area of the aperture is $A = 0.0392\,\mathrm{m}^2$. The calculated gain is shown in Figure A.4.

It is assumed in the calculation of the gain that the antenna is perfectly matched to a transmission line. This antenna is poorly impedance-matched below 2.4 GHz. The reflection loss was measured using a network analyzer, and the S-parameters of reflection and radiation were calculated and are shown in Figure A.5. Both of these plots should be used when conducting measurements using this horn in the 2.0 to 2.5 GHz frequency range.

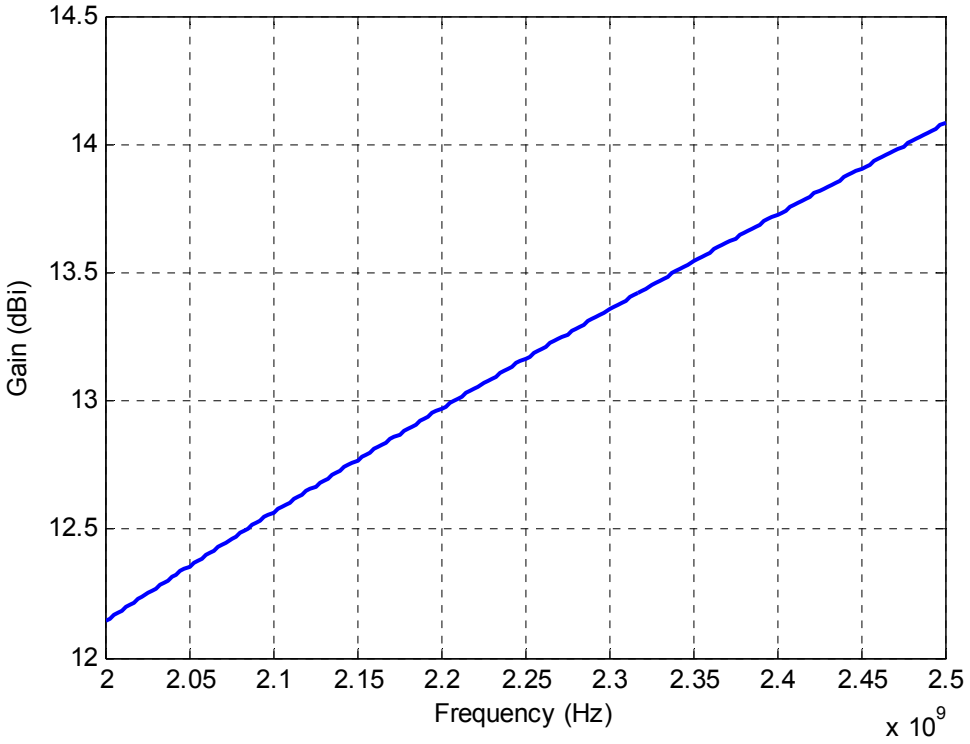

Figure A.4: Extrapolated main-lobe gain of the standard gain horn.

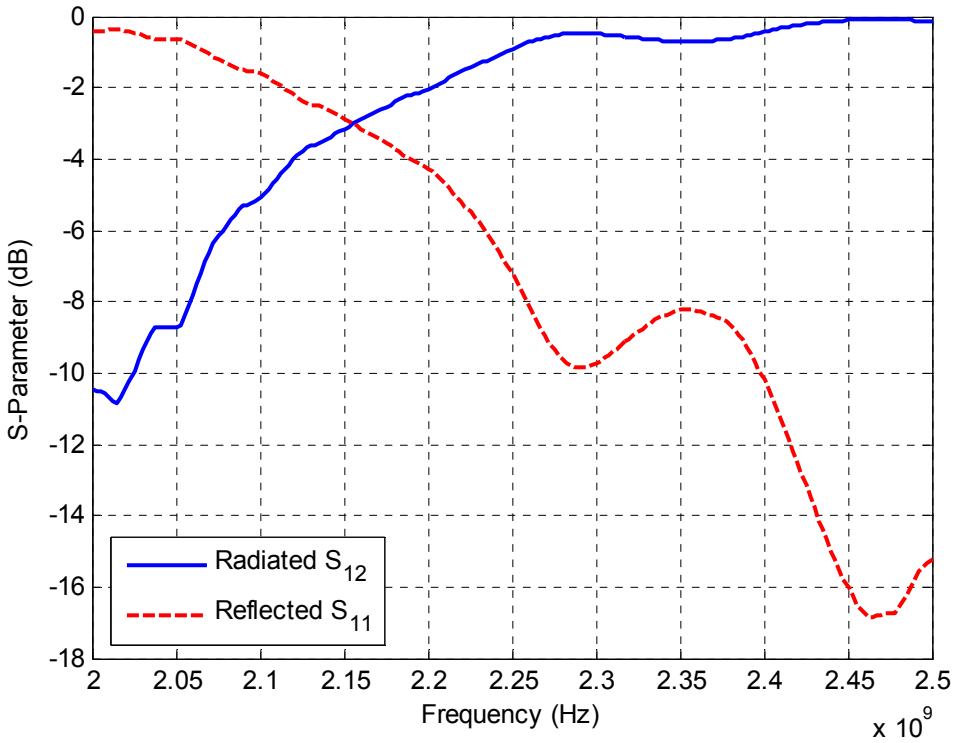

Figure A.5: Measured S-parameters of the standard gain horn.

APPENDIX B.
MATLAB-BASED PROGRAMS FOR CAPTURE AND CONTROL

B.1 GPIB Related Commands

These functions return abstracted container objects for a signal generator. This object contains the properties of the signal source as well as a handle to the GPIB interface for the source. The indicated power levels for these objects are preprogrammed for the experimental setup for the passes on 5/7/2006 and 5/9/2006, and they account for the cable loss between the signal generators and the JBoard receiver unit.

[LO] = GPIB_s33250_Clock()

Initailizes the Agilent 33250 signal source used for the 80 MHz clock for the digitizers.

[LO] = GPIB_s33250_Trigger()

Initializes the Agilent 33250 signal source used as the trigger pulse generator for the digitizers.

[LO] = GPIB_s83712()

Initializes the Hewlett Packard 83712 signal source used as the first local oscillator for the JBoard Receiver Assembly.

[LO] = GPIB_s8656()

Initializes the Hewlett Packard 8656 signal source used as the second local oscillator for the JBoard Receiver Assembly.

[none] = setSource(LO)

Programs the signal source encapsulated by the LO object. Although configuration of different sources requires different GPIB commands, the LO object contains abstract values that are the same regardless of the type of signal source used. For example, the code

```
LO1.freq = 930E6; LO1.power =6.0; LO1.rf = 1; setSource(LO1)
```

sets the frequency of LO1 to 930 MHz, the power to +6dBm, and enables the RF output. Because setSource handles identification and programming of the source, this code works regardless of the signal generator represented by LO1.

B.2 JBoard Related Commands

[decimalDataStream] = bits2dec(binaryDataStream)

Converts a binary data stream to a decimal data stream.

[none] = JBoard_BitWrite(decimalDataStream)

Writes the decimal data stream to the JBoard bus.

[binaryDataStream] = JBoard_CreateDataStream(dataValues, controlValues)

Returns a binary data stream for the four-wire serial interface of the JBoard programming bus. The inputs dataValues and controlValues contain the 8-bit sequences to load into the corresponding registers.

[Helper] = JBoard_MakeHelper()

Returns a helper object for JBoard programming containing language objects and their associated programming bits. For example, Helper.aLoadZOutput contains the address bits for programming the output attenuator.

[none] = JBoard_SetRCVR(JBoardReceiver)

Encapsulates the programming process for the JBoard bus. The JBoardReceiver object contains three variables describing the desired input attenuation, output attenuation, and bandwidth of the board. For example, the code

```
JB.attenInput=0; JB.switch='sw5'; JBoard_SetRCVR(JB)
```

configures the receivers on the JBoard bus with maximum input attenuation and 6 MHz bandwidth.

[binaryDataStream] = JBoard_WriteValue(mode, value)

Programs a single characteristic to the JBoard bus. Input modes specify which characteristic to program (input attenuation, output attenuation, or switch), and value indicates the value to program to this register. Returns the binary data stream used to program the bus.

[none] = jennieGUI()

Starts a graphical user interface for programming and testing a JENNIE board.

B.3 Automated Operation and Processing Based Commands

The functions for capturing and processing data utilize a Receiver object that contains calibration and control data for receiver channels. Unique Receiver objects are

created for each computer and contain data for the corresponding JENNIE receiver channels. The master computer also utilizes a Remote object, which contains the concatenated Receiver objects for all computers, the GPIB objects for controlling the local oscillators, and the JBoardReceiver object for programming the JBoard bus.

[Receiver] = X_CalibrateData(Receiver)

Calibrates the spectrum of the data stored in the Receiver object. Updates the Receiver object to include the power-spectral-density (magnitude) and voltage-spectral-density (complex) of the calibrated spectra. These spectra reflect the power and frequency of signals at the input port of the JENNIE receivers. Capture sequence #3.

[Receiver] = X_Capture(Receiver)

Captures raw data based on the characteristics of the Receiver object. Updates the Receiver object to include the raw captured data. Capture sequence #1.

[Receiver] = X_FFT(Receiver)

Processes raw data to generate baseband spectra of the inphase, quadrature, and combined channels. Updates the Receiver object to include the power-spectral-density (magnitude) and voltage-spectral-density (complex) of the baseband spectra. Capture sequence #2.

[Receiver] = X_PlotData(Receiver)

Resamples the calibrated power-spectral-density included in the Receiver object to create data suitable for plotting. The PSD can contain up to one million points;

this function downsamples to one thousand points. Updates the Receiver object to include the down sampled spectra. Capture sequence #4.

[none] = X_RemoteClose(Remote)

Closes all connections to objects contained in the Remote object. Turns off the signal sources, sets the JBoard receivers for maximum safety (high attenuation and low bandwidth), and terminates TCP/IP connections.

[Remote] = X_RemoteControl(ReceiverMaster)

Creates a Remote control object containing the GPIB, JBoard, and TCP/IP handles, and the receiver calibration data contained in the RecevierMaster object.

[Remote] = X_StartPebbles

Performs the start-up tasks for initializing the synchronous data acquisition system. Loads the calibration data for the boards, initializes the GPIB and JBoard connections, and starts the synchronization process. Returns the master remote control object used in the system.

[t12, t13] = X_SynchronizeBoardClocks(Remote)

Synchronizes the 10 MHz sample clocks on the digitizers. Returns the measured time delay between channels.

[Remote] = X_SynchronizeBoards(Remote)

A wrapper function that synchronizes the sample clocks and the trigger pulse. Updates the Remote object to include the results of the synchronization.

[triggerPhase, pError] = X_SynchronizeTriggerPhase(Remote)

Determines the best timing for the trigger pulse. Returns the optimized phase (in degrees for a 5 MHz trigger cycle) and the measured probability of a timing error for different values of the trigger phase.

B.4 Other Commands

Pnet

PNET is a public-domain Matlab-based TCP/IP interface [75]. It has the capacity to remotely control one or more Matlab processes on remote machines from a client machine. Dino and BamBam operated PNET in server mode, and Pebbles operated PNET in client mode.

XDA_Board_AuxBNC(device, function)

The Matlab-based commands provided by Exacq Technologies for operating the CH3160 cards were incomplete, especially regarding the Auxillary BNC connection on the card. This function allows access to the driver commands controlling the function of the Auxillary BNC connector, specifically for driving the internal 80 MHz clock based on an external source.

APPENDIX C.
PASS DATA FOR EO-1 OBSERVATIONS

The following tables contain calculated and observed data for the four passes of the NASA satellite EO-1. The data in the tables includes the rise and set time for the satellite, calculated and observed acquisition of signal (AOS) and loss of signal (LOS), and peak location. The observed AOS and LOS times are based on when the averaged signal power of the strongest channel rises above (and drops below) the noise floor. The observed AOS and LOS track locations are taken from the start and end of the prediceted track. The peak time is calculated from the point where the Doppler shift is zero. The peak location is observed based on the predicted track.

C.1 Pass #1: 4/29/2006

For the first pass, the array was positioned in close proximity to the north-east corner of the Van-Leer fifth floor offices. A partial track was obtained.

Table C.1:
Satellite Pass Data for EO-1 for 4/29/2006

Model	Predicted	Observed	Observed
Rise (0°)	22:53:15 (EDT)	---	---
AOS (5°)	22:54:36 (EDT)	22:54:56 (EDT)	6.5° El
AOS (Track)	---	144.5° Az	23.5° El
LOS (5°)	23:05:55 (EDT)	23:06:50 (EDT)	1.4° El
LOS (Track)	---	38.5° Az	49° El
Set (0°)	23:07:17 (EDT)	---	---
Peak	23:00:14 (EDT)	23:00:15 (EDT)	Snapshot 131.5
Peak Location	74.4° Az, 56.5° El	75.5° Az	56.0° El

.

C.2 Pass #2: 4/30/2006

The array was also positioned near the fifth-floor offices for the second pass. The tracking algorithm predicted a path for the satellite, but this path was incorrect. The satellite signal was blocked by buildings for much of this pass.

Table C.2:
Satellite Pass Data for EO-1 for 4/30/2006

Model	Predicted	Observed	Observed
Rise (0°)	23:32:29 (EDT)	---	---
AOS (5°)	23:33:50 (EDT)	23:39:05 (EDT)	49.8° El
AOS (Track)	---	---	---
LOS (5°)	23:45:08 (EDT)	23:45:15 (EDT)	4.5° El
LOS (Track)	---	---	---
Set (0°)	23:46:31 (EDT)	---	---
Peak	23:39:27 (EDT)	23:39:30 (EDT)	Snapshot 108.5
Peak Location	259.6° Az, 51.2° El	---	---

.

C.3 Pass #3: 5/7/2006

The array was moved to the far north-east corner of the Van Leer roof for the third pass. The tracking algorithm returned the true track of EO-1 for almost the full duration of this pass. It is noted that the difference between the predicted and observed peak is not as drastic as it appears from the table. Because the elevation coordinate is close to zenith, large differences in azimuth cause small angular differences.

Table C.3:
Satellite Pass Data for EO-1 for 5/07/2006

Model	Predicted	Observed	Observed
Rise (0°)	23:14:42 (EDT)	---	---
AOS (5°)	23:16:02 (EDT)	23:15:46 (EDT)	3.9° El
AOS (Track)	---	167.0° Az	6.5° El
LOS (5°)	23:27:33 (EDT)	23:27:57 (EDT)	3.3° El
LOS (Track)	---	347°Az	6.0° El
Set (0°)	23:28:54 (EDT)	---	---
Peak	23:21:46 (EDT)	23:21:46 (EDT)	Snapshot 109
Peak Location	259.4° Az, 82.3° El	253.0° Az	85.0° El

C.4 Pass #4: 5/9/2006

The array was positioned on the far north-east corner of Van Leer for the final pass. The algorithm obtained the true track of EO-1 for most of this pass.

Table C.4:
Satellite Pass Data for EO-1 for 5/09/2006

Model	Predicted	Observed	Observed
Rise (0°)	22:55:48 (EDT)	---	---
AOS (5°)	22:57:09 (EDT)	22:57:18 (EDT)	5.7° El
AOS (Track)	---	145.5° Az	24.0° El
LOS (5°)	23:08:31 (EDT)	23:09:33 (EDT)	1.1° El
LOS (Track)	---	353° Az	3.5° El
Set (0°)	23:09:53 (EDT)	---	---
Peak	23:02:49 (EDT)	23:02:51 (EDT)	Snapshot 99
Peak Location	74.6° Az, 60.8° El	73.0° Az	60.0° El

APPENDIX D.
SCAN-LOSS MANAGEMENT WITH A SPACE-FED LENS

D.1 Introduction

A ground station comprised entirely of fixed PLMA antennas will require thousands of antennas to achieve the data rates currently required by LEO satellites. This can lead to a very complex system and digitization rates greater than of one tera-bps (10^{12} bps) if each channel is digitized and stored. This problem is alleviated by using several medium-gain antennas, as opposed to many low-gain antennas. Horizon-to-horizon coverage and simultaneous downlink from spatially separated targets can be achieved while eliminating moving parts, if the medium-gain antennas are electronically steered. The application of scan loss or slant angle optimization used in the development of the PLMA can also be applied to a ground station comprised of electronically steered fixed antennas.

Several types of electronically steered medium gain antennas exist; they employ several different methods for steering the beam of the antenna without moving parts or conventional RF beamforming components. One simple type of electronically steered antenna is a parasitic antenna with variable loads on the parasitic elements, such as that described by Harrington [76-77] . Changing the load on a parasitic element alters its effect on the pattern of the antenna. Customarily, diodes open $(Z = \infty)$ or short $(Z = 0)$ the electrical midpoints of the parasitic elements depending on the steering direction.

A second type of electronically steered antenna is a reflect-array antenna, introduced by Berry in 1963 [78], which has been a subject of much research in recent

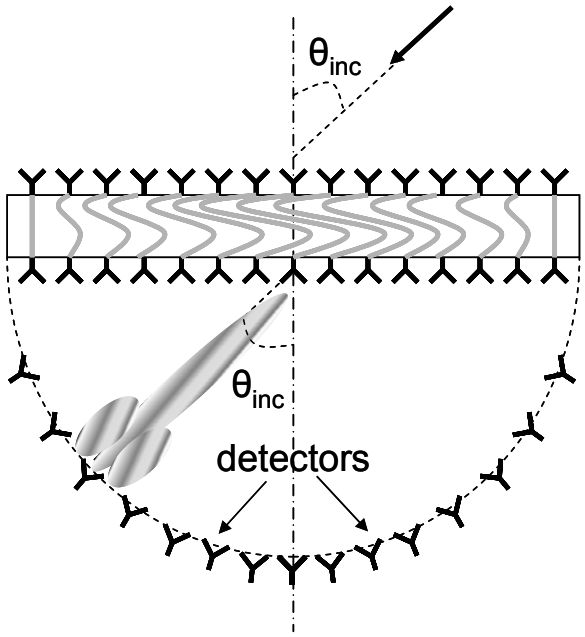

Figure D.1: Conceptual drawing of the Space-fed lens.

years, for example [79-81]. A reflectarray is similar to a dish reflector antenna but uses a planar reflector made of many small elemental (often microstrip patch) antennas, rather than a parabolic reflector. The impedance of each patch is controlled to vary the phase of the reflected wave, thus steering the reflected beam.

A third type of antenna is a Space-fed Lens (SFL), originally described by McGrath [82]. The basic operation of the SFL is illustrated in Figure D.1. An incoming plane wave encounters two layers of radiating elements separated by fixed phase shifts. The re-radiated wave on the feed-side is focused in a small area of the focal arc; small feed elements placed in the focal arc correspond to high-gain beams radiated in known directions.

The analyses in this section use a SFL as an elemental ground station antenna. The gain and scan loss model for this SFL is based on reported data for such an antenna

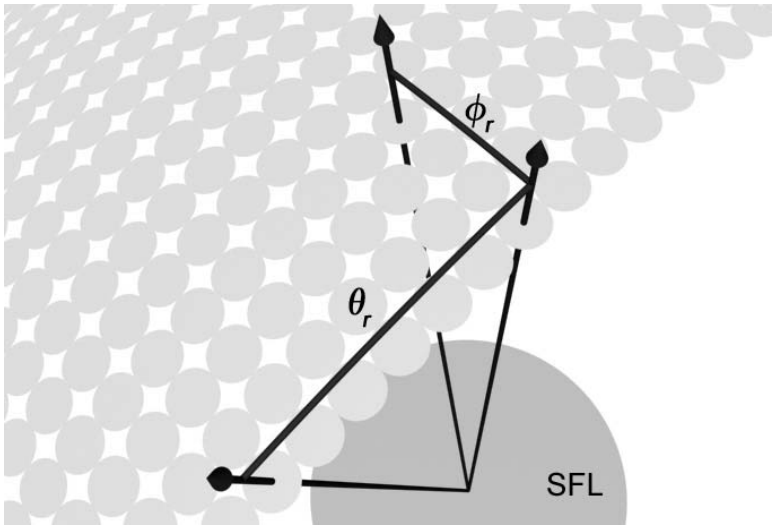

Figure D.2: Graphical representation of SFL beam positions.

[83-84]. This SFL has up to 32 beams placed at 2.5° intervals between ±38.75° from boresight. Alternatively, feeds can be placed at any location on a focal surface; an arrangement of spot beams is shown in Figure D.2, with beams arranged in 2.5° increments along (θ_r) and perpendicular to (ϕ_r) a principal plane of electronic scanning. Values of 35 dBi and 148K were assumed for the main-lobe gain and noise temperature of this antenna (including the LNA).

The X-band downlink on the satellite EO-1 was chosen as the reference link for this analysis. When this satellite is directly over a ground station, the required G/T for the ground station is 10.25 dB, accounting for required margins [7]. As with the development of the ground station antenna, pattern synthesis is applied to the array to make the received E_B/N_0 independent from the elevation angle of the satellite. In the context of an array of electronically steered antennas, pattern synthesis is akin to scan-loss synthesis. Each antenna exhibits scan loss, meaning the peak mainlobe gain of these

antennas diminishes as the antenna is steered away from boresight [85]. When several such electronically steered antennas are used in a ground station, the boresight directions of the antennas can be different. The boresight directions are optimized so the aggregate scan loss of the ground station varies according to the rules of the optimization, and the adaptive combination of the antenna outputs yields the highest possible DBR.

Three ground station models were analyzed with the GA, and the results are compared. The overall design goal is to maximize the amount of contact time with one or more satellites, therefore maximizing the DBR for a fixed data rate link. Models that produce similar values for the DBR can be compared; criteria for comparison include the number of antennas, the number of feeds when using a SFL, and the ability of the array to form multiple beams simultaneously to spatially separated satellites.

D.2 Model 1: Mechanical Azimuth, Electronic Elevation

The first model of pattern synthesis optimization with SFL antennas is the simplest, and provides a foundation for the following models. It is assumed that the antennas are mechanically steered in azimuth and electronically steered in elevation. Therefore, they will have scanning loss only as a function of elevation. Figure D.3a shows three SFLs, on azimuth turntables, sharing the same boresight direction and steered to the same target. In Figure D.3b each SFL has a different tilt, or boresight direction, but the mainlobes are steered to the same target location. Thus, for a given target location, each SFL exhibits a different value for scanning loss.

This scanning loss can be described by the function $G(\psi)$, where ψ is the elevation angle off-boresight, such that $G(0) = 1$. If the peak power gain of the SFL in

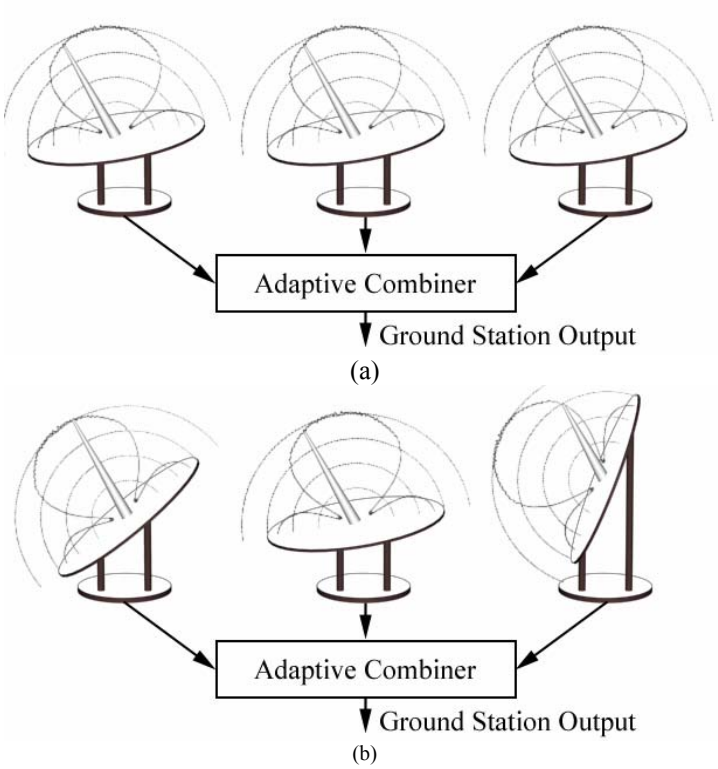

Figure D.3: Azimuth turntable configurations using the SFL. The SFLs in (a) are all tilted to the same angle. The SFLs in (b) are tilted at different angles. The scan loss behavior is overlaid with 10 dB intervals.

the boresight direction is given by a constant, A, then the power gain of the SFL when scanned to the angle ψ is $AG(\psi)$. The path loss between the ground station and the satellite is defined as $L_P(\theta)$, where θ is the elevation angle of the satellite and L_p is as defined in (5.4). If there are *N* SFLs and no other loss mechanisms, then the part of the link gain dependent only on $L_P(\theta)$ and the SFL mainlobe gains can be expressed by

$$G_L(\theta) = \left[A \cdot \sum_{n=1}^{N} G(\theta - \psi_n) \right] L_p(\theta), \qquad \text{(D.1)}$$

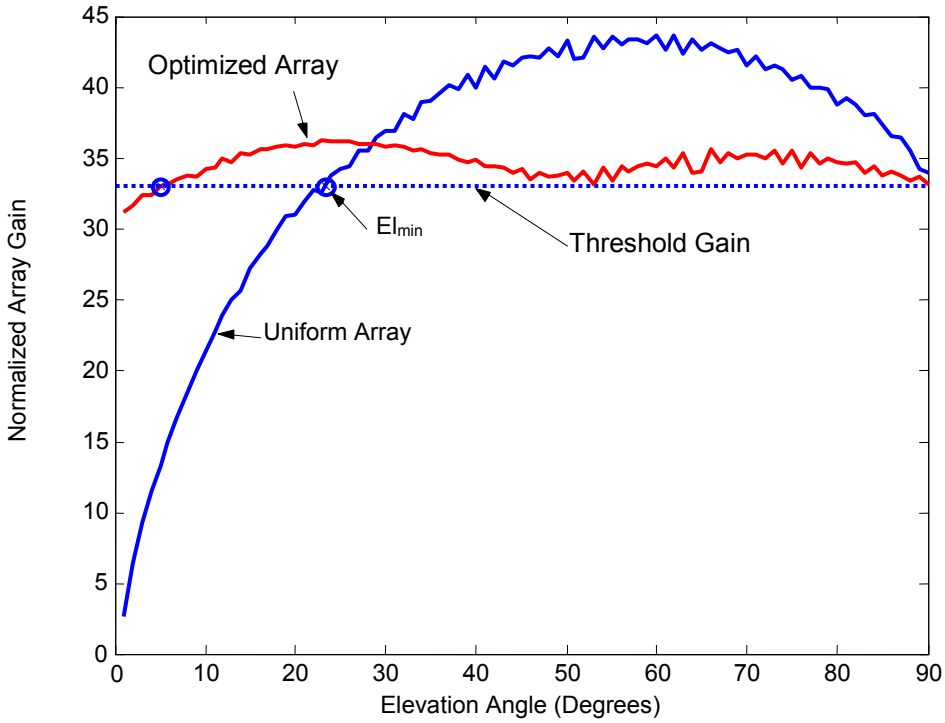

Figure D.4: The normalized link gain of the optimized SFL array as a function of elevation angle.

where ψ_n is the boresight elevation of the Nth Space-fed Lens. The GA optimizes the values of ψ to minimize the first elevation angle at which the received E_B/N_0 drops below the threshold value.

Figure D.4 contains plots of $G_L(\theta)/L_P(\theta)$ for two cases. The optimized design has an acquisition angle, $El_{\min}$, of $5°$ with eight antennas; despite the scan loss of the SFL, this is only one more antenna than would be required for an array of mechanically steered dish antennas that have the same peak mainlobe gain. The uniform array has an $El_{\min}$ of only $23°$ and an excess gain of more than 10 dB at some angles. The DBR of the optimized array is almost four times that of the uniform array.

D.3 Forming Multiple Beams

A method of further reducing the cost of downloading data is to have one ground station establish simultaneous downlinks with spatially separated satellites. If two satellites are close together in the same orbital plane, then it is possible to extend the previous model by adding beams to the SFL antennas or by allowing another electronically steered antenna to form multiple beams. Additional beams are achieved through the addition of feeds to the SFL; although feeds can be placed to form beams in any direction, within the limits of scan loss, economics drive the decision of how many feeds to include in the antenna.

One method of analysis is to assume a grid of possible beam locations at increments of 2.5° along (θ_r) and perpendicular to (ϕ_r) the principal plane of constant azimuth of the SFL, as shown in Figure D.2. For a particular configuration, it is possible to calculate how often each feed location is used, and thus how many feeds are necessary for each antenna. The number of required feeds is related to the amount of contact time the antenna has with the satellite, as compared to the amount of contact time when all feeds are used.

Figure D.5 contains beam usage density plots for antennas with tilt angles of 5° and 60°, for satellite separations of 1 and 2 minutes. These plots do not depend significantly on the latitude of the ground station. The origin of each plot represents the boresight pointing angle; the x and y axes represent the beam positions in ϕ_r and θ_r, respectively. Although this method can allow multiple beams to be formed to spatially separated transmitting sources, the angular separation of the sources will affect the scan loss exhibited by each SFL, and the gain to each source will be reduced as compared to

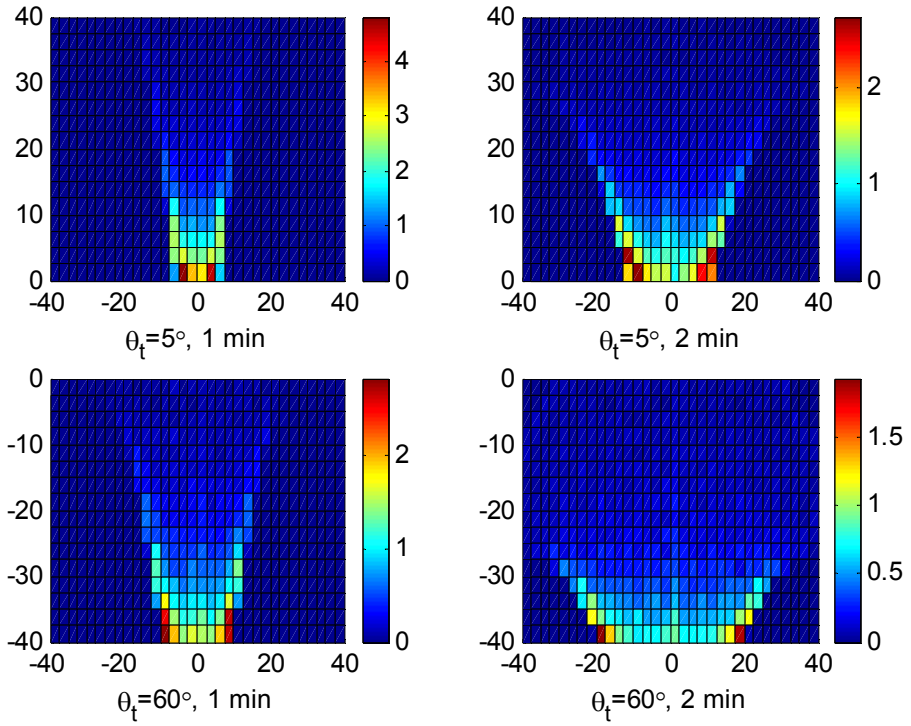

Figure D.5: Beam stimulation density for different SFL tilt angles and different satellite separation times. Color indicates percentage of total data downloaded using the indicated beam. The axes represent the beam coordinates (ϕ_r, θ_r).

the original optimization plot in Figure D.4. For example, if the maximum angular separation of the sources is $15°$, corresponding to a maximum additional scan loss of 3 dB, then twice as many antennas are required for this multibeaming method as for the single satellite case.

D.4 Model 2: Mechanically Tracking an Orbital Plane

If two satellites are separated by a larger increment of time, or if the array should track many satellites in a long orbital train, the previous method is insufficient for multibeaming from a single ground station. While pairs of satellites might be spaced less

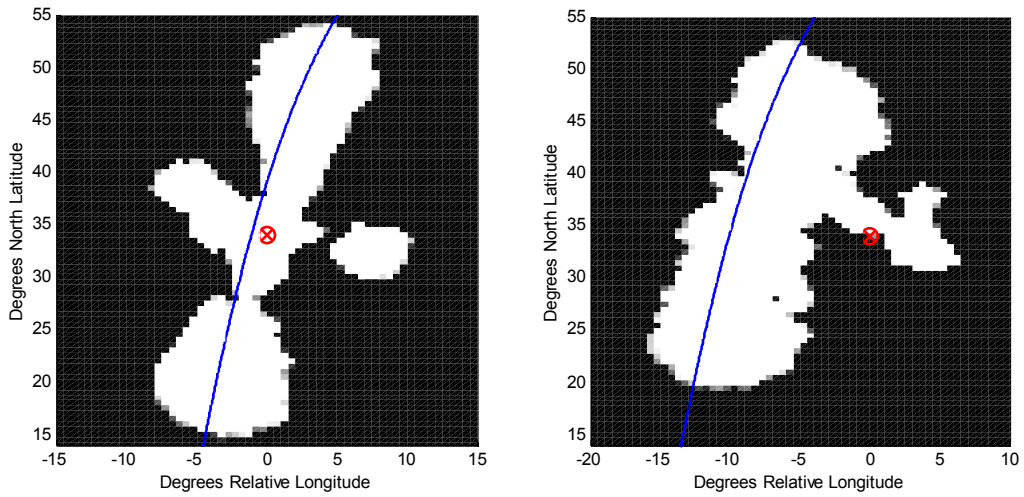

Figure D.6: Path tracking ground station footprint for a ground station located at 34°N. Peak elevations of the paths are 81° (left) and 32° (right). The blue line indicates subsatellite points corresponding to the paths. The ground station position is marked in red.

than a minute apart, a satellite train can consist of many satellites and span a comparatively long period of time.

One alternative arrangement is to add mechanical axes to the antennas, add more feeds, and construct the GA to orient the antennas to maximize contact time along an orbital plane, as projected into local coordinates. Two mechanical axes, azimuth and elevation, are required if the θ_r and ϕ_r electronic scan ranges are equal. A third axis, roll, is required if the values differ. If the satellites in the train are in the same orbit, then these mechanical axes must be constantly attended. On the other hand, if the satellites in the train share the same ground track, these mechanical axes can be set prior to a pass event and then locked until the pass is completed.

For paths with peak elevations above 45°, a required contact time of 90% of maximum implies 24 antennas in this arrangement; the contact time is slightly increased

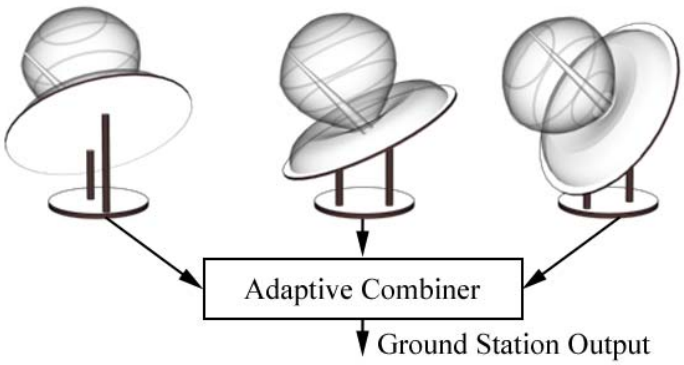

Figure D.7: Possible ground station configuration using the Space-fed Lens (SFL). The SFL apertures are fully populated, and each SFL is tilted to a different fixed azimuth and elevation coordinate. The scan loss behavior and pointing direction of a possible beam are shown as in Figure D.3.

when the fully populated SFLs are used, and decreased when the ϕ_r range is restricted to 15° off boresight. More antennas are required to achieve a contact time of 90% for paths with lower peak elevation angles. Figure D.6 contains footprint plots for a ground station at 34°N using 24 SFLs with ϕ_r limited to 15°. The figure is presented for tracking an orbital plane; tracking a constant ground track produces similar results. White regions in the figure define subsatellite points where a link can be established to the ground station; black regions define subsatellite points where the received signal strength is below the threshold for demodulation. Although the algorithm successfully places the visible region over the satellite path, the mechanically steered axes are undesirable for a high-reliability ground station.

D.5 Model 3: Full Sky Electronic Scanning

Further increasing the number of antennas will eliminate moving parts and allow simultaneous multibeaming outside of a single satellite train. In this case, the azimuth

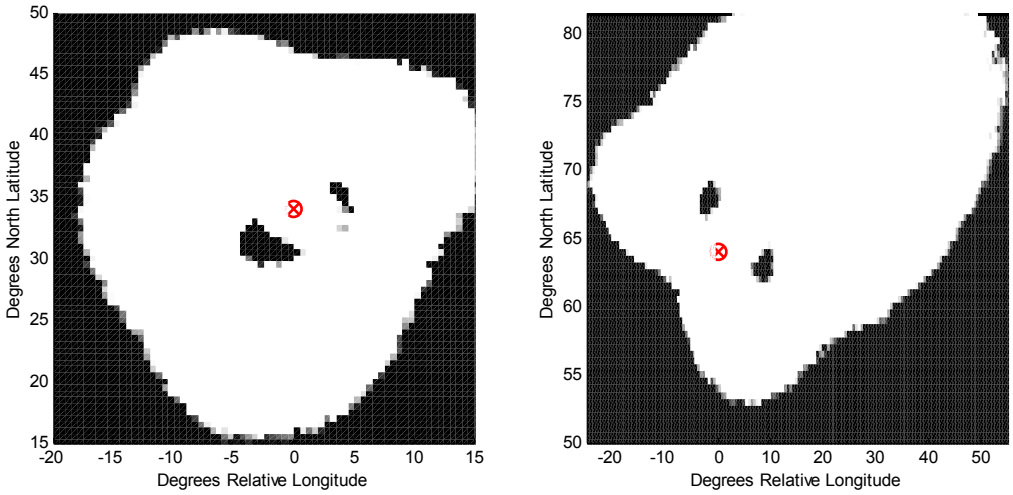

Figure D.8: Ground Station footprint for a ground station located at 34°N (left) and 64°N (right) using 32 fixed SFLs. Similar to Figure D.6.

and elevation tilt angles for an array of fixed antennas are optimized, and it is assumed that the antennas have a full 2D scanning range. Figure D.7 illustrates an array based on this case. The new optimization is designed to maximize the DBR of a constant data rate link for all points in the sky; the integral (2.7) is used to calculate the DBR based on the footprint of the ground station, the ground station coordinates, and satellite orbital characteristics.

Fixed arrays of 64 antennas achieve high per-satellite DBRs; this implies a high number of feeds, but the benefit is the complete elimination of moving parts and the ability to form many simultaneous beams to arbitrary coordinates. Footprint plots for ground stations located at 34°N and 64°N using 32 antennas are shown in Figure D.8. The higher latitude optimization shows the benefit of optimizing the array based on the probability integral (2.7). The footprint from the higher latitude displays a clear structure that is arranged to obtain a high contact time from the high-probability regions near the

poles. On the other hand, because there is only a small probability gradient at lower latitudes, the footprint for a ground station at 34°N displays no clear structure.

D.6 Station Comparisons

Table D.1 contains some comparative data on the different models of ground station optimization using the SFL antennas. Several optimized ground station configurations exhibit DBRs that are similar to that obtained using a single large-aperture dish antenna. While a SFL was used as the elemental antenna for this design, this analysis can be applied to arrays of any electronically steered antenna that exhibits scan loss.

Table D.1:
Ground Station Optimization and Performance

Model	Note	Total Antennas	Total Feeds (xE3)	DBR (GB)
Reference	11m dish at Poker Flats	1	-	585
Single	Standard, one satellite	8	0.14	585
Close Track*	1 Minute Separation	10	1.0	526
Close Track*	2 Minute Separation	20	3.9	526
Path Track	15 degree off plane	24	9.2	498
Path Track	Fully populated aperture	24	19.2	560
Full Sky	Fully populated aperture	32	16.4	266
Full Sky	Fully populated aperture	64	31.6	545
Full Sky	Half populated aperture	64	17.8	450

DBR analysis for ground stations located at 64°N, at the Poker Flats facility in Alaska. Feeds based on the definition of a fully populated aperture extending to 40° from broadside. Reducing this scan angle will increase the number of antennas but can reduce the total number of required feeds.
*Close track antennas and feeds estimated based on scan loss behavior of the SFL and the beam density plots from Figure D.5, and do not account for the increased scan loss of the SFL when steered off the principle plane.

APPENDIX E.
SUMMARY OF COORDINATE TRANSFORMATIONS

E.1 Local Beam Steering-Space

Local coordinates are often expressed in units of azimuth (clockwise angle from north) and elevation (angle above the horizon) rather than ϕ (counter-clockwise angle from the *x*-axis) and θ (angle from the positive *z*-axis). If the *x*-axis of the local coordinate system points north and the *z*-axis points toward zenith, then azimuth and elevation are determined by the relationships below.

$$Az = 360° - \phi \qquad \phi = 360° - Az$$
$$El = 90° - \theta \qquad \theta = 90° - El$$

E.2 Array Pattern-Space

The pattern-space used in this dissertation is a rectangular conversion of the beam steering-space. Pattern-space coordinates of a stimulus are described by their offset from the steering direction of the main beam, as in

$$\Delta u = u_{stimulus} - u_{steered}$$
$$\Delta v = v_{stimulus} - v_{steered}$$
$$\Delta w = w_{stimulus} - w_{steered}.$$

The values (u, v, w) are determined from the polar angles of the beam-steering space

$$u = \cos(\phi)\sin(\theta)$$
$$v = \sin(\phi)\sin(\theta)$$
$$w = \cos(\theta).$$

SEQUENTIAL INDEX OF REFERENCES

[1] K. Ford, "Space network: briefing to the NRC," *NASA Space Communications Division Technical Briefing*, Jan. 26-27, 2006.

[2] "Advanced NASA communications satellite gives broadband access new meaning," National Aeronautics and Space Administration, Goddard Space Flight Center, press release no. H02-40, Mar. 2002.

[3] *Earth Observation Magazine*, GITC America, Frederick, MD, vol. 13, April 2004.

[4] S. W. Ellingson and G. A. Hampson, "Argus: an L-Band array for detection of astronomical transients," presented at the 2003 IEEE Antennas and Propagation Soc. Int. Symposium, Columbus, OH, June 22-27, vol. 3, pp. 256-259.

[5] M. A. Ingram, R. Romanofsky, R. Q. Lee, F. Miranda, Z. Popovic, J. Langley, W. C. Barott, M. U. Ahmed, and D. Mandl, "Optimizing satellite communications with adaptive and phased array antennas," in *Proc. 2004 Earth Science Technology Conference*, Palo Alto, CA, June 22-24.

[6] B. Tomasic, J. Turtle, et al., "The geodesic dome phased array antenna for satellite control and communication – subarray design, development, and demonstration," presented at the 2003 IEEE Int. Symp. on Phased Array Sys. and Tech., Oct. 14-17, pp. 411-416.

[7] *Radio Frequency Interface Control Document (RFICD) Between the Earth Orbiter (EO)-1 Spacecraft and the Spaceflight Tracking and Data Network (STDN),* National Aeronautics and Space Administration, Goddard Space Flight Center, November 2000.

[8] T. Pratt and C. W. Bostian, *Satellite Communications*, New York: Wiley, 1986, pp. 11-30.

[9] F. R. Hoots and R. L. Roehrich, *Spacetrack Report No. 3: Models for Propagation of NORAD Element Sets*, Peterson Air Force Base, Aerospace Defense Center, Office of Astrodynamics, 1980. Ed. T. S. Kelso, 1988. Available online: http://celestrak.com/NORAD/documentation/spacetrk.pdf.

[10] Torsten Lorentzen. "Attitude control and determination system for DTUsat1," Technical University of Denmark. February 2002.

[11] W. L. Stutzman and G. A. Thiele*, Antenna Theory and Design*, 2nd ed., New York: Wiley, 1998.

[12] R. C. Hansen, *Phased Array Antennas*, New York: Wiley, 1998. pp. 465-466.

[13] S. L. Salas, E. Hille, and G. J. Etgen, *Calculus: One and Several Variables*, 8th Edition, New York: Wiley, 1999. pp. 187-188.

[14] D. S. Weile and E. Michielssen, "Genetic algorithm optimization applied to electromagnetics: A review," *IEEE Antennas Propagat. Mag.*, vol. 45, pp. 343-353, Mar. 1997.

[15] R. L. Haupt, "An introduction to genetic algorithms for electromagnetics," *IEEE Antennas Propag. Mag*., vol. 37 pp. 7-15, April 1995.

[16] M. G. Bray, D. H. Werner, D. W. Boeringer, and D. W. Machuga, "Optimization of thinned aperiodic linear phased arrays using genetic algorithms to reduce grating lobes during scanning", *IEEE Trans. Antennas Propagat.*, vol. 50, pp. 1732-1742, Dec. 2002.

[17] R. L. Haupt, "Thinned arrays using genetic algorithms," *IEEE Trans. Antennas Propagat.*, vol. 42, pp. 993-999, July 1994.

[18] D. S. Linden, "Using a real chromosome in a genetic algorithm for wire antenna optimization," *IEEE Antennas Propagat. 1997 Int'l Symposium Digest,* vol. 3, pp. 1680-1683, July 1997.

[19] D. W. Boeringer, D. H. Werner, and D. W. Machuga, "A simultaneous parameter adaptation scheme for genetic algorithms with application to phased array synthesis," *IEEE Trans. Antennas Propagat.*, vol. 53, pp. 356-371, Jan. 2005.

[20] E. E. Altshuler and D. S. Linden, "Wire-antenna designs using genetic algorithms," *IEEE Antennas Propagat. Magazine,* vol. 39, pp. 33-43, April 1997.

[21] E. E. Altshuler and D. S. Linden, "Design of a wire antenna using a genetic algorithm," *Journal of Electronic Defense*, vol.20, p.50-52, July 1997.

[22] E. E. Altshuler, "Electrically small self-resonant wire antennas optimized using a genetic algorithm," *IEEE Trans. Antennas Propagat.*, vol. 50, pp. 297-300, Mar. 2002.

[23] D. S. Linden, "The twisted Yagi antenna optimized with a genetic algorithm: a potential alternative to the helix," presented at the 2003 IEEE Antennas and Propagation Soc. Int. Symposium, Columbus, OH, June 22-27, vol. 1, pp. 153-156.

[24] R. M. Edwards, S. K. Khamas, and G. G. Cook, "Design of printed eccentric spiral antennas using genetic algorithm optimization," presented at the 1999 IEE National Conference on Antennas and Propagation, pp. 375-379, April 1999.

[25] F. J. Villegas, T. Cwik, Y. R. Sammi, and M. Manteghi, "A parallel electromagnetic genetic algorithm optimization (EGO) application for patch antenna design," *IEEE Trans. Antennas Propagat.,* vol. 52, pp. 2424-2435, Sep. 2004.

[26] P. L. Werner, M. J. Wilhelm, R. T. Salisbury, L. D. Swann, and D. H. Werner, "Novel design techniques for miniature circularly-polarized antennas using genetic algorithms," presented at the 2003 IEEE Antennas and Propagation Soc. Int. Symposium, Columbus, OH, June 22-27, vol. 1, pp. 145-148.

[27] *Manual of Regulations and Procedures for Federal Radio Frequency Management,* National Telecommunications and Information Administration, September 2004.

[28] D. M. Pozar, *Microwave Engineering*, 2nd ed., New York: Wiley, 1998.

[29] S. D. Rogers, C. M. Butler and A. Q. Martin, "Design and realization of GA-optimized wire monopole and matching network with 20:1 bandwidth" *IEEE Trans. Antennas Propagat.*, vol. 51, pp. 493-502, Mar. 2003.

[30] H. Araii, G. J. Durnan and S. Saito, "A dual element patch array antenna structure with microstrip triple stub matching," presented at the 2003 IEEE Antennas and Propagation Soc. Int. Symposium, Columbus, OH, June 22-27, vol. 4, pp. 528-531.

[31] C. A. Balanis*, Antenna Theory: Analysis and Design*, 2nd ed., New York: Wiley, 1982.

[32] Y. Lo, "A mathematical theory of antenna arrays with randomly spaced elements," *IEEE Trans. Antennas Propagat.*, vol. 12, pp. 257-268, May 1964.

[33] A. Ishimaru, "Theory of unequally-spaced arrays," *IEEE Trans. Antennas Propag*., vol. 10, pp 691-702, Nov. 1962.

[34] R. L. Haupt, "Unit circle represenatation of aperiodic arrays," *IEEE Trans. Antennas Propag*., vol. 43, pp. 1152-1155, Oct. 1995.

[35] A. Camps, A. Cardama, and D. Infantes, "Synthesis of large low-redundancy linear arrays," *IEEE Trans. Antennas Propag*., vol. 49, pp. 1881-1883, Dec. 2001.

[36] D. Werner, M. Gingrich, and P. Werner, "A self-similar fractal radiation pattern synthesis technique for reconfigurable multiband arrays," *IEEE Trans. Antennas Propag*., vol. 51, 1486-1498, July 2003.

[37] B. K. Chang, X. Ma, and H. B. Sequeira, "Minimax-maxmini algorithm: a new approach to optimization of thinned antenna arrays," *1994 AP-S Int'l Symp. Digest,* vol. 1, pp 20-24.

[38] A. Tennant, A. F. Fray, D. B. Adamson and M. W. Shelley, "Beam scanning characteristics of 64 element broadband volumetric array," Electronics Letters, vol. 33, pp. 2001-2002, 20 Nov. 1997.

[39] J. Ender and H. Wilden, "The crow's nest antenna – a spatial array in theory and experiment," *Proc. IEE 2nd Int'l Conf. Antennas Propagat,* Heslington, UK, pp. 25-27, 1991.

[40] R. Voles, "Spherical shell and volume arrays," *IEE Proc. Microwave Antennas Propagat,* vol. 142, pp. 498-500, 1995.

[41] A. D. Carr and P. J. Tittensor, "Volume array with optical feeds," presented at the 1998 Int. Topical Meeting on Microwave Photonics, Oct. 12-14, pp. 123-125.

[42] R. Schmidt, "Multiple emitter location and signal parameter estimation," *IEEE Trans. Antennas Propagat.*, vol. 34, pp. 276-280, Mar. 1986.

[43] R. Roy and T. Kailath, "ESPRIT-estimation of signal parameters via rotational invariance techniques," *IEEE Trans. Acoustics, Speech, and Signal Processing*, vol. 37, pp. 984-995, July 1989.

[44] R. E. Kalman, "A New approach to linear filtering and prediction problems," *Trans. ASME,* vol. 82, pp. 35-45, 1960.

[45] J. W. Cooley and J. W. Tukey, "An algorithm for the machine calculation of complex Fourier series," *Math. Comput.*, vol. 19, pp. 296-301, Apr. 1965.

[46] W. Nester, "The fast Fourier transform and the Butler matrix," *IEEE Trans. Antennas Propagat.*, vol. 16, pp. 360-360, May 1968.

[47] E. K. L. Hung and R. M. Turner, "A fast beamforming algorithm for large arrays," *IEEE Trans. Aerosp. Electron. Syst.*, vol. AES-19, pp. 598–607, July 1983.

[48] H. Subbaram and K. Abend, "Interference suppression via orthogonal projections: Performance analysis," *IEEE Trans. Antennas Propagat.*, vol. 41, pp. 1187–1193, Sept. 1993.

[49] S. W. Ellingson and G. A. Hampson, "A subspace-tracking approach to interference nulling for phased array-based radio telescopes," *IEEE Trans. Antennas Propagat.*, vol. 50, pp. 25–30, Jan. 2002.

[50] S. W. Ellingson and W. Cazemier, "Efficient multibeam synthesis with interference nulling for large arrays," *IEEE Trans. Antennas Propagat.*, vol. 51, pp. 503-511, Mar. 2003.

[51] W. Jiang, Y. Guo, T. Liu, W. Shen and W. Cao, "Comparison of random phasing methods for reducing beam pointing errors in phased array," *IEEE Trans. Antennas Propagat.*, vol. 51, pp. 782-787, Apr. 2003.

[52] M. S. Smith and Y. C. Guo, "A comparison of methods for randomizing phase quantization errors in phased arrays," *IEEE Trans. Antennas Propagat.,* vol. 31, pp. 821-828, Nov. 1983.

[53] G. Strang, *Linear Algebra and its Applications*, New York: Saunders College Publishing, 1988, pp. 183-193, 299.

[54] B. Razavi, *RF Microelectronics*, NJ: Prentice-Hall, 1998, pp. 214-217.

[55] G. R. Cooper and C. D. McGillem, *Probabilistic Methods of Signal and System Analysis*, 3rd. ed., New York: Oxford University Press, 1999. pp. and 257-262 (Chapter 11), pg. 73 (Chapter 14).

[56] J. D. Markel, "FFT pruning," *IEEE Trans. Audio Acoustics,* vol. 19, pp. 305-311, Dec. 1971.

[57] M. Lewis, "The development of algorithms for FFT processing of sparse data," IEE Colloquium on DSP Chips in Real-Time Instrumentation and Display Systems, Digest 1997/300, pp. 7/1-7/4. 24 Sept. 1997.

[58] H. Guo, G. A. Sitton and C. S. Burrus, "The quick Fourier transform: an FFT based on symmetries," *IEEE Trans. Signal Processing*, vol. 46, pp. 335-41, Feb. 1998.

[59] H. Guo, G. A. Sitton and C. S. Burrus, "The quick discrete Fourier transform," presented at the 1994 IEEE International Conf. on Acoustics, Speech, and Signal Processing, Adelaide, Australia, April 19-22.

[60] H. V. Sorensen and C. S. Burrus, "A new efficient algoirthm for computing a few DFT points," presented at the 1988 IEEE Intl Symposium on Circuits and Systems, June 7-9, vol. 2, pp 1915-18.

[61] H. V. Sorensen and C. S. Burrus, "Efficient computation of the DFT with only a subset of input or output points," *IEEE Trans. Signal Processing*, vol. 41, pp. 1184-200, March 1993.

[62] S. Bouguezel, M. O. Ahmad and M. Swamy, "Efficient pruning algorithms for the DFT computation for a subset of output samples," presented at the 2003 IEEE Intl. Symposium on Circuits and Systems, Bangkok, Thailand, May 25-28.

[63] H. Guo and C. S. Burrus, "Wavelet transform based fast approximate Fourier transform," presented at the 1997 IEEE Intl. Conf. on Acoustics, Speech, and Signal Processing, Munich, Germany, Apr. 21-24, vol. 6, pp. 1973-6.

[64] L. Rabiner, R. Schafer, and C. Rader, "The chirp z-transform algorithm," *IEEE Trans. Audio and Electroacoustics*, vol. 17, pp. 86-92, June 1969.

[65] G. Gilmour, B. Brown, and J. Lane, "CCD/SAW sonar beamforming," *OCEANS*, vol. 11, pp 104-108, Sep. 1979.

[66] M. Xu and X. Ping, "An improved fast Fourier transform in polar coordinate system," *Proceedings of IEEE: Intelligent Transportation Systems*, vol. 2, pp 1735-1739, 12-15 Oct. 2003.

[67] P. A. Chiavacci and J. W. Locke, "Planar phased array antenna relationships for FFT & Butler matrix generated beamlets with graphical display of results,"

presented at the 1996 IEEE Int. Symposium on Phased Array Systems and Technology, Oct. 15-18, pp. 196-202.

[68] W. C. Barott, *Design, Analysis, and Testing of the S-Band JENNIE Receiver System,* Georgia Institute of Technology, 2006.

[69] B. Z. Kobb, *Wireless Spectrum Finder,* New York, McGraw-Hill, 2001.

[70] *Exacq CH Series: High Speed Data Acquistion Boards for PCI Bus. User Manual.* Exacq Technologies, Indianapolis, IN, August 2004.

[71] A. V. Oppenheim, A. S. Willsky, and S. H. Nawab, *Signals and Systems*, 2nd ed., Upper Saddle River, New Jersey, Prentice-Hall, 1996, p. 328.

[72] *Listing of One Way Events: Monthly Report for EO-1 for 4/1/06 through 4/30/06,* National Aeronautics and Space Administration, Goddard Space Flight Center, Flight Dynamics Facility, May 2006.

[73] *HP 8560 E-Series Spectrum Analyzer Calibration Guide*, Hewlett-Packard, December 1997.

[74] M. A. Ingram, W. C. Barott, et al., "LEO downlink capacity analysis for a network of adaptive array ground stations," presented at the 2005 Earth Science Technology Conf., Adelphi, MD, June 27-30.

[75] P. Rydesäter, *PNET: IO-function for TCP and UDP Communication in Matlab*, Mid Sweden University, 2003.

[76] R. Harrington, "Reactively controlled directive arrays," *IEEE Trans. Antennas Propagat.*, vol. 26, pp. 390-395, May 1978.

[77] R. Schlub and D. V. Thiel, "Switched parasitic antenna on a finite ground plane with conductive sleeve," *IEEE Trans. Antennas Propagat.*, vol. 52, pp. 1343-1347, May 2004.

[78] D. G. Berry, R. G. Malech and W. A. Kennedy, "The reflectarray antenna," *IEEE Trans. Antennas Propagat.*, pp. 645-651, Nov. 1963.

[79] D. M. Pozar, S. D. Targonski, and H. D. Syrigos, "A shaped beam microstrip patch reflectarray," *IEEE Trans. Antennas Propagat.*, vol. 47, pp. 1167-1173, July 1999.

[80] R. R. Romanofsky and A. H. Qureshi, "A model for ferroelectric phase shifters," *IEEE Trans. Magnetics*, vol. 36, pp. 3491-3494, Sept. 2000.

[81] R. R. Romanofsky, J. T. Bernhard, F. W. Van Keuls, F. A. Meranda, G. Washington, and C. Canedy, "K-band phased array antennas based on $Ba_{0.60}Sr_{0.40}TiO_3$ thin-film phase shifters," *IEEE Trans. Microwave Theory and Techniques*, vol. 48, pp. 2504-2510, Dec. 2000.

[82] D. T. McGrath, "Planar three-dimensional constrained lenses," *IEEE Trans. Antennas Propagat.*, vol. AP-34, pp. 46-50, Jan. 1986.

[83] D. Popovic, Z. Popovic, "Multibeam antennas with polarization and angle diversity," *IEEE Trans. Antennas and Propagat., Special Issue on Wireless Communications*, pp. 651-657, May 2002.

[84] M. B. Perotoni, S. Rondineau, R. Lee, D. Consonni, and Z. Popovic, "X-band discrete lens array for a satellite communication ground station antenna," *Proc. IEEE MTT-S Int'l Conf. on Microwave and Optoelectronics*, pp. 197-200, July 2005.

[85] R. J. Mailloux, *Phased Array Antenna Handbook*, Boston: Artech House, 1993.

ALPHABETICAL INDEX OF REFERENCES

A

Altshuler, E. E., "Electrically small self-resonant wire antennas optimized using a genetic algorithm," *IEEE Trans. Antennas Propagat.*, vol. 50, pp. 297-300, Mar. 2002. [22]

Altshuler, E. E., and D. S. Linden, "Design of a wire antenna using a genetic algorithm," *Journal of Electronic Defense*, vol.20, p.50-52, July 1997. [21]

Altshuler, E. E., and D. S. Linden, "Wire-antenna designs using genetic algorithms," *IEEE Antennas Propagat. Magazine,* vol. 39, pp. 33-43, April 1997. [20]

Araii, H., G. J. Durnan and S. Saito, "A dual element patch array antenna structure with microstrip triple stub matching," presented at the 2003 IEEE Antennas and Propagation Soc. Int. Symposium, Columbus, OH, June 22-27, vol. 4, pp. 528-531. [30]

B

Balanis, C. A*., Antenna Theory: Analysis and Design*, 2nd ed., New York: Wiley, 1982. [31]

Barott, W. C., *Design, Analysis, and Testing of the S-Band JENNIE Receiver System,* Georgia Institute of Technology, 2006. [68]

Berry, D. G., R. G. Malech and W. A. Kennedy, "The reflectarray antenna," *IEEE Trans. Antennas Propagat.*, pp. 645-651, Nov. 1963. [78]

Boeringer, D. W., D. H. Werner, and D. W. Machuga, "A simultaneous parameter adaptation scheme for genetic algorithms with application to phased array synthesis," *IEEE Trans. Antennas Propagat.*, vol. 53, pp. 356-371, Jan. 2005. [19]

Bouguezel, S., M. O. Ahmad and M. Swamy, "Efficient pruning algorithms for the DFT computation for a subset of output samples," presented at the 2003 IEEE Intl. Symposium on Circuits and Systems, Bangkok, Thailand, May 25-28. [62]

Bray, M. G., D. H. Werner, D. W. Boeringer, and D. W. Machuga, "Optimization of thinned aperiodic linear phased arrays using genetic algorithms to reduce grating lobes during scanning", *IEEE Trans. Antennas Propagat.*, vol. 50, pp. 1732-1742, Dec. 2002. [16]

C

Camps, A., A. Cardama, and D. Infantes, "Synthesis of large low-redundancy linear arrays," *IEEE Trans. Antennas Propag*., vol. 49, pp. 1881-1883, Dec. 2001. [35]

Carr, A. D., and P. J. Tittensor, "Volume array with optical feeds," presented at the 1998 Int. Topical Meeting on Microwave Photonics, Oct. 12-14, pp. 123-125. [41]

Chang, B. K., X. Ma, and H. B. Sequeira, "Minimax-maxmini algorithm: a new approach to optimization of thinned antenna arrays," *1994 AP-S Int'l Symp. Digest,* vol. 1, pp 20-24. [37]

Chiavacci, P. A., and J. W. Locke, "Planar phased array antenna relationships for FFT & Butler matrix generated beamlets with graphical display of results," presented at the 1996 IEEE Int. Symposium on Phased Array Systems and Technology, Oct. 15-18, pp. 196-202. [67]

Cooley, J. W., and J. W. Tukey, "An algorithm for the machine calculation of complex Fourier series," *Math. Comput.*, vol. 19, pp. 296-301, Apr. 1965. [45]

Cooper, G. R., and C. D. McGillem, *Probabilistic Methods of Signal and System Analysis*, 3rd. ed., New York: Oxford University Press, 1999. pp. and 257-262 (Chapter 11), pg. 73 (Chapter 14). [55]

E

Earth Observation Magazine, GITC America, Frederick, MD, vol. 13, April 2004. [3]

Edwards, R. M., S. K. Khamas, and G. G. Cook, "Design of printed eccentric spiral antennas using genetic algorithm optimization," presented at the 1999 IEE National Conference on Antennas and Propagation, pp. 375-379, April 1999. [24]

Ellingson, S. W., and W. Cazemier, "Efficient multibeam synthesis with interference nulling for large arrays," *IEEE Trans. Antennas Propagat.*, vol. 51, pp. 503-511, Mar. 2003. [50]

Ellingson, S. W., and G. A. Hampson, "A subspace-tracking approach to interference nulling for phased array-based radio telescopes," *IEEE Trans. Antennas Propagat.*, vol. 50, pp. 25–30, Jan. 2002. [49]

Ellingson, S. W., and G. A. Hampson, "Argus: an L-Band array for detection of astronomical transients," presented at the 2003 IEEE Antennas and Propagation Soc. Int. Symposium, Columbus, OH, June 22-27, vol. 3, pp. 256-259. [4]

Ender, J., and H. Wilden, "The crow's nest antenna – a spatial array in theory and experiment," *Proc. IEE 2nd Int'l Conf. Antennas Propagat,* Heslington, UK, pp. 25-27, 1991. [39]

Exacq Technologies, *Exacq CH Series: High Speed Data Acquistion Boards for PCI Bus. User Manual.* Indianapolis, IN, August 2004. [70]

F

Ford, K., "Space network: briefing to the NRC," *NASA Space Communications Division Technical Briefing*, Jan. 26-27, 2006. [1]

G

Gilmour, G., B. Brown, and J. Lane, "CCD/SAW sonar beamforming," *OCEANS*, vol. 11, pp 104-108, Sep. 1979. [65]

Guo, H., and C. S. Burrus, "Wavelet transform based fast approximate Fourier transform," presented at the 1997 IEEE Intl. Conf. on Acoustics, Speech, and Signal Processing, Munich, Germany, Apr. 21-24, vol. 6, pp. 1973-6. [63]

Guo, H., G. A. Sitton and C. S. Burrus, "The quick discrete Fourier transform," presented at the 1994 IEEE International Conf. on Acoustics, Speech, and Signal Processing, Adelaide, Australia, April 19-22. [59]

Guo, H., G. A. Sitton and C. S. Burrus, "The quick Fourier transform: an FFT based on symmetries," *IEEE Trans. Signal Processing*, vol. 46, pp. 335-41, Feb. 1998. [58]

H

Hansen, R. C., *Phased Array Antennas*, New York: Wiley, 1998. pp. 465-466. [12]

Harrington, R., "Reactively controlled directive arrays," *IEEE Trans. Antennas Propagat.*, vol. 26, pp. 390-395, May 1978. [76]

Haupt, R. L., "An introduction to genetic algorithms for electromagnetics," *IEEE Antennas Propag. Mag.*, vol. 37 pp. 7-15, April 1995. [15]

Haupt, R. L., "Thinned arrays using genetic algorithms," *IEEE Trans. Antennas Propagat.*, vol. 42, pp. 993-999, July 1994. [17]

Haupt, R. L., "Unit circle represenatation of aperiodic arrays," *IEEE Trans. Antennas Propag.*, vol. 43, pp. 1152-1155, Oct. 1995. [34]

Hewlett-Packard, *HP 8560 E-Series Spectrum Analyzer Calibration Guide*, December 1997. [73]

Hoots, F. R., and R. L. Roehrich, *Spacetrack Report No. 3: Models for Propagation of NORAD Element Sets*, Peterson Air Force Base, Aerospace Defense Center, Office

of Astrodynamics, 1980. Ed. T. S. Kelso, 1988. Available online: http://celestrak.com/NORAD/documentation/spacetrk.pdf. [9]

Hung, E. K. L., and R. M. Turner, "A fast beamforming algorithm for large arrays," *IEEE Trans. Aerosp. Electron. Syst.*, vol. AES-19, pp. 598–607, July 1983. [47]

I

Ingram, M. A., W. C. Barott, et al., "LEO downlink capacity analysis for a network of adaptive array ground stations," presented at the 2005 Earth Science Technology Conf., Adelphi, MD, June 27-30. [74]

Ingram, M. A., R. Romanofsky, R. Q. Lee, F. Miranda, Z. Popovic, J. Langley, W. C. Barott, M. U. Ahmed, and D. Mandl, "Optimizing satellite communications with adaptive and phased array antennas," in *Proc. 2004 Earth Science Technology Conference*, Palo Alto, CA, June 22-24. [5]

Ishimaru, A., "Theory of unequally-spaced arrays," *IEEE Trans. Antennas Propag*., vol. 10, pp 691-702, Nov. 1962. [33]

J

Jiang, W., Y. Guo, T. Liu, W. Shen and W. Cao, "Comparison of random phasing methods for reducing beam pointing errors in phased array," *IEEE Trans. Antennas Propagat.*, vol. 51, pp. 782-787, Apr. 2003. [51]

K

Kalman, R. E., "A New approach to linear filtering and prediction problems," *Trans. ASME,* vol. 82, pp. 35-45, 1960. [44]

Kobb, B. Z., *Wireless Spectrum Finder,* New York, McGraw-Hill, 2001. [69]

L

Lewis, M., "The development of algorithms for FFT processing of sparse data," IEE Colloquium on DSP Chips in Real-Time Instrumentation and Display Systems, Digest 1997/300, pp. 7/1-7/4. 24 Sept. 1997. [57]

Linden, D. S., "The twisted Yagi antenna optimized with a genetic algorithm: a potential alternative to the helix," presented at the 2003 IEEE Antennas and Propagation Soc. Int. Symposium, Columbus, OH, June 22-27, vol. 1, pp. 153-156. [23]

Linden, D. S., "Using a real chromosome in a genetic algorithm for wire antenna optimization," *IEEE Antennas Propagat. 1997 Int'l Symposium Digest,* vol. 3, pp. 1680-1683, July 1997. [18]

Lo, Y., "A mathematical theory of antenna arrays with randomly spaced elements," *IEEE Trans. Antennas Propagat.*, vol. 12, pp. 257-268, May 1964. [32]

Lorentzen, Torsten, "Attitude control and determination system for DTUsat1," Technical University of Denmark. February 2002. [10]

M

Mailloux, R. J., *Phased Array Antenna Handbook*, Boston: Artech House, 1993. [85]

Markel, J. D., "FFT pruning," *IEEE Trans. Audio Acoustics,* vol. 19, pp. 305-311, Dec. 1971. [56]

McGrath, D. T., "Planar three-dimensional constrained lenses," *IEEE Trans. Antennas Propagat.*, vol. AP-34, pp. 46-50, Jan. 1986. [82]

N

National Aeronautics and Space Administration, "Advanced NASA communications satellite gives broadband access new meaning," Goddard Space Flight Center, press release no. H02-40, Mar. 2002. [2]

National Aeronautics and Space Adminsitration, *Listing of One Way Events: Monthly Report for EO-1 for 4/1/06 through 4/30/06,* Goddard Space Flight Center, Flight Dynamics Facility, May 2006. [72]

National Aeronautics and Space Administration, *Radio Frequency Interface Control Document (RFICD) Between the Earth Orbiter (EO)-1 Spacecraft and the Spaceflight Tracking and Data Network (STDN),* Goddard Space Flight Center, November 2000. [7]

National Telecommunications and Information Administration, *Manual of Regulations and Procedures for Federal Radio Frequency Management*, September 2004. [27]

Nester, W., "The fast Fourier transform and the Butler matrix," *IEEE Trans. Antennas Propagat.*, vol. 16, pp. 360-360, May 1968. [46]

O

Oppenheim, A. V., A. S. Willsky, and S. H. Nawab, *Signals and Systems*, 2nd ed., Upper Saddle River, New Jersey, Prentice-Hall, 1996, p. 328. [71]

P

Pratt, T., and C. W. Bostian, *Satellite Communications*, New York: Wiley, 1986, pp. 11-30. [8]

Perotoni, M. B., S. Rondineau, R. Lee, D. Consonni, and Z. Popovic, "X-band discrete lens array for a satellite communication ground station antenna," *Proc. IEEE MTT-S Int'l Conf. on Microwave and Optoelectronics*, pp. 197-200, July 2005. [84]

Popovic, D., Z. Popovic, "Multibeam antennas with polarization and angle diversity," *IEEE Trans. Antennas and Propagat., Special Issue on Wireless Communications*, pp. 651-657, May 2002. [83]

Pozar, D. M., *Microwave Engineering*, 2nd ed., New York: Wiley, 1998. [28]

Pozar, D. M., S. D. Targonski, and H. D. Syrigos, "A shaped beam microstrip patch reflectarray," *IEEE Trans. Antennas Propagat.*, vol. 47, pp. 1167-1173, July 1999. [79]

R

Rabiner, L., R. Schafer, and C. Rader, "The chirp z-transform algorithm," *IEEE Trans. Audio and Electroacoustics*, vol. 17, pp. 86-92, June 1969. [64]

Razavi, B., *RF Microelectronics*, NJ: Prentice-Hall, 1998, pp. 214-217. [54]

Rogers, S. D., C. M. Butler and A. Q. Martin, "Design and realization of GA-optimized wire monopole and matching network with 20:1 bandwidth" *IEEE Trans. Antennas Propagat.*, vol. 51, pp. 493-502, Mar. 2003. [29]

Romanofsky, R. R., J. T. Bernhard, F. W. Van Keuls, F. A. Meranda, G. Washington, and C. Canedy, "K-band phased array antennas based on $Ba_{0.60}Sr_{0.40}TiO_3$ thin-film phase shifters," *IEEE Trans. Microwave Theory and Techniques*, vol. 48, pp. 2504-2510, Dec. 2000. [81]

Romanofsky, R. R., and A. H. Qureshi, "A model for ferroelectric phase shifters," *IEEE Trans. Magnetics*, vol. 36, pp. 3491-3494, Sept. 2000. [80]

Roy, R., and T. Kailath, "ESPRIT-estimation of signal parameters via rotational invariance techniques," *IEEE Trans. Acoustics, Speech, and Signal Processing*, vol. 37, pp. 984-995, July 1989. [43]

Rydesäter, P., *PNET: IO-function for TCP and UDP Communication in Matlab*, Mid Sweden University, 2003. [75]

S

Salas, S. L., E. Hille, and G. J. Etgen, *Calculus: One and Several Variables*, 8th Edition, New York: Wiley, 1999. pp. 187-188. [13]

Schlub, R., and D. V. Thiel, "Switched parasitic antenna on a finite ground plane with conductive sleeve," *IEEE Trans. Antennas Propagat.*, vol. 52, pp. 1343-1347, May 2004. [77]

Schmidt, R., "Multiple emitter location and signal parameter estimation," *IEEE Trans. Antennas Propagat.*, vol. 34, pp. 276-280, Mar. 1986. [42]

Smith, M. S., and Y. C. Guo, "A comparison of methods for randomizing phase quantization errors in phased arrays," *IEEE Trans. Antennas Propagat.,* vol. 31, pp. 821-828, Nov. 1983. [52]

Sorensen, H. V., and C. S. Burrus, "A new efficient algoirthm for computing a few DFT points," presented at the 1988 IEEE Intl Symposium on Circuits and Systems, June 7-9, vol. 2, pp 1915-18. [60]

Sorensen, H. V., and C. S. Burrus, "Efficient computation of the DFT with only a subset of input or output points," *IEEE Trans. Signal Processing*, vol. 41, pp. 1184-200, March 1993. [61]

Strang, G., *Linear Algebra and its Applications*, New York: Saunders College Publishing, 1988, pp. 183-193, 299. [53]

Subbaram, H., and K. Abend, "Interference suppression via orthogonal projections: Performance analysis," *IEEE Trans. Antennas Propagat.*, vol. 41, pp. 1187–1193, Sept. 1993. [48]

Stutzman, W. L., and G. A. Thiele*, Antenna Theory and Design*, 2nd ed., New York: Wiley, 1998. [11]

T

Tennant, A., A. F. Fray, D. B. Adamson and M. W. Shelley, "Beam scanning characteristics of 64 element broadband volumetric array," Electronics Letters, vol. 33, pp. 2001-2002, 20 Nov. 1997. [38]

Tomasic, B., J. Turtle, et al., "The geodesic dome phased array antenna for satellite control and communication – subarray design, development, and demonstration," presented at the 2003 IEEE Int. Symp. on Phased Array Sys. and Tech., Oct. 14-17, pp. 411-416. [6]

V

Villegas, F. J., T. Cwik, Y. R. Sammi, and M. Manteghi, "A parallel electromagnetic genetic algorithm optimization (EGO) application for patch antenna design," *IEEE Trans. Antennas Propagat.,* vol. 52, pp. 2424-2435, Sep. 2004. [25]

Voles, R., "Spherical shell and volume arrays," *IEE Proc. Microwave Antennas Propagat,* vol. 142, pp. 498-500, 1995. [40]

W

Weile, D. S., and E. Michielssen, "Genetic algorithm optimization applied to electromagnetics: A review," *IEEE Antennas Propagat. Mag.*, vol. 45, pp. 343-353, Mar. 1997. [14]

Werner, D., M. Gingrich, and P. Werner, "A self-similar fractal radiation pattern synthesis technique for reconfigurable multiband arrays," *IEEE Trans. Antennas Propag*., vol. 51, 1486-1498, July 2003. [36]

Werner, P. L., M. J. Wilhelm, R. T. Salisbury, L. D. Swann, and D. H. Werner, "Novel design techniques for miniature circularly-polarized antennas using genetic algorithms," presented at the 2003 IEEE Antennas and Propagation Soc. Int. Symposium, Columbus, OH, June 22-27, vol. 1, pp. 145-148. [26]

X

Xu, M., and X. Ping, "An improved fast Fourier transform in polar coordinate system," *Proceedings of IEEE: Intelligent Transportation Systems*, vol. 2, pp 1735-1739, 12-15 Oct. 2003. [66]

VITA

William Chauncey Barott was born in Logan, Utah in 1980. After spending time in California and eastern Washington, he moved with his family to Atlanta in 1991. After graduating from Lassiter High School in Marietta in 1997, he entered the Georgia Institute of Technology, where he pursued Electrical Engineering. He earned his BS with Highest Honors in 2001 and opted to stay for graduate school, earning his MS in 2003 and PhD in 2006.

In the midst of his doctoral end-game, he was married in January of 2006 to Jeanette Gartman, whose support was invaluable throughout the preceding years of graduate school. In his spare time, he busies himself with diverse activities such as building furniture, acting in and writing plays, and playing his violin.

Following the completion of his dissertation, he and Jeanette will move to Daytona Beach, Florida, where he has accepted a faculty position at Embry-Riddle Aeronautical University.